Anisotropic moment tensor inversion and geomechanical modeling of fracturing-induced seismicity

DISSERTATION

zur Erlangung des Grades eines

DOKTORS DER NATURWISSENSCHAFTEN

am Fachbereich Geowissenschaften
der Freien Universität Berlin

vorgelegt von

Nepomuk Boitz

Berlin
Mai 2021

Erstgutachter: Prof. Serge A. Shapiro
Zweitgutachter: Prof. Frederik Tilmann
Datum der Disputation: 15.07.2021

Hiermit erkläre ich an Eides statt, dass ich die vorliegende Dissertation selbstständig und nur unter Verwendung der angegebenen Quellen und Hilfsmittel angefertigt habe.

Berlin, den 21.05.2021

Summary

It has long been known that the injection of fluids into the earth's subsurface can cause seismic activity. Usually, magnitudes of this anthropogenic seismicity are too small to be felt at the surface, but several cases of large-magnitude earthquakes related to fluid operations are known. A deeper understanding of the physical mechanisms and controlling parameters of this anthropogenic seismicity is therefore of interest for science as well as for society.

This thesis aims to improve the characterization of source mechanisms of fracturing-induced seismicity. For this, I develop a framework that takes the effect of seismic anisotropy on the source process into account. Microseismic events induced by hydraulic fracturing are typically located in shales, that can exhibit high degrees of anisotropy. This can affect the radiation pattern of events and thus can lead to a misinterpretation of source deformation if not accounted for correctly. In this thesis, I describe a methodology that considers adequately the anisotropy both in the source region and along the propagation path. I examine the influence of various anisotropy parameters on different seismic sources and propose a visualization that directly represents the strain caused by a microseismic source.

The source process of most earthquakes can be approximated by double-couple faulting, that is the rupture occurs as shear on a fault plane and does not contain opening or closing components. For such sources, I propose a decomposition that can be used to analyze different source orientations. Additionally, I suggest a new visualization tool to evaluate the diversity of many mechanisms at the same time. This could be applied to potentially distinguish between natural and induced seismicity. The new decomposition and the source type plot are particularly beneficial for the analysis of fracturing-induced seismicity as it explicitly incorporates the half-moon faulting type, which is typical in this environment.

Subsequently, I use these two theoretical tools to invert and analyze source mechanisms of hydraulic fracturing-induced seismicity. I show that anisotropy has a notable effect on the determined mechanisms and that accounting for this effect correctly, creates a more coherent distribution of mechanisms. The decomposition shows two main types of faulting, (1) strike-slip faulting and (2) dip-slip faulting on nearly vertical fault planes. Strike-slip faulting is characteristic for the tectonic seismicity of the region, the second mechanism type, frequently called half-moon faulting, is a typical source mechanism for hydraulic fracturing.

Half-moon events are observed hardly anywhere in natural seismicity but are typically observed during hydraulic fracturing stimulations. Therefore, this event type seems to be directly related to the fracturing process. I provide an explanation for the occurrence of these events, by using geomechanical modeling. This involves the quantification of fracturing-induced changes of the local stress field which triggers these earthquakes. I elaborate that half-moon events require special stress conditions in the subsurface, for instance, local rotations of the principal stresses. 2D geomechanical modeling shows that these conditions are created in the vicinity of the tips of hydraulic fractures and at layer boundaries that are crossed by the fracture. This model can be used to study hydraulic fracturing under normal-faulting conditions. I complement the modeling with a 3D model that is also capable of modeling hydraulic fracturing under general strike-slip conditions. I compare this model to the studied dataset and show that several field characteristics can be reproduced and explained. The study demonstrates the importance of the integration of data analysis and numerical modeling to accurately capture the physical processes in the source.

Altogether, this thesis provides two new theoretical tools that can be applied to any microseismic dataset in order to achieve more accurate and more consistent results. It further provides new insights into the long-standing discussion on the physical conditions responsible for the occurrence of half-moon events. Consequently, this thesis yields an important contribution to the general physical understanding of fluid-induced seismicity.

Zusammenfassung

Es ist seit langem bekannt, dass die Injektion von Fluiden in den Untergrund zu seismischer Aktivität führen kann. Die Magnituden dieser anthropogenen Seismizität sind typischerweise zu gering, um an der Erdoberfläche gespürt zu werden. Es sind jedoch auch einige Fälle größerer Beben bekannt, die auf Fluidinjektionen zurückzuführen sind. Ein besseres Verständnis der physikalischen Prozesse und der kontrollierenden Parameter ist deswegen notwendig und von Interesse, sowohl für die Wissenschaft als auch für die Gesellschaft.

Das Ziel dieser Arbeit ist es, die Herdmechanismen von mikroseismischer Aktivität besser zu verstehen. Dafür entwickle ich einen Rahmen, der den Einfluss von Anisotropie auf den Quellprozess eines Bebens miteinbezieht. Mikroseismische Ereignisse, die durch *Hydraulic Fracturing* hervorgerufen werden, liegen häufig in Tonschiefern, die einen hohen Grad von seismischer Anisotropie aufweisen können. Diese Anisotropie kann die Abstrahlmuster seismischer Quellen beeinflussen und kann, wenn sie nicht korrekt in die Modellierung einbezogen wird, zu einer Missinterpretation des Bruchprozesses führen. In dieser Arbeit zeige ich eine Methodik, die sowohl den Einfluss von Anisotropie auf die Quellregion als auch auf die Wellenausbreitung betrachtet. Dazu zeige ich den Einfluss verschiedener Anisotropieparameter auf die Abstrahlmuster verschiedener seismischer Quellen und schlage daraufhin eine neue Visualisierung vor, mit der die durch ein Erdbeben hervorgerufene Verformung, unabhängig von der Anisotropie, dargestellt werden kann.

Die Herdmechanismen der meisten Erdbeben können durch einen sogenannten *double-couple* Bruchprozess beschrieben werden, der als Scherbruch auf der Bruchfläche stattfindet und keine signifikanten Öffnungs- oder Schließungsanteile hat. Für diese Erdbeben zeige ich eine neue Art der Momententensor-Zerlegung, mit der verschiedene Bruchorientierungen beschrieben werden können. Außerdem schlage ich eine Methode vor, um diese Orientierungen zu visualisieren, sodass die Mechanismen vieler Beben gleichzeitig verglichen werden können. Diese Visualisierung bietet die Möglichkeit verschiedene Typen von Erdbeben voneinander abzugrenzen und möglicherweise zwischen natürlicher und induzierter Seismizität zu unterscheiden. Diese neue Momententensor-Zerlegung und Visualisierung sind besonders geeignet, um Beben zu untersuchen, die durch *Hydraulic Fracturing* induziert wurden, da sie mit *Half-Moon Faulting* einen Bruchprozess beinhaltet, der dabei typischerweise beobachtet wird.

Anschließend nutze ich diese beiden Techniken, um Herdmechanismen von Erdbeben, die durch *Hydraulic Fracturing* hervorgerufen wurden, zu invertieren und zu analysieren. Ich zeige, dass die Anisotropie einen bemerkbaren Einfluss auf diese Mechanismen hat und das ihre korrekte Einbeziehung in die Modellierung zu einer gleichförmigeren Verteilung der Bruchmuster führt. Bei der Analyse des Datensatzes können zwei verschiedene Arten von Seismizität unterschieden werden: Blattverschiebungen und Mechanismen, die eine vertikale Bewegungsrichtung auf einer vertikal orientierten Bruchfläche zeigen. Blattverschiebungen sind typisch für tektonische Seismizität in dieser Region, der zweite Typ, häufig *Half-Moon Faulting* genannt, ist ein typischer Bruchtyp für *Hydraulic Fracturing*.

Half-moon Beben sind zwar typische Mechanismen für *Hydraulic Fracturing*, werden jedoch so gut wie nie bei natürlicher Seismizität beobachtet und scheinen deshalb direkt mit dem Fracturing-Prozess zusammenzuhängen. Mithilfe von geomechanischer Modellierung, zeige ich einen Erklärungsansatz für das Auftreten dieser Beben. Dazu quantifiziere ich die Änderungen der Stressverhältnisse im Untergrund, die durch die hydraulische Stimulation hervorgerufen werden und die diese Beben auslösen. Ich zeige, dass diese Beben spezielle Stressbedingungen im Untergrund, wie zum Beispiel lokale Rotationen der Hauptstressrichtungen, benötigen. Mit numerischer 2D Modellierung zeige ich, dass diese Bedingungen an den vertikalen Enden einer *Hydraulic Fracture* auftreten, sowie an Schichtgrenzen, die von der *Fracture* durchbrochen werden. Das 2D Modell kann nur verwendet werden, um *Hydraulic Fracturing* unter Abschiebungsbedingungen zu beschreiben, weswegen ich im Anschluss die Modellierung um ein 3D Modell erweitere. Dieses Modell kann außerdem verwendet werden, um *Hydraulic Fracturing* unter Blattverschiebungsbedingungen zu untersuchen. Anschließend vergleiche ich die Ergebnisse der numerischen Modellierungen mit dem untersuchten Datensatz und zeige, dass das Modell in der Lage ist, Resultate der Datenbearbeitung zu reproduzieren und zu erklären. Dieser Vergleich zeigt, wie wichtig gemeinsame Datenanalyse und numerische Modellierung sind, um die physikalischen Prozesse des Bruchprozesses zu verstehen.

Insgesamt stellt diese Arbeit zwei neue Werkzeuge zur Bearbeitung und Analyse von Mikroseismizität zur Verfügung, die es ermöglichen, genauere Herdmechanismen zu erhalten und diese übersichtlicher darzustellen. Außerdem bietet sie neue Einblicke in die physikalischen Bedingungen, die für das Auftreten von *Half-Moon* Beben verantwortlich sind. Damit leistet diese Arbeit einen wichtigen Beitrag zum generellen physikalischen Verständnis von Fluid-induzierter Seismizität.

CONTENTS

List of Figures

List of Tables

CHAPTER 1

INTRODUCTION

Clean, reliable energy and its sustainable production is a contemporary issue. For the transition from fossil to renewable energy, the production of natural gas is of great importance as it causes significantly less carbon dioxide (CO_2) than coal or oil and can thus be considered as a transition technology. Besides traditional gas production, the process of hydraulic fracturing is becoming increasingly important. With this technique, hydrocarbons are produced from shales by high-pressure fluid injection. A promising future technology is the use of EGS (enhanced geothermal systems) to produce steam from reservoirs in several kilometers depth in the earth's crust for heat and electricity production. A third technology to reduce the human CO_2 footprint is the sequestration of CO_2 into the earth's crust.

All three techniques require the injection or production of fluids from/into the subsurface, thus influencing the natural stress field of the earth. Therefore, such activities are frequently accompanied by small earthquakes, known as microseismicity. Typically, magnitudes of induced events are too small to be felt at the surface, but several cases of larger induced magnitudes are known, for instance, the 2017 Pohang M_W5.4 earthquake [Grigoli *et al.*, 2018] that injured 82 people and caused a multi-million economic loss. In practice, operators try to mitigate this risk for example by using safety precautions, such as traffic light systems. However, seismic activity also provides a unique tool to understand the physical processes induced by the stimulation. For this understanding highly accurate velocity models, hypocenter locations and source mechanisms are essential. Based on this information geomechanical models can be created. This work attempts to contribute to the understanding of microseismicity caused by fluid injection focusing on the case of gas production by hydraulic fracturing (HF).

Following an introduction, I discuss the influence of structural anisotropy on source mechanisms and radiation patterns of microseismic sources in the second chapter of this work. Most of this material is published in Boitz *et al.* [2018]. Seismic source mechanisms are usually plotted as beachballs that visualize the stress distribution in the source. Since HF is typically performed in shales that are often highly anisotropic,

this effect needs to be taken into account to correctly describe the deformation in the source. Further, I propose a technique to remove the impact of anisotropy from the radiation pattern. This allows to plot beachballs that directly correspond to the deformation of the source mechanisms that potentially provide significantly more coherent source mechanisms.
Because typical faulting is predominately double-couple, I develop a new type of moment tensor decomposition and source type plot for such sources in the third chapter. This new source type plot has, in contrast to previous source type plots, half-moon [1] faulting as an additional end-member and is more convenient to distinguish different types of faulting induced by hydraulic fracturing. Additionally to the theoretical derivation, I apply this new decomposition to source mechanisms from a hydraulic fracturing case study, which I present in Chapter 4.
In the fourth chapter, I elaborate on a workflow to invert for the source deformation and invert source mechanisms for more than one hundred microseismic events induced by hydraulic fracturing. The events show two dominant types of double-couple faulting that are typical for hydraulic fracturing. One group of events consists of events characteristical for the regional stress field (i.e. strike-slip faulting), the other group are half-moon events that are almost exclusively observed during hydraulic fracturing.
Although half-moon events are under tectonic conditions quite improbable they are commonly observed during hydraulic stimulation. In literature, this discrepancy has not yet been fully understood and the existing models cannot entirely explain the observations. It is also highly debated if the slip of half-moon events occurs on a vertical or the horizontal fault plane. In the fifth chapter, I propose several geomechanical models for hydraulic fracturing that can explain most of the observations from the field. This work is published in Boitz & Shapiro [2021]. I show that the fluid pressure inside the hydraulic fracture can create local stress field rotations at layer interfaces, where the lithology changes, and at the vertical and horizontal limits of the fracture, known as the fracture tips. At such locations, preferred conditions for half-moon events are created locally. In the sixth chapter, I expand the 2D modeling from Chapter 5 to the full 3D space to consider also hydraulic fracturing under strike-slip conditions. Such an approach is necessary, to explain additional features observed in the field.
Altogether I propose two new tools that can be applied to any microseismic dataset that can help to get potentially more consistent results that are a better representation of the source process. The geomechanical modeling presented in the final chapters provides new deep insights into the nature of half-moon events. This may contribute to improved stimulation designs and improved safety that is inevitable to increase the public acceptance of hydraulic fracturing.

[1] The term 'half-moon faulting' is frequently used in the microseismic community to either describe a vertical slip on a vertical fault plane or a horizontal slip on a horizontal fault plane. The term is in detail discussed in section 5.1.1 on page 67.

CHAPTER 2

MICROSEISMIC SOURCES IN ANISOTROPIC MEDIA

2.1 Introduction to Elastic Media and Microseismic Sources

Seismic source mechanisms and the energy they radiate have been intensively studied by many authors over the past decades. The following descriptions of seismic sources and the surrounding media are nowadays widely accepted. The potency tensor as a geometrical representation of the source process was firstly introduced by Rice [1980]. This tensor describes the orientation of a fault plane and the direction of the slip on this fault plane and is thus proportional to the strain in the source. The rock mass, in which the earthquake occurs, is typically described as an elastic medium of arbitrary complexity. Typical media that are also used in this work are the isotropic medium described by two parameters, the vertical transverse isotropic (VTI) medium that can be described by two vertical velocities and three Thomsen parameters [Thomsen, 1986] and the orthorhombic medium described by 12 independent parameters [Tsvankin, 1997; Cheng *et al.*, 2012]. The energy that a seismic source radiates is usually defined as the moment tensor that depends on the source geometry and the elastic medium, the earthquake occurs in.

The propagation of seismic energy from the source to the observer is described by the elastodynamic Green's function that has a simple analytic form for homogeneous isotropic media [Shearer, 2012; Stein & Wysession, 2013]. For inhomogeneous anisotropic media such analytical solutions generally do not exist and Green's functions in a geometrical-optics approximation derived by Červený [2001] and Chapman [2004] are used.

The effect of anisotropy on the source process and on the radiation pattern has been investigated previously. One of the first authors is Vavryčuk [2005] who showed that anisotropy can cause non-DC components for pure slip sources and who described its

influences on the radiation pattern. Leaney & Chapman [2010] showed the influence of VTI-anisotropy on various source types and concluded that anisotropy should be taken into account for moment tensor inversion. Subsequently to our analysis of this subject published in Boitz *et al.* [2018], Grechka [2020b] investigated the influence of anisotropy on an arbitrarily oriented source in VTI-media.
For the description of a seismic source, numerous methods to construct and decompose potency and moment tensors were introduced. Seismic sources can be described by double-couple faulting, tensile components and isotropic components [Chapman, 2004]. An alternative representation is shown by Tape & Tape [2013] who describe the seismic source as the sum of a double-couple and a crack tensor.
Methods to decompose the full moment tensor have been shown by Hudson *et al.* [1989], who proposed two dimensionless parameters representing the volumetric and compensated-linear-vector-dipole (CLVD) components of the moment tensor and a graphical representation in the form of the diamond plot. Another classical decomposition and source type plot is the one proposed by Riedesel & Jordan [1989]. Zhu & Ben-Zion [2013] showed a modified decomposition taking also the size of an event, described by the scalar moment, into account. In this thesis, I mainly use the method of Vavryčuk [2015] to decompose the moment tensor into its double-couple (DC), volumetric (ISO) and compensated-linear-vector-dipole (CLVD) components. The most recent decomposition is the one by Chapman [2019] that proposes another new type of projection. All these decompositions are tools to visualize different seismic sources. Chapman & Leaney [2012] introduced another slightly different way of moment tensor decomposition and showed a 3D visualization of the source process. They proposed to visualize the source mechanism in the form of two disks, which are shifted to each other. However, for this type of visualization one needs additional information for example about the stress state to solve the ambiguity of the source mechanism.
In this chapter, I firstly summarize the theoretical basis for the parameterization of elastic isotropic and VTI-media. Next, I describe the source process using the potency and the moment tensor and show how to compute amplitudes for these sources. Furthermore, I review two different approaches of moment tensor decomposition. I show the effect of different anisotropy parameters on the source process by writing the corresponding moment tensors explicitly and visualizing them using their radiation pattern and the Vavryčuk-diamond plot. Furthermore, I analyze the effect of anisotropy on the propagation path on the radiation pattern. Finally, I propose an alternative representation of source mechanisms in anisotropic media using their potency tensor isotropic equivalent (PTI). The chapter is a continuation of the research presented in the frame of my master's thesis [Boitz, 2016], where I analyzed the effect of the individual Thomsen parameters on the radiation patterns of different source mechanisms. The analysis and quantification of the non-DC components, the application to realistic anisotropic

media and the theoretical concept of the PTI are new scientific aspects developed in the frame of this PhD thesis. The chapter is in wording mainly equal to our work published in Boitz *et al.* [2018]. Figures 2.2 - 2.7, 2.10 - 2.11 and 2.13 are taken from Boitz *et al.* [2018], 2.1 and 2.12 are slightly modified versions of the corresponding figures from the paper. Figures 2.8 and 2.9 were not included in the original paper. I acknowledge the contributions of my co-authors, Prof. Serge Shapiro who had the initial idea to study the influence of anisotropy on microseismic sources and who developed the concept of the PTI and Dr. Anton Reshetnikov who provided several programming codes, in particular to solve the Christoffel equation.

2.2 Linear Elasticity and Definition of Elastic Media

Here, I firstly explain the concept of linear elasticity and the parameterization of different elastic media.
A solid body exposed to external stress is deformed. Depending on the applied stresses, the solid can either change its shape and/or size (see e.g. Shapiro [2015]). If the deformation is small and reversible, i.e. the body returns to its initial shape after removing the applied stress, the deformation is considered to be elastic and can be described by the concept of linear elasticity. A body typically only behaves elastically, if the deformations are small. Larger deformations result in an inelastic or plastic behavior of the solid that I do not consider in this thesis.
The concept of linear elasticity was firstly formulated in the 17th century by Robert Hooke [Hooke, 1678] and is known as Hooke's law. This law links the stress tensor σ_{ij}, describing the stresses applied to the body to its deformation, described by the strain tensor ϵ_{ij}. The linearity is described by the fourth rank stiffness tensor C_{ijkl}:

$$\sigma_{ij} = C_{ijkl}\epsilon_{kl}. \tag{2.1}$$

The 81 components of the stiffness tensor are not independent of each other, as the stiffness tensor itself is symmetric (a consequence of Equation 2.1):

$$C_{ijkl} = C_{jikl} = C_{ijlk} \tag{2.2}$$

and additionally possesses the symmetry (see e.g. Jaeger *et al.* [2007]):

$$C_{ijkl} = C_{klij}. \tag{2.3}$$

This reduces the maximum number of independent parameters of the stiffness tensor to 21 (a triclinic medium). The symmetry makes it possible to convert the fourth rank

stiffness tensor C_{ijkl} into a second rank symmetric (6x6) tensor C_{IJ} using the contracted, sometimes also called 'Voigt' notation, by converting indices ij to I (or respectively kl to J) as follows:

ij	11	22	33	23	13	12
	↓	↓	↓	↓	↓	↓
I	1	2	3	4	5	6

In this work, I use the two simplest elastic media, the isotropic and the vertical transverse isotropic medium that can be described by two or respectively five independent parameters.

2.2.1 Isotropic Medium

An isotropic medium is defined by only two independent parameters. Typically, the stiffness tensor is defined by the Lamé-parameters λ and μ, which is also called the shear modulus. The stiffness tensor expressed by these two quantities then reads [Aki & Richards, 2002]:

$$C_{ijkl} = \lambda\delta_{ij}\delta_{kl} + \mu\left(\delta_{ik}\delta_{jl} + \delta_{il}\delta_{jk}\right), \tag{2.4}$$

where δ is the Kronecker symbol, which is 1 if indexes i and j are equal and otherwise zero. Alternatively, rock properties are frequently expressed in terms of Young's modulus E and Poisson's ratio ν (see also Chapter 5) that are related to the Lamé-parameters as follows (see e.g. [Sheriff & Geldart, 1995]):

$$E = \mu\left(\frac{3\lambda + 2\mu}{\lambda + \mu}\right) \tag{2.5}$$

$$\nu = \frac{\lambda}{2\left(\lambda + \mu\right)}. \tag{2.6}$$

2.2.2 Vertical Transverse Isotropic (VTI) Medium

The second type of medium used in this thesis is the vertical transverse isotropic medium that is typically described by the vertical P and S-wave velocities, v_{PV} and v_{SV}, and the three Thomsen parameters, ϵ, γ and δ [Thomsen, 1986], which quantify the degree of anisotropy:

$$\epsilon = \frac{C_{11} - C_{33}}{2C_{33}} = \frac{v_{PH}^2 - v_{PV}^2}{2v_{PV}^2} \tag{2.7}$$

$$\gamma = \frac{C_{66} - C_{44}}{2C_{44}} = \frac{v_{SH}^2 - v_{SV}^2}{2v_{SV}^2} \tag{2.8}$$

$$\delta = \frac{(C_{13} + C_{44})^2 - (C_{33} - C_{44})^2}{2C_{33}(C_{33} - C_{44})}. \tag{2.9}$$

Using the definitions of the vertical velocities and the Thomsen parameters (Equations 2.7 - 2.9), one can express the components of the stiffness tensor **C** as:

$$C_{33} = v_{PV}^2 \rho \tag{2.10}$$

$$C_{44} = v_{SV}^2 \rho \tag{2.11}$$

$$C_{11} = C_{33}\,(2\epsilon + 1) \tag{2.12}$$

$$C_{66} = C_{44}\,(2\gamma + 1) \tag{2.13}$$

$$C_{13} = C_{23} = \sqrt{2\delta C_{33}\,(C_{33} - C_{44}) + (C_{33} - C_{44})^2} - C_{44} \tag{2.14}$$

$$C_{12} = C_{11} - 2C_{66}. \tag{2.15}$$

The stiffness tensor for a VTI medium then has the following form:

$$C_{IJ} = \begin{pmatrix} C_{11} & C_{12} & C_{13} & 0 & 0 & 0 \\ C_{12} & C_{11} & C_{13} & 0 & 0 & 0 \\ C_{13} & C_{13} & C_{33} & 0 & 0 & 0 \\ 0 & 0 & 0 & C_{44} & 0 & 0 \\ 0 & 0 & 0 & 0 & C_{44} & 0 \\ 0 & 0 & 0 & 0 & 0 & C_{66} \end{pmatrix}. \tag{2.16}$$

2.3 Description of Source Mechanisms

After having briefly introduced Hooke's law, the stress, strain and stiffness tensor, I consider in the following the deformation caused by a point-like earthquake.

2.3.1 Geometrical Description of the Source - the Potency Tensor

An earthquake as a seismic source can be characterized using the normal unit vector of the fault plane **n** and a non-unit slip vector **s**. Multiplied element-wise, as shown in Equation 2.17, they form the potency or source tensor **p**, (see e.g. [Rice, 1980; Shapiro,

2015]).

$$p_{ij} = \frac{1}{2}(n_i s_j + n_j s_i). \tag{2.17}$$

In literature, the tensor p_{ij} is frequently called the potency density tensor [Segall, 2010]. In the case of an earthquake of a finite rupture length, this tensor characterizes a surface element of the rupture. In the following, I consider microseismic events, which can be approximated by point-like sources. Thus, I omit the word 'density' in the notation of this tensor.
The potency tensor can be expressed in contracted notation in a vector form:

$$p_I = \begin{pmatrix} p_1 \\ p_2 \\ p_3 \\ p_4 \\ p_5 \\ p_6 \end{pmatrix} = \begin{pmatrix} p_{11} \\ p_{22} \\ p_{33} \\ 2p_{23} \\ 2p_{13} \\ 2p_{12} \end{pmatrix}. \tag{2.18}$$

This representation follows from the fact that the potency tensor reflects the strain in the source due to co-seismic deformations. Thus, its contracted notation is equivalent to the one of the strain tensor. Because this strain defines the geometry of the source, it is important to visualize it. If the angle between the two vectors **n** and **s** is 90°, the sum of the diagonal elements (p_{ii}) is zero and the source is a 'pure slip' one. In this case, the unit potency tensor normalized to the length of the slip |**s**| can be described by three angles defining the dip, the azimuthal orientation of the fault plane and the slip direction on this fault plane. The definition of these three angles and their relation to the potency tensor are shown in Chapter 3. If the angle differs from 90° the source mechanism has also a volumetric component which can be interpreted as opening or closing of a preexisting crack. In this case, a fourth parameter describing the angle between **n** and **s** has to be introduced. These sources then describe tensile faulting. A geometrical description of a seismic source using only **n** and **s** covers not all types of faulting. It cannot be used for isotropic explosion or implosion source strain. To define a full potency tensor an additional isotropic correction term must be added, see [Chapman, 2004]:

$$p_{ij}^{full} = p_0 \delta_{ij} + p_{ij}. \tag{2.19}$$

In the case of $p_{ii} = 0$, p_0 denotes the size of the isotropic component, δ_{ij} is the Kronecker symbol. To define the full p_{ij} six parameters are needed. In addition to the four angles mentioned above, these are the quantities $|\bar{\mathbf{s}}|$ and p_0.
For the illustrations in this chapter, I use four pure slip source mechanisms, strike-slip, normal and thrust faulting (both on a strictly 45° inclined fault plane) and dip-slip

faulting on a vertical fault plane. This event type, frequently called half-moon event, is discussed in detail in Chapter 5.
The potency tensors of these sources composed of unit vectors $\hat{\mathbf{n}}$ and $\hat{\mathbf{s}}$ can be found in Table 2.1. Their corresponding isotropic radiation patterns (see section 2.4.1) are displayed in Figure 2.1.

Strike-Slip	Normal Fault	Thrust Fault	Vertical Dip-Slip
$\hat{\mathbf{n}} = (1\ 0\ 0)$ $\hat{\mathbf{s}} = (0\ 1\ 0)$	$\hat{\mathbf{n}} = \frac{1}{\sqrt{2}}(1\ 0\ 1)$ $\hat{\mathbf{s}} = \frac{1}{\sqrt{2}}(1\ 0\ -1)$	$\hat{\mathbf{n}} = \frac{1}{\sqrt{2}}(1\ 0\ 1)$ $\hat{\mathbf{s}} = \frac{1}{\sqrt{2}}(-1\ 0\ 1)$	$\hat{\mathbf{n}} = (1\ 0\ 0)$ $\hat{\mathbf{s}} = (0\ 0\ 1)$
$p_{ij} = \frac{1}{2}\begin{pmatrix} 0 & 1 & 0 \\ 1 & 0 & 0 \\ 0 & 0 & 0 \end{pmatrix}$	$p_{ij} = \frac{1}{4}\begin{pmatrix} 1 & 0 & 0 \\ 0 & 0 & 0 \\ 0 & 0 & -1 \end{pmatrix}$	$p_{ij} = \frac{1}{4}\begin{pmatrix} -1 & 0 & 0 \\ 0 & 0 & 0 \\ 0 & 0 & 1 \end{pmatrix}$	$p_{ij} = \frac{1}{2}\begin{pmatrix} 0 & 0 & 1 \\ 0 & 0 & 0 \\ 1 & 0 & 0 \end{pmatrix}$

Table 2.1: Unit potency tensors $\mathbf{p}$ for strike-slip faulting, normal and thrust faulting (on a 45° inclined fault plane) and vertical dip-slip faulting.

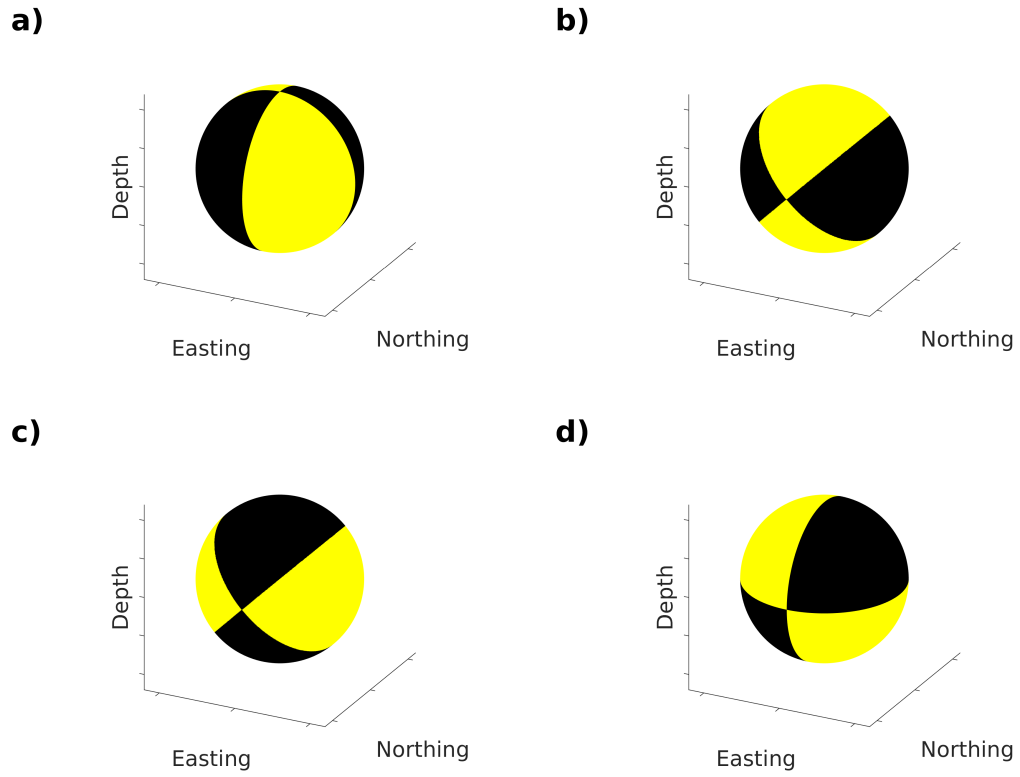

Figure 2.1: Radiation pattern in isotropic media of **a)** strike-slip faulting, **b)** normal faulting, **c)** thrust faulting and **d)** dip-slip faulting on a vertical fault plane (see definition of source mechanisms in Table 2.1). The strike direction of the fault plane is in N-direction (i.e. a strike of 0°) for all mechanisms.

2.3.2 Moment Tensor

Using the Thomsen parameters one can compute the stiffness tensor of the elastic medium, see Equations 2.10 - 2.15. If the stiffness tensor is multiplied with the potency tensor we obtain a quantity that describes the forces acting in the source [Chapman, 2004; Shapiro, 2015]. In the case of an earthquake with a finite rupture area A this quantity expresses a surface density of the so-called moment tensor. The moment tensor **M** is given by a product of this quantity with the rupture area (more generally, a corresponding surface integral):

$$M_{ij} = C_{ijkl} \cdot p_{kl} \cdot A. \tag{2.20}$$

Here and everywhere in the chapter, Einstein summation over repeating indices is implied. In this equation, $C_{ijkl} \cdot p_{kl}$ expresses an averaged surface density of the moment tensor. In contracted notation (see Equation 2.18) Equation 2.20 takes the following form:

$$M_I = C_{IJ} \cdot p_J \cdot A. \tag{2.21}$$

In this computation one creates, what I call in the following, **source anisotropy** by multiplying the potency tensor with an anisotropic stiffness tensor.
Using this method, I am able to compute the moment tensor for an arbitrarily orientated source in anisotropic media. These moment tensors will be later analyzed using their radiation pattern and their moment tensor decomposition.

2.4 Visualization of Seismic Sources

2.4.1 Radiation Pattern

In this chapter, I focus on the influence of different sources and media on the distribution of P-wave polarity. Here, I use the terms radiation pattern, beachball and P-wave polarity as synonyms to describe the distribution of positive and negative polarity radiated by a seismic source.
To analyze the radiation pattern one has to compute the displacement at each point on a sphere surrounding the source. For this, a relation is needed that describes the displacement **u** at any position which is caused by a source described by the moment tensor. The function describing this relation is the elastodynamic Green's function **G**. It provides the displacement **u** at a receiver in the far-field of a point event of the moment

M:

$$u_i = G_{ijk}\dot{M}_{jk} \tag{2.22}$$

$$u_i = G_{ijk}\frac{dM_{jk}}{dt}, \tag{2.23}$$

where $\dot{M}_{jk}$ is the temporal moment rate. Here and in Chapter 4, I use a Green's function in a geometrical-optics approximation derived from Chapman [2004] (Equation 5.4.27). It can be found in a similar notation in [Yu *et al.*, 2016]. This function can be written as

$$u_k(\mathbf{x}_R, \mathbf{x}_S) = \frac{\hat{g}_k^R(\hat{g}_i^S\,\hat{p}_j^S + \hat{g}_j^S\,\hat{p}_i^S)}{8\pi c_S^2 R(\mathbf{x}_R, \mathbf{x}_S)\,\sqrt{\rho_R\rho_S V_R V_S}}\frac{M_{ij}}{T_r}, \tag{2.24}$$

where T_r is the rupture time. Here, $\mathbf{x}_R$ and $\mathbf{x}_S$ denote the receiver and source position, $\hat{g}^R$ and $\hat{g}^S$ are unit polarization vectors at source and receiver and $\hat{p}^S$ is the unit phase slowness vector. The scaling terms in the denominator, the phase velocity c_S, the effective raypath length R, the density ρ and the group velocity V have an impact on the amplitude, but not on the polarity of the wave. In homogeneous anisotropic media, all these parameters can be obtained from solving the Christoffel equation using the stiffness of the medium and a propagation direction. In homogeneous anisotropic media, the polarization vector and the slowness vector can deviate from each other for certain directions, whereas for isotropic media these vectors always coincide for P-wave.
In general inhomogeneous anisotropic media, the polarization vectors at source and receiver can additionally be different. This is the case if the ray from the source to the receiver is deviated due to changes in the elastic parameters. In this case, polarizations cannot be computed analytically but are calculated numerically by two-point raytracing algorithms. I do not take into account this effect here, since I consider in this chapter only sources in homogeneous anisotropic media, but this effect is taken into account for the moment tensor inversion in Chapter 4. The deviation between slowness and polarization of P-wave can cause significant changes in the polarity and amplitude distribution in the radiation pattern. This effect is called in the following **propagation anisotropy effect**.
Using this framework it is possible to separate the effects of source anisotropy from propagation anisotropy. Later, I show radiation patterns for both cases and for the combined anisotropic source and propagation case.

2.4.2 Moment Tensor Decomposition

Visualizing of non-DC moment tensors is frequently done using the decomposition of the moment tensor **M** into its double-couple (DC), volumetric (ISO) and compensated-linear-vector-dipole (CLVD) components. As described in the introduction, there are many similar approaches of various authors to decompose the moment tensor. I decided to use the approach of Vavryčuk [2015], who simplified the decomposition of Knopoff & Randall [1970]. The moment tensor is a symmetric tensor that can be decomposed into its eigenvalues ($M_1 \geq M_2 \geq M_3$) and an orthonormal set of its eigenvectors ($\mathbf{e}_1$,$\mathbf{e}_2$,$\mathbf{e}_3$):

$$\mathbf{M} = M_1\mathbf{e}_1\mathbf{e}_1^T + M_2\mathbf{e}_2\mathbf{e}_2^T + M_3\mathbf{e}_3\mathbf{e}_3^T. \tag{2.25}$$

The components of the moment tensor can then be expressed as follows [Vavryčuk, 2015]:

$$M_{ISO} = \frac{1}{3}(M_1 + M_2 + M_3) \tag{2.26}$$

$$M_{CLVD} = \frac{2}{3}(M_1 + M_3 - 2M_2) \tag{2.27}$$

$$M_{DC} = \frac{1}{2}(M_1 - M_3 - |M_1 + M_3 - 2M_2|). \tag{2.28}$$

However in general practice it is easier to evaluate components scaled to the scalar seismic factor M:

$$\begin{bmatrix} C_{ISO} \\ C_{CLVD} \\ C_{DC} \end{bmatrix} = \frac{1}{M}\begin{bmatrix} M_{ISO} \\ M_{CLVD} \\ M_{DC} \end{bmatrix}, \tag{2.29}$$

where M is defined as:

$$M = |M_{ISO}| + |M_{CLVD}| + M_{DC}. \tag{2.30}$$

The scaled factors C_{ISO}, C_{CLVD} and C_{DC} then satisfy the following equation:

$$|C_{ISO}| + |C_{CLVD}| + C_{DC} = 1. \tag{2.31}$$

Using these definitions, C_{DC} is always positive between 0 and 1 and C_{CLVD} and C_{ISO} can vary in a range between -1 and 1. These factors can be easily displayed and evaluated using the diamond source type plot proposed by Vavryčuk [2015]. This plot shows the source mechanism in the C_{CLVD}-C_{ISO}-coordinate system. The percentage of the C_{DC}-component is displayed by color intensity. This means that source mechanisms with pure double-couple sources plot in the origin of the coordinate system, explosion and

implosion sources plot at the top and bottom of the diamond and sources with high CLVD components at the left and right side of the diamond.
This source type plot can be used to evaluate both, potency tensor **p** and moment tensor **M**. For demonstrations I use pure slip sources that moment tensors would exhibit double-couple faulting in isotropic media. In order to show the effect of anisotropy, I here use anisotropic stiffness tensors to compute the moment tensor. These moment tensors which are, due to anisotropy, non-pure double-couple sources are then evaluated using the moment tensor decomposition and the diamond plot.
Another type of moment tensor decomposition was proposed by Hudson *et al.* [1989]. He also uses the sorted eigenvalues ($M_1 \geq M_2 \geq M_3$) of **M** to compute a horizontal projection u and a vertical projection v on a skewed diamond. These two parameters are defined as:

$$u = \frac{2\,(M_1 + M_3 - 2M_2)}{3max\,(|M_1|, |M_2|, |M_3|)} \tag{2.32}$$

$$v = \frac{M_1 + M_2 + M_3}{3max\,(|M_1|, |M_2|, |M_3|)} \tag{2.33}$$

and can vary in the range of

$$-\frac{4}{3} \leq u \leq \frac{4}{3} \quad and \quad -1 \leq v \leq 1 \tag{2.34}$$

In the skewed-diamond plot explosion and implosion sources plot similarly as in the Vavryčuk plot at the top and bottom of the skewed diamond. The major difference is that sources with pure negative CLVD components plot at [1, 0] and pure positive CLVD sources plot at [-1,0]. Furthermore, the Hudson-plot exhibits a uniform probability density distribution for a uniform distribution of eigenvalues, which is not the case in the Vavryčuk plot.
For comparison, I show for one example also this original Hudson plot [Hudson *et al.*, 1989] (Figure 2.7). As the visualization of Vavryčuk [2015] is simpler and more practical for the approach here, I concentrate on this visualization to evaluate the influence of anisotropy on the moment tensor.

2.5 Results of Anisotropic Source Modeling

2.5.1 Anisotropic Source

For this section, I simulate an anisotropic source and assume the propagation to be isotropic. Therefore, I individually examine the effects of ϵ, δ and γ for a constant

V_{P0}/V_{S0}-ratio of $\sqrt{3}$, i.e. a Poisson solid in the isotropic limit. For this, I vary one of the Thomsen parameters and set the other two to zero.
Strike-slip mechanisms are not affected by anisotropy. To understand this better, I express the moment tensor of a strike-slip source in the contracted notation form (Equation 2.21):

$$M_I = C_{IJ} \cdot (0, 0, 0, 0, 0, 1)^T \cdot |\bar{s}| \cdot A. \tag{2.35}$$

In comparison to normal or thrust faulting the potency tensor has only one non-zero component. This component is multiplied with the C_{66} component of the stiffness tensor, which depends on γ (Equations 2.8 and 2.50). However, this scales only the whole moment tensor with respect to the potency tensor. So the effect could be observed in the values of the moment tensor but not in the radiation pattern. All other components of the elasticity tensor which are affected by anisotropy are multiplied with zero elements in the strike-slip potency tensor.
The same is true for the half-moon event. If one rewrites the potency tensor of the half-moon event in Table 2.1 in contracted notation (Equation 2.21) it has the following form:

$$M_I = C_{IJ} \cdot (0, 0, 0, 0, 1, 0)^T \cdot |\bar{s}| \cdot A. \tag{2.36}$$

Here, the only non-zero element of the potency tensor is multiplied with the C_{44} component that is independent of all three Thomsen parameters. This result can be generalized for any dip-slip event with arbitrary strike direction of the vertical plane, as these events are only described by p_4 and p_5. Thus, any event of half-moon type is not affected by VTI-anisotropy.
Note that this effect is due to the fact that the symmetry axis of the VTI medium (i.e. vertical direction) lies in the same plane as the fault plane. A detailed discussion of the dependence of the angle between the fault plane and the symmetry axis can be found in section 2.5.1.
However, elastic anisotropy at the source location has a significant impact on the moment tensor and the radiation pattern for normal and reverse faulting (also compare to Figure 2.1b). To illustrate this effect, I show in Figures 2.2 and 2.3 the effect of the individual Thomsen parameters on a normal faulting source. For a better understanding I additionally show the corresponding moment tensors next to the radiation patterns. The impact on thrust and normal faulting mechanisms are opposed. Note that I only consider normal and thrust faulting on a strictly 45° degree inclined fault plane in this chapter. The potency tensors for normal and thrust faulting in contracted notation read as follows:

$$p_{normal} = \frac{1}{2}(0.5, 0, -0.5, 0, 0, 0)^T \cdot |\bar{s}| \tag{2.37}$$

$$p_{thrust} = \frac{1}{2}(-0.5, 0, 0.5, 0, 0, 0)^T \cdot |\bar{s}|. \tag{2.38}$$

Because of linear elasticity, the sum of these normal thrust faulting moment tensors is zero for any anisotropic, as well as isotropic, medium:

$$M_{ij}^{thrust} = -M_{ij}^{normal}. \tag{2.39}$$

As strike-slip and half-moon events are not affected by anisotropy and the effect on normal and thrust faulting are opposed, I investigate in the following only the impact of the anisotropy on normal faulting sources. For this, I compute the moment tensor for normal faulting sources as a function of the individual Thomsen parameters.
These moment tensors are then decomposed into their CLVD, ISO and DC components using Equations 2.25 - 2.31. Since I use normal faulting sources for our demonstration, the decomposition is significantly simpler, because the moment tensor is already in a diagonal form, so that the main diagonal elements can be directly used as the eigenvalues of **M**.

Effect of ϵ

The moment tensor for a medium with $\delta = \gamma = 0$ can be expressed as:

$$M_I = \begin{pmatrix} \alpha^2(2\epsilon+1) & \alpha^2(2\epsilon+1)-2\beta^2 & \alpha^2-2\beta^2 & 0 & 0 & 0 \\ \alpha^2(2\epsilon+1)-2\beta^2 & \alpha^2(2\epsilon+1) & \alpha^2-2\beta^2 & 0 & 0 & 0 \\ \alpha^2-2\beta^2 & \alpha^2-2\beta^2 & \alpha^2 & 0 & 0 & 0 \\ 0 & 0 & 0 & \beta^2 & 0 & 0 \\ 0 & 0 & 0 & 0 & \beta^2 & 0 \\ 0 & 0 & 0 & 0 & 0 & \beta^2 \end{pmatrix} \begin{pmatrix} p_{11} \\ p_{22} \\ p_{33} \\ 2p_{23} \\ 2p_{13} \\ 2p_{12} \end{pmatrix}. \tag{2.40}$$

Here and in the following, I omit the factor $|\bar{s}| \cdot A$. The moment tensor for a normal faulting source in contracted notation then looks like this:

$$M_I^{normal} = \frac{1}{2}\left(\alpha^2\epsilon + \beta^2, \alpha^2\epsilon, -\beta^2, 0, 0, 0\right)^T. \tag{2.41}$$

ϵ affects the M_{11} and M_{22} component. This means that negative ϵ decreases M_{11} and M_{22} for normal faulting mechanisms and increases both components for thrust faulting mechanisms. For both mechanisms the absolute values of M_{11} decrease. In the radiation

pattern this leads to nearly circular areas of the same polarity along the y-(easting)axis. For positive ϵ the absolute values of M_{11} and M_{22} are increased. This means for normal faulting that one obtains positive forces in horizontal directions, confirmed by the positive polarity in the radiation pattern and for thrust faulting mechanisms negative forces. Because the force in x-direction is larger compared to the force in y-direction and the force in vertical direction remains constant we see elliptic areas of the same polarity at the top and bottom of the radiation pattern. This effect can be also observed in the radiation patterns in the first columns of Figures 2.2 and 2.3.
Because the moment tensor is already in a diagonal form, one can directly use its eigenvalues:

$$M_1 = \frac{1}{2}(\alpha^2\epsilon + \beta^2) \qquad M_2 = \frac{1}{2}(\alpha^2\epsilon) \qquad M_3 = -\frac{1}{2}\beta^2 \tag{2.42}$$

to compute the ISO and CLVD components of the Vavryčuk decomposition:

$$M_{ISO} = \frac{1}{3}\alpha^2\epsilon \qquad M_{CLVD} = -\frac{1}{3}\alpha^2\epsilon. \tag{2.43}$$

The M_{DC} component depends on the sign of ϵ:

$$\epsilon > 0 : M_{DC} = \frac{1}{2}\beta^2 \qquad \epsilon < 0 : M_{DC} = \frac{1}{2}(\beta^2 + \alpha^2\epsilon). \tag{2.44}$$

The ratio between M_{ISO} and M_{CLVD} is equal to minus one. This leads to points on a line with 45° inclination with respect to the coordinate axes (Figure 2.4). The effect is much stronger for negative ϵ. This is because the scalar factor M (Equation 2.30) decreases for negative ϵ because the M_{DC} decreases (Equation 2.44).
For comparison, I plot also the classical Hudson diamond in Figure 2.7 for the same source mechanisms and media as in Figure 2.4. Both show coinciding results (negative CLVD and positive ISO components for positive ϵ and the opposite for negative ϵ). However, the classic Hudson plot is less intuitive to read (e.g. negative CLVD for positive x-values) as in the case of the Vavryčuk-diamond plot. This shows the great advantage of the decomposition of Vavryčuk and explains why I use his approach here.

Effect of δ

For a medium where only δ is a free parameter, the moment tensor looks like this:

$$M_I = \begin{pmatrix} \alpha^2 & \alpha^2-2\beta^2 & \sqrt{\xi}-\beta^2 & 0 & 0 & 0 \\ \alpha^2-2\beta^2 & \alpha^2 & \sqrt{\xi}-\beta^2 & 0 & 0 & 0 \\ \sqrt{\xi}-\beta^2 & \sqrt{\xi}-\beta^2 & \alpha^2 & 0 & 0 & 0 \\ 0 & 0 & 0 & \beta^2 & 0 & 0 \\ 0 & 0 & 0 & 0 & \beta^2 & 0 \\ 0 & 0 & 0 & 0 & 0 & \beta^2 \end{pmatrix} \begin{pmatrix} p_{11} \\ p_{22} \\ p_{33} \\ 2p_{23} \\ 2p_{13} \\ 2p_{12} \end{pmatrix}. \tag{2.45}$$

Here ξ is equal to $2\delta\alpha^2(\alpha^2-\beta^2)+\left(\alpha^2-\beta^2\right)^2$. The moment tensor of a normal faulting source for such a medium then reads:

$$M_I^{normal} = \frac{1}{4}\left(\alpha^2+\beta^2-\sqrt{\xi}, \alpha^2-\beta^2-\sqrt{\xi}, -\alpha^2-\beta^2+\sqrt{\xi}, 0, 0, 0\right)^T. \tag{2.46}$$

δ has an impact on the C_{13} and C_{23} component and therefore an effect on the M_{11}, M_{22}, M_{33}. Because δ is part of a square root term (Equation 2.14), the components of the moment tensor scale not linearly with δ.

For positive δ this means that the absolute values of M_{11} and M_{33} decrease and the absolute value of M_{22} increases. The sign of the components depends on the source mechanism. In the radiation pattern, this effect can be observed in the form of equal polarity along the y-z-plane (Figure 2.2). For negative values of δ the absolute values of M_{11}, M_{22} and M_{33} increase, the sign of M_{22} is equal to M_{11}. In the radiation pattern, this leads to areas of the same polarity in the horizontal plane and elliptical areas of the opposed polarity along the z-direction (Figure 2.3).

Using Equation 2.46, the eigenvalues and non-DC components are then written as:

$$M_1 = \frac{1}{4}\left(\alpha^2+\beta^2-\sqrt{\xi}\right) \qquad M_2 = \frac{1}{4}\left(\alpha^2-\beta^2-\sqrt{\xi}\right) \qquad M_3 = -\frac{1}{4}\left(\alpha^2+\beta^2-\sqrt{\xi}\right) \tag{2.47}$$

$$M_{ISO} = -\frac{1}{12}\left(-\alpha^2+\beta^2+\sqrt{\xi}\right) \qquad M_{CLVD} = \frac{1}{3}\left(-\alpha^2+\beta^2+\sqrt{\xi}\right). \tag{2.48}$$

The size of the DC component depends on the sign of δ and is given by:

$$\delta > 0 : M_{DC} = \frac{1}{2}(\alpha^2-\sqrt{\xi}) \qquad \delta < 0 : M_{DC} = \frac{1}{2}\beta^2. \tag{2.49}$$

The ratio between M_{ISO} and M_{CLVD} is -0.25, which leads to points on a line with an inclination of $\approx 14°$ with respect to the coordinate axis. For positive δ the anisotropy effect is stronger because M_{DC} and M decrease with increasing δ.

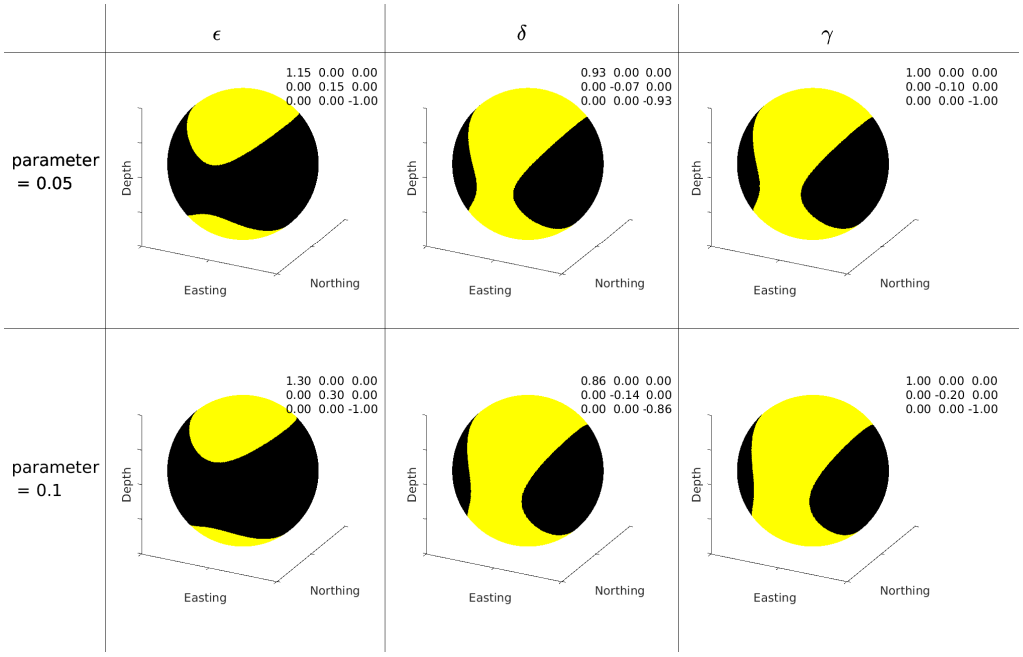

Figure 2.2: Effect of positive Thomsen parameters on the radiation pattern of a normal faulting source considering source anisotropy. First column: effect of ϵ, second column: effect of δ, third column: effect of γ. Note that reverse faulting will have the same beachballs, but with reverse colors, see Equation 2.39.

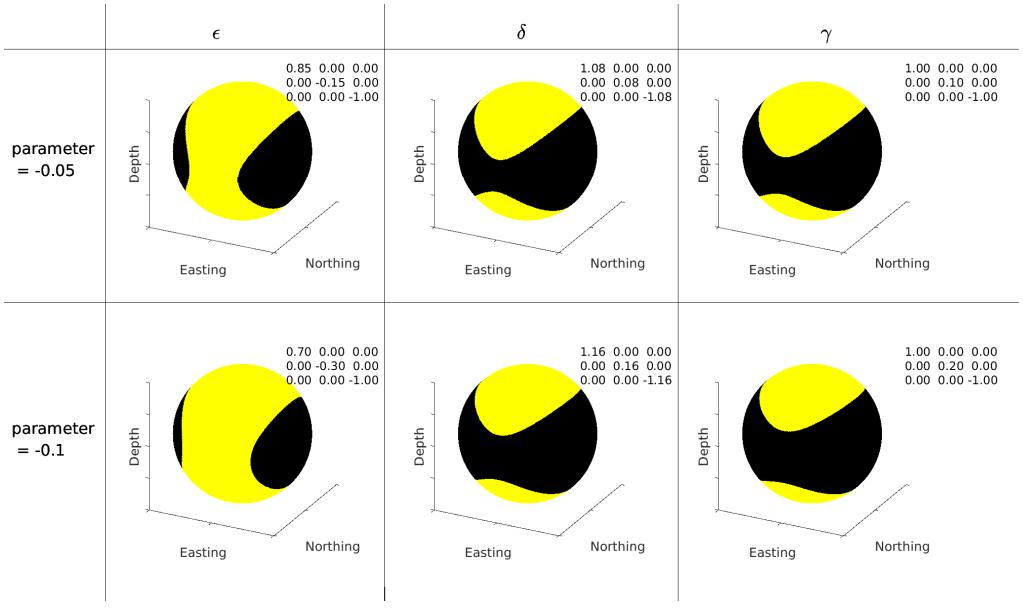

Figure 2.3: Effect of negative Thomsen parameters on the radiation pattern of a normal faulting source considering source anisotropy. First column: effect of ϵ, second column: effect of δ, third column: effect of γ. Note that reverse faulting will have the same beachballs, but with reverse colors, see Equation 2.39.

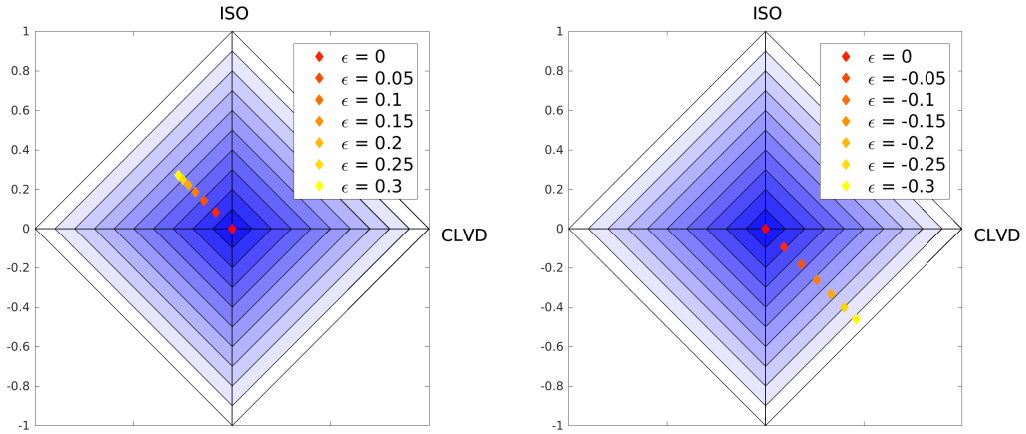

Figure 2.4: Moment tensor decomposition of a normal faulting source and a varying ϵ.

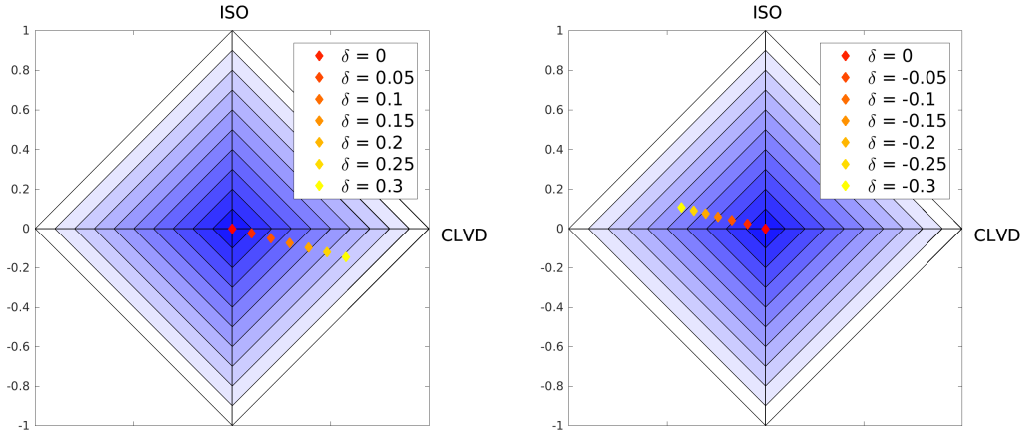

Figure 2.5: Moment tensor decomposition of a normal faulting source and a varying δ.

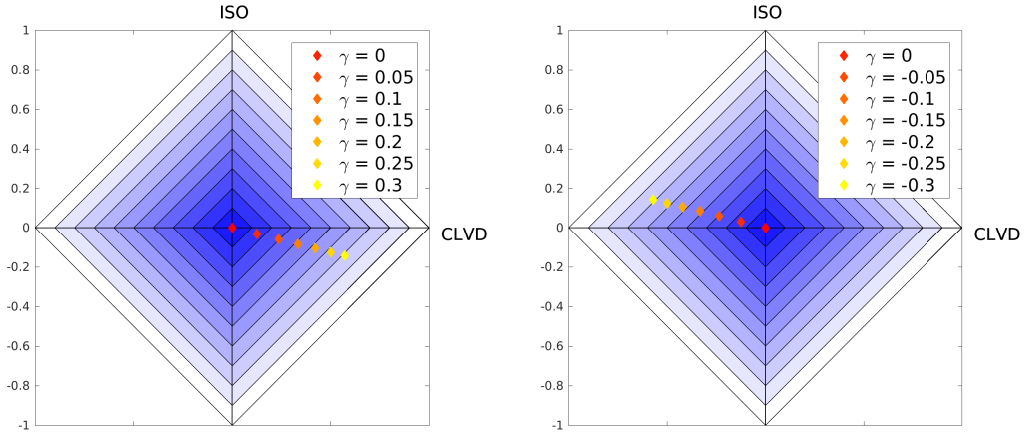

Figure 2.6: Moment tensor decomposition of a normal faulting source and a varying γ.

Effect of γ

$$M_{IJ} = \begin{pmatrix} \alpha^2 & \alpha^2 - 2\beta^2(2\gamma+1) & \alpha^2 - 2\beta^2 & 0 & 0 & 0 \\ \alpha^2 - 2\beta^2(2\gamma+1) & \alpha^2 & \alpha^2 - 2\beta^2 & 0 & 0 & 0 \\ \alpha^2 - 2\beta^2 & \alpha^2 - 2\beta^2 & \alpha^2 & 0 & 0 & 0 \\ 0 & 0 & 0 & \beta^2 & 0 & 0 \\ 0 & 0 & 0 & 0 & \beta^2 & 0 \\ 0 & 0 & 0 & 0 & 0 & \beta^2(2\gamma+1) \end{pmatrix} \begin{pmatrix} p_{11} \\ p_{22} \\ p_{33} \\ 2p_{23} \\ 2p_{13} \\ 2p_{12} \end{pmatrix}. \tag{2.50}$$

γ affects the M_{11}, M_{22} and the M_{12} component of **M**. This means that γ is the only Thomsen parameter, which directly affects the strike-slip mechanism. However, this effect cannot be seen in the polarities and therefore not in the beachball representation as it scales the whole tensor. The moment tensor of a normal faulting source for such a medium then reads:

$$M_I^{normal} = \frac{1}{2}\left(\beta^2, -2\beta^2\gamma, -\beta^2, 0, 0, 0\right)^T. \tag{2.51}$$

For normal and thrust faulting mechanisms γ influences the M_{22} component (The M_{11} component is not affected because $p_{22} = 0$) . This means that for positive γ a negative component in y-direction for normal faults and a positive component for thrust faults is generated (Figure 2.2). For negative γ the effect is opposed. In general, the influences of γ and δ on the radiation pattern are very similar, compare radiation pattern in Figures 2.2 - 2.3 and the corresponding diamond plot.
Using Equation 2.51, the eigenvalues for a varying γ are then given by:

$$M_1 = \frac{1}{2}\beta^2 \qquad M_2 = -\beta^2\gamma \qquad M_3 = -\frac{1}{2}\beta^2 \tag{2.52}$$

$$M_{ISO} = -\frac{1}{6}\beta^2\gamma \qquad M_{CLVD} = \frac{2}{3}\beta^2\gamma \tag{2.53}$$

$$\gamma > 0 : M_{DC} = \frac{1}{4}\left(\beta^2 - \beta^2\gamma\right) \qquad \gamma < 0 : M_{DC} = \frac{1}{4}\left(\beta^2 + \beta^2\gamma\right). \tag{2.54}$$

Note that this sorting of the eigenvalues is only true for media with $|\gamma|$ <0.5, which is the case for most media. This means that the ratio between M_{ISO} and M_{CLVD} is equal to -0.25, which leads to points on a line with the same inclination of $\approx 14°$ as in the case of δ (Figure 2.6).

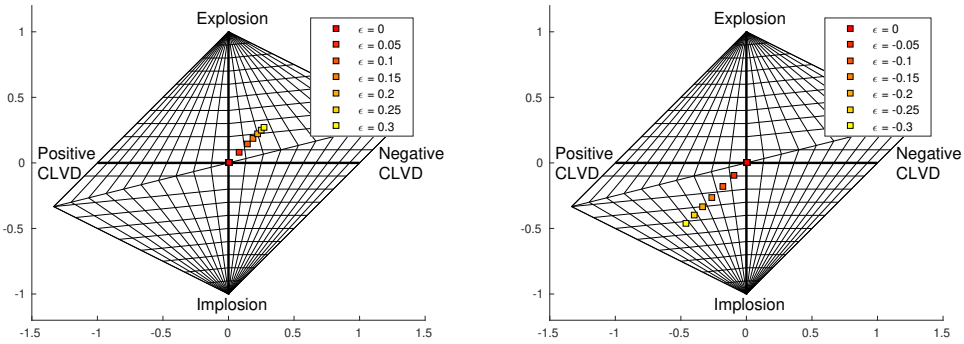

Figure 2.7: The classical Hudson-diamond plot for positive and negative ϵ. Compare also the Vavryčuk source type plot of these source mechanisms in Figure 2.4.

Dependence on Fault Plane Orientation

As explained before, half-moon and strike-slip events are not affected by anisotropy, because the fault plane has a special orientation with respect to the symmetry axis of the VTI-medium, (i.e. the symmetry axis lies in the fault plane). In the following, I briefly analyze the dependency of the angle between the fault plane and the symmetry axis on the non-DC components of the source mechanism. A detailed discussion of this subject can be found in Grechka [2020b]. For illustrations, I consider a medium with the elastic parameters of a rock layer where microseismic events were induced in Horn-River Basin (see analysis in Chapter 4) that can be found in Table 2.2.

To analyze the influence of the dip of the fault plane on the non-DC components, I take a fixed rake of -90° (i.e. normal faulting) and vary the dip in the range between 0° (horizontal faulting) and 90° (vertical dip-slip) as shown in Figure 2.8a. For 0° and 90° (i.e. for half-moon events), anisotropy has no influence on the radiation pattern, the non-DC components are zero. An increase in the dip of the fault plane from horizontal leads to an increase of both non-DC components having a maximum at 45°, which are exactly the source orientation, I considered theoretically before. Here, the DC percentage is only approximately 50%. For even steeper fault plane dips, the magnitude of the non-DC components decreases again up to 90°, where the source is purely double-couple, i.e. not influenced by anisotropy.

A similar analysis can be done for a varying rake and a fixed dip. For this, I fix the fault dip at 45° and vary the rake between -90° (normal faulting) and 90°(thrust faulting), see Figure 2.8b. For -90° the geometry is equal to the source geometry shown in Figure 2.8a for 45°. Correspondingly, the ISO, CLVD and DC components are equal. An increase in the rake leads to an increase of the DC component up to 100% for a rake of 0°, i.e. a slip in a horizontal direction. A further increase of the rake decreases the DC part of the moment tensor and creates negative ISO and CLVD components.

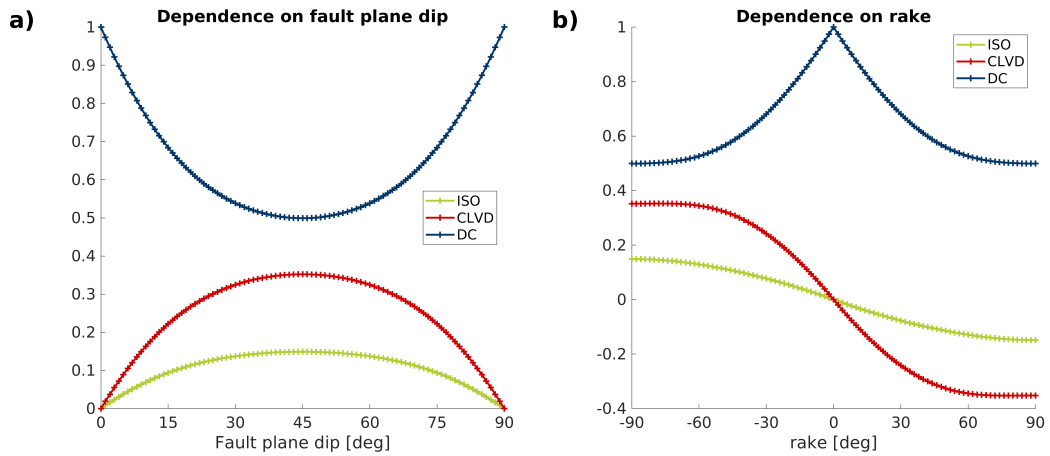

Figure 2.8: Relation between source orientation and the non-DC components created by anisotropy. **a)** Dependence on the fault plane dip for a fixed rake of -90°, **b)** dependence on the rake for a fixed dip of 45°.

This brief analysis shows that in VTI media, sources are not influenced by anisotropy if they either have a horizontal or vertical slip-orientation s or if the fault plane normal vector n is not purely vertical or horizontal. Only sources, where both vectors deviate from these directions are influenced by anisotropy.
I invert in Chapter 4 exactly such source mechanisms, half-moon and strike-slip faulting, for the dataset from Horn-River Basin. There, fault planes are not perfectly vertical though, and radiation patterns show small deviations from pure DC faulting. To theoretically model those sources here, I perturb the dip and rake values for pure strike-slip and half-moon events by normally distributed deviations from these and compute potency and moment tensors. The moment tensors are then decomposed into their ISO, CLVD and DC components, shown in Figure 2.9. Here, green diamonds correspond to sources that occurred in an anisotropic layer with parameters 'Horn-River Basin I' (Table 2.2), red diamonds correspond to the values of 'Horn-River Basin II'. Figure 2.9a shows the result for half-moon events, 2.9b the results for strike-slip events. The figure shows that the influence of anisotropy on both half-moon and strike-slip faulting for layer II is nearly zero and moment tensors show DC components larger than 90%. This can be expected since the anisotropy in this layer is rather small (Table 2.2). In the upper layer (Horn-River Basin I) that exhibits moderate degrees of anisotropy, the influence on the moment tensor is larger, leading to maximal non-DC components of 20% for half-moon events and 10% for strike-slip events. As explained before, these non-DC components are, however, significantly smaller than for a potential normal faulting earthquake in these media. In Chapter 4, I compare these results from theoretical mod-

eling with the actually inverted mechanisms (Figures 4.10 and 4.11) and show that theoretical modeling and data exhibit basically the same distribution.

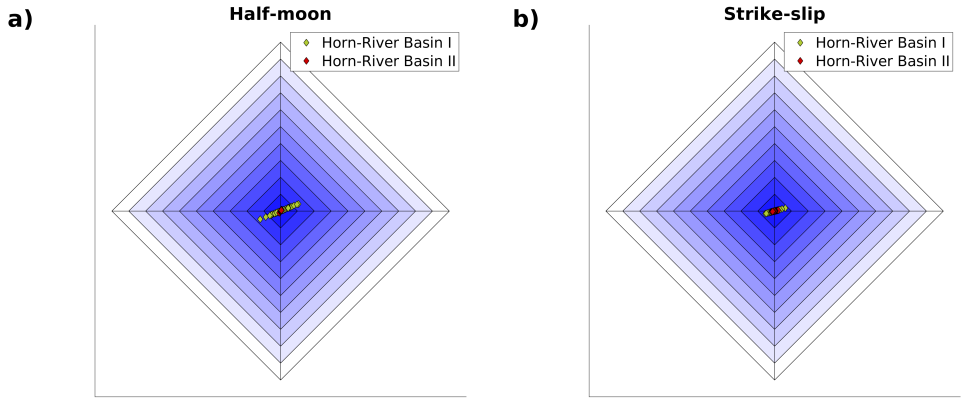

Figure 2.9: Moment tensor decomposition for sources that deviate **a)** from half-moon faulting and **b)** from strike-slip faulting theoretically occurring in anisotropic media with elastic parameters shown in Table 2.2.

2.5.2 Anisotropic Propagation

In this section, I investigate the influence on the radiation pattern coming from the wave propagation. For this, I compute a moment tensor for an isotropic source region, according to Equation 2.20. The values of these moment tensors equal exactly the potency tensors multiplied with a constant, see also Equation 2.57. Using the anisotropic ray-based Green's function (Equation 2.24), I compute the displacement for each point of the sphere. For this, I have to solve the Christoffel equation for each direction to get the polarization needed in Equation 2.24.
A closer look at Equation 2.24 shows that any deviations in polarity of the P-wave can only be caused by a deviation of the polarization vector $\hat{g}_i$ from the phase slowness vector $\hat{p}_i$.
From Equation 2.8 we know that γ does not affect the P-wave radiation pattern, because it has only an impact on SH-waves. This can be also observed in the radiation pattern for anisotropic propagation, which is equal to the isotropic beachballs for any γ. Equations 2.7 and 2.9 imply that both ϵ and δ have an impact on the polarity of the P-wave radiation pattern (Figures 2.10 and 2.11). Because a horizontal slip on a vertical fault plane causes no deviations between polarization and propagation direction of P-wave, the strike-slip mechanism is again not affected by the VTI anisotropy. The same can be shown for the half-moon faulting type.

Effect of ϵ

For positive ϵ one observes that the intersection points of the nodal surfaces are preserved. However, the nodal planes are not longer planes but exhibit a curved surface. Furthermore, the angle between these surfaces is changed and decreases in vertical direction and increases in horizontal direction. For positive ϵ the vertical P-wave velocity is smaller than the horizontal P-wave velocity. This means that the slowness tends to point more in a vertical direction than the polarization. This is what we observe in the radiation patterns (Figure 2.10). For negative ϵ the effect is opposed and one observes smaller angles between the nodal surfaces along the horizontal direction. Furthermore one has to emphasize that the effect is much stronger for negative ϵ (compare values of ϵ in Figures 2.10 and 2.11).

Effect of δ

The effect of positive and negative δ on the radiation pattern is shown in Figures 2.10 and 2.11. For δ, the intersection points of the nodal surfaces are again preserved. Furthermore, the ratio of positive and negative polarity in the radiation pattern remains constant. However, we observe that the polarity is changed along the fault surface. The borders between positive and negative polarity along the fault and auxiliary planes are not flat, but curved. For instance, for normal faulting and positive δ, we observe that the area of positive polarity near the nodal points is decreased and further away increased. The effects of positive and negative δ are opposed. Again the effect of negative δ on the radiation pattern is much stronger than for positive.

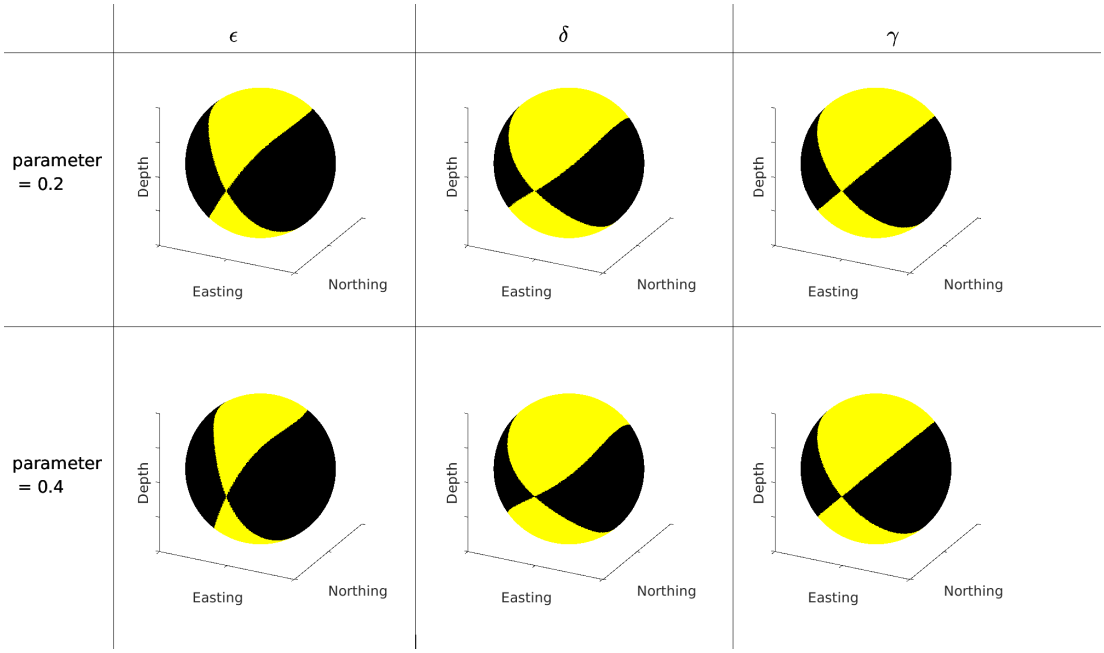

Figure 2.10: Effect of positive Thomsen parameters on the radiation pattern considering propagation anisotropy. The first column shows the effect of ϵ, the second column the effect of δ and the third column the effect of γ.

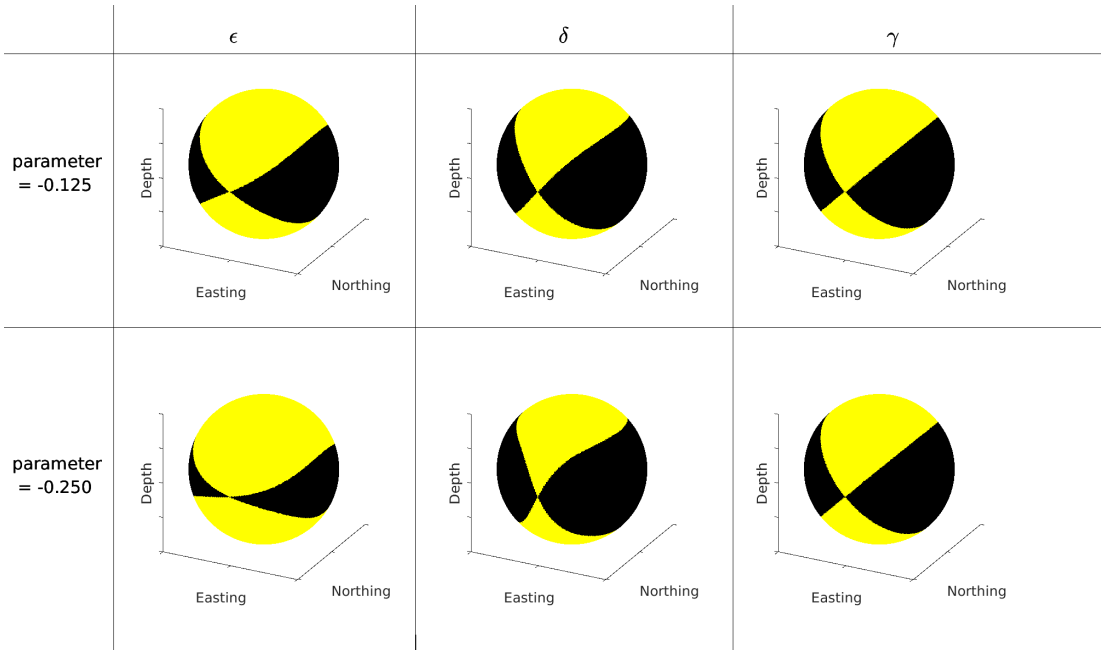

Figure 2.11: Effect of negative Thomsen parameters on the radiation pattern considering propagation anisotropy. The first column shows the effect of ϵ, the second column the effect of δ and the third column the effect of γ.

2.5.3 Analysis of Both Effects for Realistic Anisotropic Media

In the previous sections, I have shown that both source anisotropy and propagation anisotropy have an effect on the radiation pattern of normal and thrust faulting sources. The effect of propagation anisotropy is significantly smaller, but still not negligible. Therefore, I plot in this section radiation patterns which combine both effects and are a physically complete description of the source radiation pattern in anisotropic media. After having examined the effect of the individual Thomsen parameters, I here show the effect for a combination of different Thomsen parameters. For this, I use real shale data examples. As shown before the strike-slip mechanism is not affected by VTI-anisotropy and the effects on thrust and normal faulting are opposed. Therefore, I consider here only the radiation pattern for normal faulting mechanisms. Table 2.2 shows the Thomsen parameters for four different layers from two observation sites. The first two examples are the previously discussed values from Horn-River Basin that I will further consider in Chapter 4, the other two correspond to values from Barnett-shale. All examples show that also for Thomsen parameters corresponding to real media the deviation from the isotropic beachball is significant.

The first Horn-River Basin sample (Figure 2.12a) exhibits moderate degrees between 0.155 for δ and 0.3 for γ. The radiation pattern shows a larger area of positive polarity and nodal planes that do not intersect. This source exhibits approximately 50% DC faulting and 35% CLVD components and 15% volumetric components (Figure 2.12e). The radiation pattern of the second example from Horn-River Basin shows although anisotropy is quite small, notable deviations from a normal faulting source in isotropic media. These deviations are limited to an area close to the nodal points though and the general DC percentage is still larger than 90%.

The first sample from Barnett-shale exhibits moderate Thomsen parameters, which are all in a similar range. This leads to a radiation pattern (Figure 2.12c) which is very similar to the isotropic case which also coincides with a quite high DC component (around 65%) (Figure 2.12e). The second example shows the highest anisotropy, especially γ is quite high, ϵ and δ are in a similar range. This leads to high CLVD components, small DC and insignificant volumetric components (Figure 2.12e), which can be also observed in the radiation pattern (Figure 2.12d).

For all of these realistic anisotropic media, I show that anisotropy in the source and on the propagation path leads, for pure shear slip events, to moment tensors and radiation patterns that could be misinterpreted as having high non-DC faulting components, if anisotropy is not correctly considered.

Observation site	$V_{P0}[\frac{m}{s}]$	$V_{S0}[\frac{m}{s}]$	ϵ	δ	γ
Horn-River Basin I	3680	2280	0.283	0.155	0.299
Horn-River Basin II	3505	2310	0.051	0.000	0.040
Barnet-Shale I	4100	2500	0.18	0.14	0.16
Barnet-Shale II	4100	2500	0.25	0.27	0.38

Table 2.2: Thomsen parameters of four different shale rocks from two observation sites

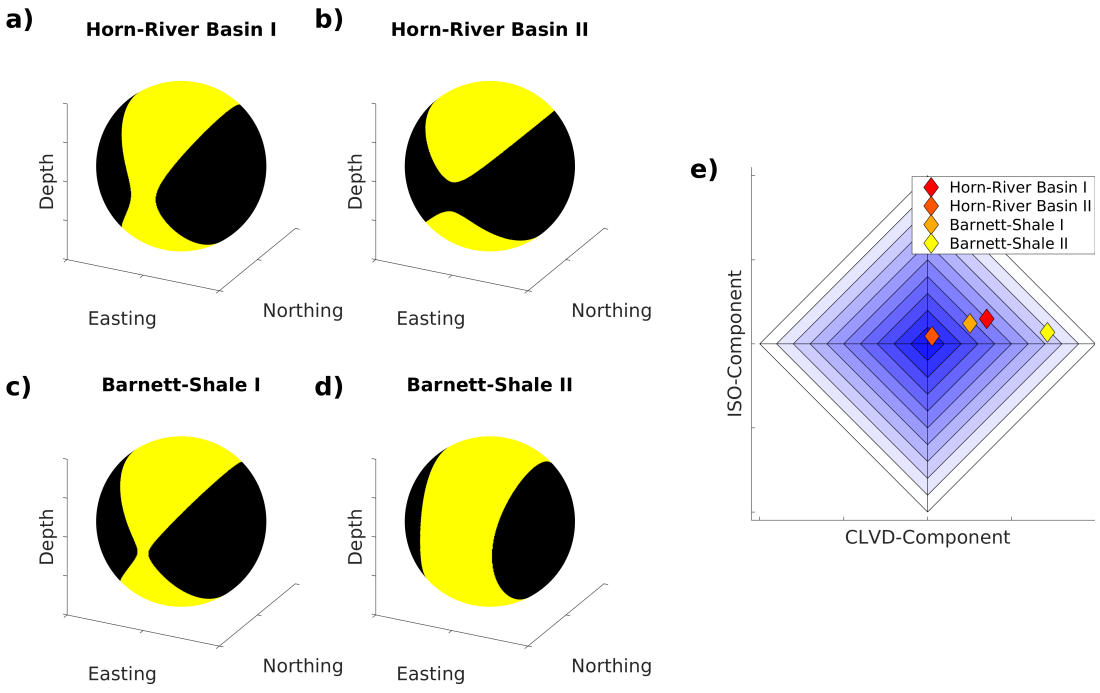

Figure 2.12: **a)** - **d)**: Radiation patterns of a normal faulting source in the four different media defined in Table 2.2, **e)** moment tensor decomposition and source type plot of these sources.

2.6 The Potency Tensor Isotropic (PTI) Equivalent Visualization

I have shown that anisotropy affects the moment tensor and therewith the radiation pattern of double-couple sources. Here, I propose a simple formulation for the moment tensor useful for visualization of earthquake sources in an arbitrary anisotropic medium. This is a standard beachball representation that keeps the symmetry and proportions of the potency tensor. Simultaneously, the proposed moment tensor corresponds to the scalar moment in the nearest isotropic equivalent medium.
I showed that each moment tensor can be computed from the potency tensor **p** and the corresponding elasticity tensor. However, for its physical interpretation, i.e. the strain in the source, it is convenient to separate the elasticity tensor into the nearest (or best fit) isotropic stiffness tensor, see [Fedorov, 1968], and the residual anisotropic (aniso) parts (denoted by superscripts "ni" and "aniso", respectively):

$$C_{ijkl} = C^{ni}_{ijkl} + C^{\Delta aniso}_{ijkl} = (\lambda^{ni}\delta_{ij}\delta_{kl} + \mu^{ni}(\delta_{ik}\delta_{jl} + \delta_{il}\delta_{jk}) + C^{\Delta aniso}_{ijkl}), \tag{2.55}$$

where λ and μ are the Lamé constants (compare Equation 2.4), δ is the Kronecker symbol and $C^{\Delta aniso}_{ijkl}$ is the difference between the isotropic and the anisotropic parts of the stiffness tensor.
If the potency tensor is multiplied with this elasticity tensor we obtain a moment tensor in the form of:

$$M_{ij} = \left(\lambda^{ni}\delta_{ij}p_{kk} + 2\mu^{ni}p_{ij} + C^{\Delta aniso}_{ijkl}p_{kl}\right) \cdot A. \tag{2.56}$$

We can see that all anisotropic effects of the elasticity tensor are concentrated in the third tensor term. The sum of all diagonal elements of the potency tensor is in the first tensor term. It is zero for a pure slip source without any volumetric component. The second term provides us with a moment tensor exactly equal to a re-scaled potency tensor. I call this the potency tensor isotropic (PTI) equivalent of the moment tensor:

$$M^{PTI}_{ij} = 2\mu p_{ij} \cdot A. \tag{2.57}$$

This moment tensor corresponds to an event of a given potency tensor in an elastic isotropic medium with the shear modulus of the nearest (best-fit) isotropic medium and λ modulus equal to zero.
The radiated displacement of P-wave corresponding to the PTI can be written explicitly. For propagation in a general isotropic medium the P-wave displacement is:

$$u^p_n = \gamma_n\gamma_i\gamma_j\frac{M_{ij}}{T_r}, \tag{2.58}$$

where γ_i is the direction cosine x_i/r. Thus, the PTI displacement reads:

$$u_n^{PTI} = \gamma_n \gamma_i \gamma_j \frac{M_{ij}^{PTI}}{T_r} \tag{2.59}$$

$$= 2\mu p_{ij} \gamma_i \gamma_j \gamma_n \frac{A}{T_r} \tag{2.60}$$

$$= 2\mu |\bar{s}| \gamma_n (\gamma_i \hat{s}_i \gamma_j \hat{n}_j) \frac{A}{T_r}. \tag{2.61}$$

Please note that under conditions of a pure-slip source and an isotropic medium this equation coincides exactly with the displacement contribution produced by the moment in Equation 2.56. However, also note that the $\mathbf{u}^{PTI}$ is valid for an arbitrary relation of **n** and **s**. The factor 2μA in Equation 2.57 provides the exact scalar moment. The PTI equivalent offers the opportunity of a very simple isotropic representation of an anisotropic moment tensor, which is cleaned from all effects of anisotropy.
For an illustration, I take the first source mechanism from Horn-River Basin (Figure 2.12a). The observed radiation pattern (Figure 2.13a) is firstly cleaned up from the propagation path effects. The radiation pattern considering only the anisotropic source is shown in Figure 2.13b. If the radiation pattern is cleaned from the anisotropic source effects as discussed above, we obtain the PTI radiation pattern as shown in Figure 2.13c.
Note that the PTI radiation pattern displays the strain within a microseismic source. If we take also the elasticity of the source medium into account (e.g. middle of Figure 2.13) the radiation pattern shows the distribution of stresses in the source.

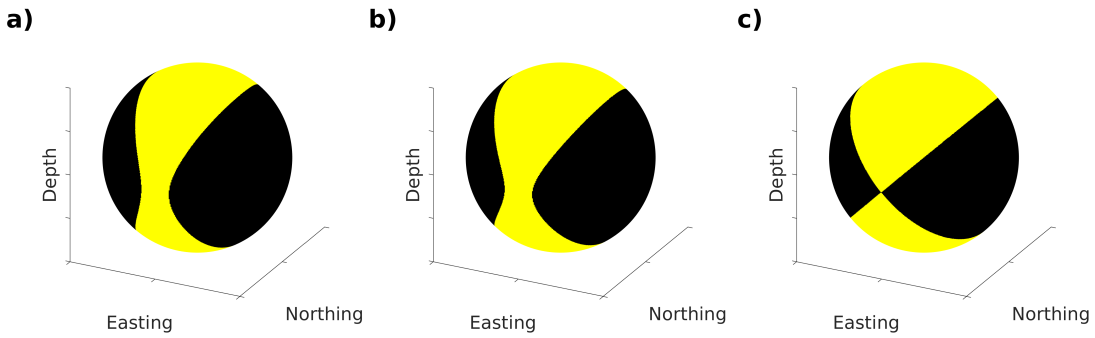

Figure 2.13: **a)** Radiation pattern as observed, **b)** radiation pattern cleaned up from propagation effect (only anisotropic source), **c)** PTI equivalent.

2.7 Summary of Microseismic Sources in Anisotropic Media

In this chapter, I have systematically investigated the effects of the Thomsen parameters on microseismic source mechanisms. By using the shown framework, I am able to separate the effects of source and propagation anisotropy. Both effects are significant, however, the effect of elastic anisotropy at the source is stronger. For both effects, I plotted the corresponding P-wave radiation patterns (beach balls) and decomposed the moment tensors. The result of both methods, the visualization in form of radiation patterns and the moment tensor decomposition are consistent. Using this workflow, I am also able to combine both effects and to take all influences of anisotropy on the source process and on the radiation of seismic energy into account. Independent of the propagation and source media, the effects of anisotropy on normal and thrust faulting events are opposed. The P-wave polarity distribution of strike-slip and half-moon events is not affected by VTI-anisotropy.

Because anisotropy can significantly modify the radiation pattern we should therefore rather invert for the potency tensor than for the moment tensor in order to retrieve source deformation of microseismic events in anisotropic environments.

Since the moment tensor and the radiation pattern of a microseismic source can be quite complex, I propose a simple way to visualize source mechanisms in arbitrary anisotropic media. For this, I use the standard beachball representation of a moment tensor that is proportional to the potency tensor and the scalar moment in the nearest isotropic equivalent medium.

In the fourth chapter, I will use the theoretical knowledge presented in this chapter to invert for potency and moment tensors of microseismic events induced by hydraulic fracturing in the Horn-River Basin and show that the effect of anisotropy also on real data is significant. Before, I propose in the next chapter a new type of moment tensor decomposition for DC sources that further decomposes the moment tensor according to the faulting geometry.

CHAPTER 3

DECOMPOSITION AND SOURCE TYPE PLOTS FOR DOUBLE-COUPLE EARTHQUAKES

In the previous chapter, I introduced the potency and the moment tensor as quantities that are proportional to the strain and the stress of the source process of an earthquake. In their general form potency and moment tensors have six independent parameters and can be expressed in terms of double-couple (four parameters), compensated linear vector dipole, and volumetric components. Among others, Hudson *et al.* [1989] and Vavryčuk [2005] showed approaches to decompose the moment tensor into these three components (see Chapter 2 and Appendix 3.5.1). Furthermore, they introduced tools to visualize these components, such as the classical Hudson-skewed-diamond plot [Hudson *et al.*, 1989] and the Vavryčuk source type plot [Vavryčuk, 2005].
However, source deformation is frequently dominated by the double-couple component (except for seismicity related to volcanic activity). As shown in Chapter 2, this dominance can be masked by the impact of elastic anisotropy of the source medium. If one corrects for this effect properly in the moment tensor as shown in Chapter 2, the resulting deformation, expressed by the potency tensor, is mainly double-couple. Thus, a further decomposition and analysis of the double-couple part of the moment tensor for a characterization of the faulting type or for stress field analysis is meaningful.
Lay & Wallace [1995] and Aki & Richards [2002] show that each DC-tensor can be written as a weighted summation of three or respectively four elementary tensors. These four elementary tensors describe (1) strike-slip faulting, (2) horizontal slip on a horizontal fault plane, (3) vertical slip on a vertical fault plane[1], and (4) dip-slip faulting on a fault dipping with 45°. They developed the mathematical basis, which I also use

[1]Here and in the following, I denote mechanisms of type (2) and (3) as "half-moon events". This term is frequently used in the microseismic community (see also discussion in section 5.1.1) and refers to the characteristic shape of the radiation pattern.

for this work. However, they did not show how to visualize these components properly. In this work, I decompose the moment tensor into four parts, which correspond to normal, thrust, half-moon and strike-slip faulting[1]. I visualize these components in a special form of a ternary diagram using a diamond, with the four end members at the edges of the diamond. Subsequently, I compare these source type plots to the existing standard visualization of Frohlich [1992].
Frohlich [1992, 2001] and Kagan [2007] show methods to distinguish different faulting geometries in a ternary diagram. They analyze P and T-axes instead of the moment tensor and introduced different projections into ternary diagrams with normal, thrust and strike-slip faulting as end members. One of the important advantages of this new approach, in comparison to the ternary diagrams of Frohlich [1992, 2001] and Kagan [2007], is that I have pure half-moon faulting as an additional end member. Half-moon events are frequently observed during hydraulic fracturing [Baig & Urbancic, 2010; Staněk & Eisner, 2013, 2017; Rutledge *et al.*, 2015, 2016; Grechka & Heigl, 2017; Grechka *et al.*, 2017; Boitz & Shapiro, 2018].
I will use this new decomposition to analyze seismicity induced by hydraulic fracturing in Horn-River Basin (see Chapter 4) and show that it is possible to delimit two types of source mechanisms from each other.

3.1 Decomposition of a Double-Couple Tensor

For the derivation here, I use the easiest possible type of a moment tensor, a pure double-couple or pure-slip source in a homogeneous isotropic medium. Such a tensor can be described by four independent parameters, the strike ϕ_s ([0, 2π]), the rake λ ([-π, π]), the dip of the fault plane δ ([0, $\pi/2$]) and the scalar seismic moment M_0:

$$M_0 = \mu A|s|, \tag{3.1}$$

where μ is the shear modulus, A is the area of the rupture surface and $|s|$ is the average slip length. The size of the earthquake is defined by the seismic moment, the orientation of the source is solely defined by strike, dip and rake[2] (see Figure 3.1). The moment

[1]Note that pure normal and thrust faulting in this decomposition only incorporates sources with a fault plane dipping with 45°.

[2]Note that the definition by strike, dip and rake is an alternative to the definition using **n** and **s** as shown in Chapter 2. In this sense, **M** would be defined as $M_{ij} = M_0(\hat{n}_i\hat{s}_i + \hat{n}_j\hat{s}_i)$, where $\hat{\mathbf{n}}$ and $\hat{\mathbf{s}}$ are the corresponding unit vectors of the quantities defined in Chapter 2.

tensor is then given by [Aki & Richards, 2002]:

$$M_{11} = -M_0 \left(sin(\delta)\, cos(\lambda)\, sin(2\phi_s) + sin(2\delta)\, sin(\lambda)\, sin(\phi_s)^2 \right) \tag{3.2}$$

$$M_{22} = M_0 \left(sin(\delta)\, cos(\lambda)\, sin(2\phi_s) - sin(2\delta)\, sin(\lambda)\, cos(\phi_s)^2 \right) \tag{3.3}$$

$$M_{33} = M_0\, sin(2\delta)\, sin(\lambda) \tag{3.4}$$

$$M_{23} = -M_0 \left(cos(\delta)\, cos(\lambda)\, sin(\phi_s) - cos(2\delta)\, sin(\lambda)\, cos(\phi_s) \right) \tag{3.5}$$

$$M_{13} = -M_0 \left(cos(\delta)\, cos(\lambda)\, cos(\phi_s) + cos(2\delta)\, sin(\lambda)\, sin(\phi_s) \right) \tag{3.6}$$

$$M_{12} = M_0 \left(sin(\delta)\, cos(\lambda)\, cos(2\phi_s) + \frac{1}{2} sin(2\delta)\, sin(\lambda)\, sin(2\phi_s) \right). \tag{3.7}$$

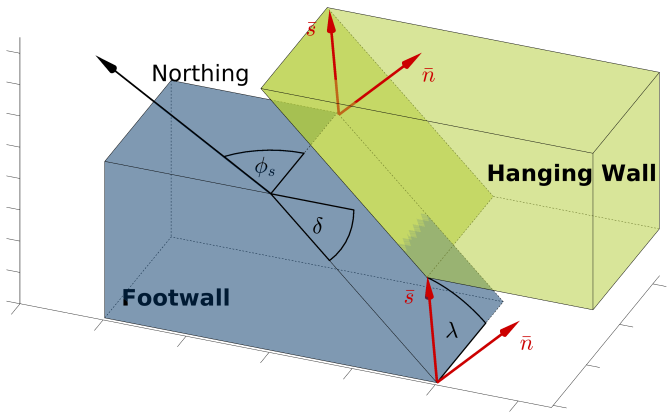

Figure 3.1: Sketch illustrating the definition of strike ϕ_s, dip δ and rake λ. Red vectors show the unit normal to the fault plane **n** and the slip-vector **s**, which can be defined using the three angles. The angle between **n** and **s** equals 90°.

For a given double-couple tensor one can determine strike, dip and rake angles as shown in Appendix A2. Note that each double-couple tensor can be described equally by two sets of strike, dip and rake angles that define faulting on the actual fault plane or faulting on the auxiliary plane that is normal to the fault plane. To distinguish different types of faulting, one could try to directly plot a diagram of these three angles, however, I show in Appendix A3 that such a plot is inconclusive and misleading.
Therefore, I express the DC tensor as the weighted summation of four elementary tensors [Aki & Richards, 2002; Lay & Wallace, 1995]:

$$\mathbf{M} = M_0 \left(a_1 * \mathbf{M}^{(1)} + a_2 * \mathbf{M}^{(2)} + a_3 * \mathbf{M}^{(3)} + a_4 * \mathbf{M}^{(4)} \right) \tag{3.8}$$

with coefficients a_i and elementary tensors $\boldsymbol{M}^{(i)}$ defined as:

$$a_1 = cos(\delta)cos(\lambda) \tag{3.9}$$

$$a_2 = sin(\delta)cos(\lambda) \tag{3.10}$$

$$a_3 = -cos(2\delta)sin(\lambda) \tag{3.11}$$

$$a_4 = sin(2\delta)sin(\lambda) \tag{3.12}$$

$$\mathbf{M}^{(1)} = \begin{pmatrix} 0 & 0 & -cos(\phi_s) \\ 0 & 0 & -sin(\phi_s) \\ -cos(\phi_s) & -sin(\phi_s) & 0 \end{pmatrix} \qquad \mathbf{M}^{(2)} = \begin{pmatrix} -sin(2\phi_s) & cos(2\phi_s) & 0 \\ cos(2\phi_s) & sin(2\phi_s) & 0 \\ 0 & 0 & 0 \end{pmatrix} \tag{3.13}$$

$$\mathbf{M}^{(3)} = \begin{pmatrix} 0 & 0 & sin(\phi_s) \\ 0 & 0 & -cos(\phi_s) \\ sin(\phi_s) & -cos(\phi_s) & 0 \end{pmatrix} \qquad \mathbf{M}^{(4)} = \begin{pmatrix} -sin(\phi_s)^2 & \frac{1}{2}sin(2\phi_s) & 0 \\ \frac{1}{2}sin(2\phi_s) & -cos(\phi_s)^2 & 0 \\ 0 & 0 & 1 \end{pmatrix}. \tag{3.14}$$

Note that $\mathbf{M}^{(2)}$ describes a pure strike-slip (SS) faulting (horizontal slip on a vertical fault plane, $\delta = \pi/2$ and $\lambda = 0$), $\mathbf{M}^{(4)}$ describes a faulting on an 45° inclined fault plane (IC) ($\delta = \pi/4$ and $\lambda = \pm\,\pi/2$), which corresponds to either normal or thrust faulting. $\mathbf{M}^{(1)}$ and a_1 describe upward or downward movement on a vertical fault plane, $\mathbf{M}^{(3)}$ and a_3 horizontal movement on a horizontal fault plane. Both mechanisms correspond to faulting that I previously introduced as half-moon events. The corresponding radiation patterns of these four mechanisms (for a strike of 0°) are shown in Figure 3.2.
The coefficients a_1 - a_4 then describe the fraction of each of the individual components in relation to the complete moment tensor $\mathbf{M}$. I use these coefficients to define three types (P_{IC}, P_{SS}, P_{HM}) of faulting:

$$P_{IC} = a_4 = (sin(2\delta)sin(\lambda)) \tag{3.15}$$

$$P_{SS} = |a_2| = |sin(\delta)cos(\lambda)| \tag{3.16}$$

$$P_{HM} = \sqrt{(a_1)^2 + (a_3)^2} = \sqrt{(cos(\delta)cos(\lambda))^2 + (-cos(2\delta)sin(\lambda))^2}. \tag{3.17}$$

P_{IC} denotes the part of inclined faulting (dip-slip faulting on a fault plane with 45° inclination), P_{SS} the part of strike-slip faulting and P_{HM} the part of half-moon faulting. Here, I define P_{SS} and P_{HM} to be always positive, because I do not want to distinguish between left and right lateral faulting. Both components, P_{SS} and P_{HM}, can then vary in the range of [0 1].

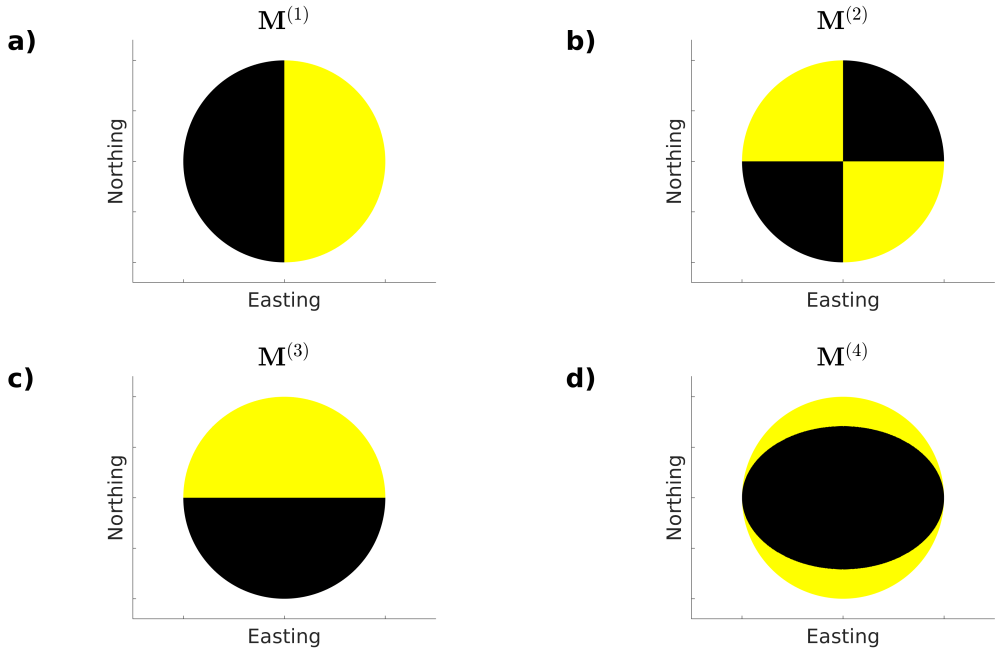

Figure 3.2: Radiation patterns of the four source mechanisms $\mathbf{M}^{(i)}$ (see also Table 3.1) for a strike angle of 0°.

P_{IC} can be additionally analyzed according to its sign: If a_4 is positive, the product a_4 * $\mathbf{M}^{(4)}$ describes thrust faulting, if a_4 is negative, the product describes a normal faulting geometry. The P_{IC} component can vary in the range of [-1 1].
Using Equations 3.9 - 3.12 one can show that these components additionally fulfill the following equation:

$$P_{IC}^2 + P_{SS}^2 + P_{HM}^2 = 1. \tag{3.18}$$

In other words, the three components define a unit vector in the three-dimensional space with components P_{IC}, P_{HM} and P_{SS}. In the following, I investigate how to project this vector into a 2D plane.

3.2 Visualization of Double-Couple Tensors in a Diamond Plot

In principle several projections of this vector are possible. Here, I propose a classical ternary diagram. For this, I divide each component by the sum of the three components:

$$P'_{IC} = \frac{P_{IC}}{|P_{IC}| + P_{SS} + P_{DS}} \tag{3.19}$$

$$P'_{HM} = \frac{P_{DS}}{|P_{IC}| + P_{SS} + P_{HM}} \tag{3.20}$$

$$P'_{SS} = \frac{P_{SS}}{|P_{IC}| + P_{SS} + P_{HM}} \tag{3.21}$$

$$P'_{SS} + P'_{IC} + P'_{HM} = 1. \tag{3.22}$$

These components P'_{IC}, P'_{SS} and P'_{HM} can be used now to build a diamond plot showing the fraction of the individual mechanisms (Figure 3.3). Due to the normalization, I only need two individual components to plot a mechanism in the source type plot. In this diamond a pure normal faulting mechanism (strictly with the dip angle of 45°) will plot at the top of the diamond, a thrust faulting mechanism at the bottom, strike-slip and half-moon mechanisms at the left or respectively right corner of the diagram. The rake and dip angles for these four "end-member" mechanisms are given in Table 3.1. Note that the strike does not influence this plot.
I define the x- and y-position of a moment tensor in the ternary diagram by the following equations:

$$x_{TD} = P'_{HM} + cos\left(\frac{\pi}{3}\right) * P'_{IC} \tag{3.23}$$

$$y_{TD} = sin\left(\frac{\pi}{3}\right) * P'_{IC}. \tag{3.24}$$

	Half-moon I	Strike-slip	Half-moon II	Thrust faulting	Normal faulting
rake λ	[-π, π]	-π, 0, π	-(π/2), (π/2)	(π/2)	-(π/2)
dip δ	0	(π/2)	(π/2)	(π/4)	(π/4)

Table 3.1: Dip and rake angles for selected mechanisms in radians. Half-moon I denotes the mechanism with a horizontal fault plane and horizontal slip direction and half-moon II the mechanism with a vertical fault plane and slip in vertical direction. See also the corresponding radiation pattern in Figure 3.2.

3.2.1 Analyzing Mechanisms in the Diamond Plot

In the following, I analyze how different events plot in this diamond plot. For this, I compute 5000 randomly oriented double-couple moment tensors and decompose them as shown before (Figure 3.3a). The figure reveals that double-couple events cannot plot in a certain (blue shaded) area of the diagram. For example, an event cannot have a percentage of 50% strike-slip and 50% normal faulting, it will always have a certain half-moon component.
To understand this observation, I analyze events that lie at the axes of the diamond plot. For instance, one can gradually change the mechanism from strike-slip to half-moon. For this, we either have to increase the rake from zero to 90° (half-moon II) or decrease the dip from 90° to zero (half-moon I). In both cases, the coefficient a_4 is zero (Equation 3.12). The mechanism has no inclined faulting component.

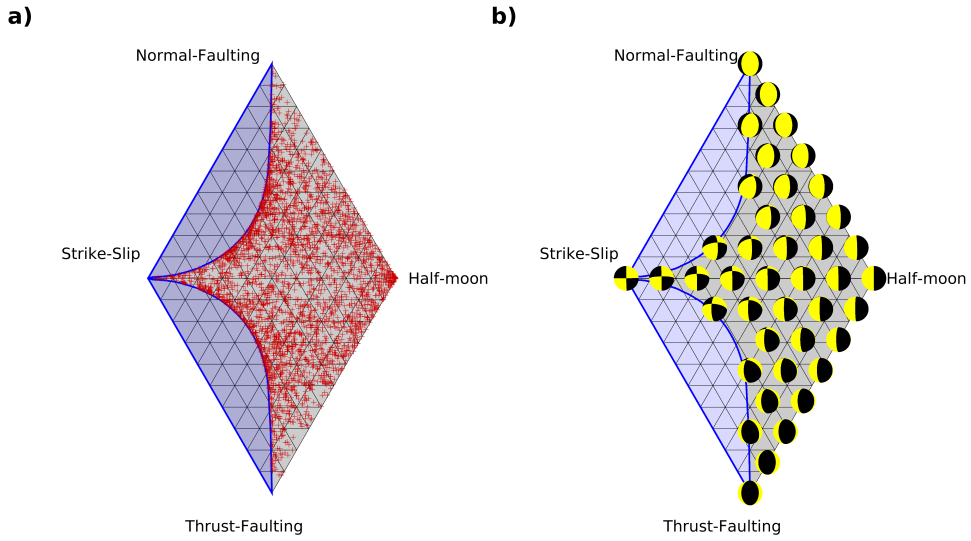

Figure 3.3: **a)** Decomposition of 5000 randomly orientated pure DC sources. No pure DC mechanism can plot in the blue shaded area, **b)** Position of the shown radiation patterns in the diamond plot. Radiation patterns are plotted for a strike of 0°.

Similarly, one can gradually change the mechanism from half-moon to inclined faulting. For this, one can decrease the dip from 90° to 45° while having a constant rake of ±90°. In this case, the coefficient a_2 is zero (see Equation 3.9). It has no strike-slip component and the considered mechanisms plot along the edge of the diamond along the axis from half-moon to normal faulting or respectively thrust faulting.
A direct path from strike-slip to normal or thrust faulting along the left edge of the diamond does not exist. For example, to change the mechanism from strike-slip to normal

faulting one has to decrease the rake from zero to -90° and the dip from 90° to 45°. In this case the coefficients a_1 and a_3 (Equations 3.9 and 3.11) are not equal to zero and these mechanisms contain certain half-moon components. The blue shaded area then marks the area, in which no pure DC source can plot in the diamond plot.
For a better illustration, I plot in Figure 3.3b the position of such moment tensors and additionally show the corresponding radiation pattern. As an example, let us consider the radiation pattern in the middle of the upper left part of the diamond: the beachball, as well as the decomposition, show that this moment tensor has a half-moon component of approximately 25%. This is because the fault plane has still a high inclination angle and the slip direction has already a certain component in the upward direction.

3.2.2 Comparison with Existing Source Type Plots

Among others, Frohlich [1992, 2001] and Kagan [2007] introduced different types of plots to visualize the diversity of double-couple focal mechanisms. In the following, I investigate the differences to this new source type plot.
Both authors work with the dip of the pressure (P), null (N) and tension (T) axes (δP, δN and δT). The direction of pressure, null and tension vectors are given by the eigenvectors of the moment tensor [Jost & Herrmann, 1989] (see also Appendix A2). In their decomposition, an individual mechanism is defined by three angles and the authors show different methods to project the 3D data to a 2D surface. Similarly, I describe the orientation of an earthquake by three components describing fractions of inclined P_{IC}, half-moon P_{HM} and strike-slip P_{SS} faulting.
To compare the standard [Frohlich, 1992] approach to my new decomposition, I plot the positions of selected mechanism types in my plot and in the Frohlich [1992] type plot in Figure 3.4. We observe several differences: the mechanisms which are distributed regularly in our plot are not regularly distributed in the Frohlich [1992] plot, which can be easily explained by the different projections. Especially in the domain of half-moon events of the Frohlich [1992] plot, the distribution of mechanisms is more dense. Furthermore, no empty areas in the Frohlich [1992] plot are visible, however, the probability of mechanisms at the edge between normal and strike-slip faulting seems to be very low (low point density at this edge in Figure 3.4). The fact that mechanisms cannot plot in a certain area in our new plot might be seen as a problem. However, it shows the important fact that any mechanism between strike-slip and normal or respectively thrust faulting contains some half-moon components, which is hidden in the ternary diagram of Frohlich [1992].

Additionally to the already discussed differences, I consider the following properties of the new decomposition as an advantage:

1. Because the components proposed in this work additionally fulfill Equation 3.18, I can describe the orientation of an arbitrary double-couple moment tensor by only two parameters.
2. With the projection described in section 3.2, I can make a quantitative statement for a moment tensor, e.g. 'the mechanism contains 70% half-moon, 20% normal and 10% strike-slip faulting'.
3. The difference between two mechanisms corresponds to a fixed difference in the diamond, which is not influenced by the projection. This makes it easy to define a metric to measure the difference between two moment tensors.
4. Potentially, the components P'_{IC}, P'_{HM} and P'_{SS} themselves are more capable and easier interpretable than the angles used by Frohlich [1992].

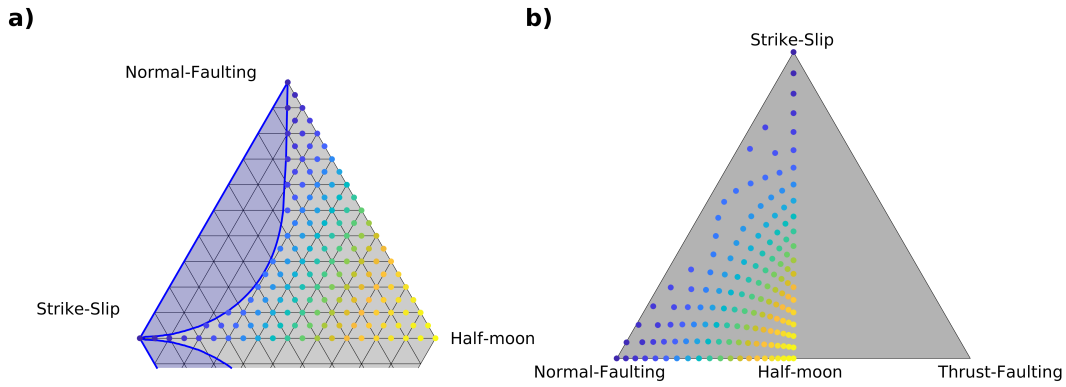

Figure 3.4: **a)** Diamond plot with selected uniformly distributed mechanisms. Note, that I only show the upper part of the diamond. **b)** Position of the same mechanisms in the Frohlich [1992] plot. Because of the projection, the mechanisms are not uniformly distributed in this plot.

3.3 Application of the Decomposition to Fracturing-Induced Seismicity in Horn-River Basin

The purpose of this work is to develop a method and a visualization that can be easily used to analyze the diversity of many source mechanisms of a dataset at the same time. Potentially, it can be used to delimit different types of faulting within a given dataset that can be then interpreted in terms of natural, triggered and induced seismicity.
Here, I use the new method to analyze microseismic events observed during hydraulic fracturing in Horn-River Basin, British Columbia, Canada. Natural faulting in this region is reported to be mainly strike-slip [Heidbach *et al.*, 2016]. The dataset and the procedure of moment tensor inversion will be described in detail in Chapter 4. Nonetheless, I consider the results of the source mechanism inversion already in this section, as it shows a practical application of the here proposed new moment tensor decomposition. Figure 3.5 shows the source type plot of the inverted events from Horn-River Basin in the diamond plot. A majority of events have high half-moon components above 60% (blue crosses in Figure 3.5a). An example of a representative radiation pattern from this group is shown in Figure 3.5b. Another group of events exhibits predominately strike-slip faulting and only small portions of half-moon, normal and thrust faulting (red stars in Figure 3.5a). A representative radiation pattern for this group is shown in Figure 3.5c.
The new source type plot was successfully used to delimit two types of mechanisms that cluster in two different regions of the diamond. The first group can be interpreted as hydraulic fracturing induced events, the second group containing much less events might be interpreted as triggered events along natural fractures. The geomechanical stress conditions for these event types and a further interpretation can be found in Chapters 4 - 6.

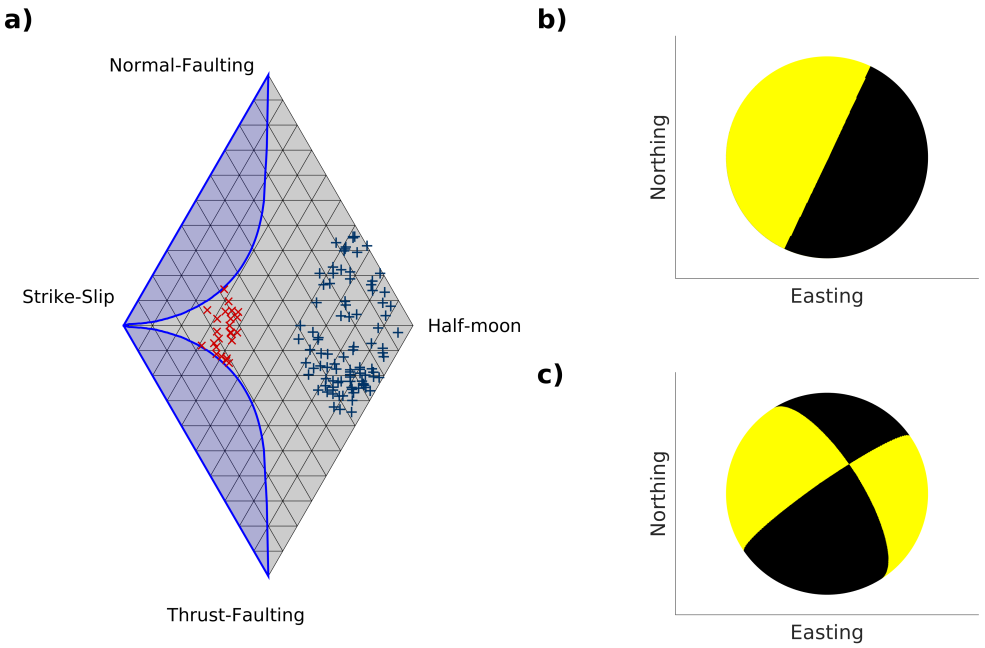

Figure 3.5: **a)** Ternary diamond plot of the inverted events from Horn-River Basin. The mechanisms can be grouped into two different groups with nearly pure half-moon faulting (blue crosses) and predominantly strike-slip faulting (red stars). Example radiation patterns for the two event types are shown in **b)** and **c)**.

3.4 Summary of Decomposition and Source Type Plots for Double-Couple Earthquakes

A general moment tensor can be decomposed into its volumetric, CLVD and double-couple components. However, the DC parts are dominant for most mechanisms. Therefore, I further decompose the DC parts according to their faulting geometry. For this, I split the DC parts into their strike-slip, half-moon, normal and thrust faulting components. The presented decomposition allows describing the faulting type by only two parameters, x_{TD} and y_{TD}. To visualize these components properly, I suggest a diamond plot. Mechanisms at the corners of the diamond plot correspond to (1) strike-slip, (2) half-moon and (3) normal and (4) thrust faulting on a strictly 45° inclined fault plane. In comparison to existing source type plots, the new proposed visualization shows no distortion caused by a projection. Furthermore, moment tensors can be considered in a quantitative sense, and an easy metric to analyze the diversity of mechanisms can be defined.

Generally, source type plots offer the opportunity to visualize the similarity or diversity of many source mechanisms at the same time. Especially in the microseismic industry,

these plots have not been popular up to now. Here, mostly beachballs or disks [Chapman & Leaney, 2012] of seismic event clouds are plotted to analyze source mechanisms. This frequently creates, particularly for a high amount of mechanisms, crowded images that are not easy to interpret. A possible reason for the rare usage of source type plots in the microseismic industry might be that mechanisms frequently show half-moon faulting. In previous source type plots, this type of faulting does not cluster in a single corner of the source type plot, but along an edge of the ternary diagram. As the proposed diamond has half-moon faulting as an end member, the new decomposition is, besides its use for global tectonic seismicity, particularly convenient to analyze hydraulic fracturing induced seismicity and has the potential to increase the usage of source type plots in the microseismic community.
In the final part, I show exactly such an application of the decomposition and visualization to hydraulic fracturing data from the Horn-River Basin. Using the decomposition, I can delimit two types of mechanisms that cluster in two different regions of the diamond plot. One group of events shows predominately half-moon faulting, the other group predominately strike-slip faulting. These groups can be interpreted as fluid-induced events (group one) and triggered events along natural faults (group two) (see also discussion in Chapters 4-6).

3.5 Appendixes for Chapter 3

In the following appendixes, I show (1) how to decompose an arbitrary moment tensor into its DC, CLVD and ISO components, (2) how to determine strike, dip and rake of a DC moment tensor and (3) why a simple dip vs rake plot is not convenient to distinguish different faulting geometries. Because these techniques are directly and solely related to the content of this chapter, the appendixes are placed subsequently to this chapter.

3.5.1 A1 - Decomposition of a non Double-Couple Tensor

In general, a seismic moment or potency tensor is not purely double-couple, but can also consist of isotropic (ISO) and compensated linear vector dipole (CLVD) components. The following derivations mainly follows [Vavryčuk, 2005; Lay & Wallace, 1995]. A general moment tensor can be written as:

$$\mathbf{M} = \mathbf{M}^{ISO} + \mathbf{M}^{CLVD} + \mathbf{M}^{DC}, \tag{3.25}$$

where the isotropic part of the moment tensor is given by

$$\mathbf{M}^{ISO} = \frac{1}{3} Trace(\mathbf{M}) \begin{bmatrix} 1 & 0 & 0 \\ 0 & 1 & 0 \\ 0 & 0 & 1 \end{bmatrix}. \tag{3.26}$$

The deviatoric moment tensor $\mathbf{M}^*$ is defined as:

$$\mathbf{M}^* = \mathbf{M} - \mathbf{M}^{ISO} \tag{3.27}$$

$$\mathbf{M}^* = \mathbf{M}^{CLVD} + \mathbf{M}^{DC}. \tag{3.28}$$

The deviatoric moment tensor can be decomposed into its eigenvalues λ_1,λ_2 and λ_3 and eigenvectors ν_1,ν_2 and ν_3:

$$\mathbf{M}^* = [\nu_1, \nu_2, \nu_3] * \begin{bmatrix} \lambda_1 & 0 & 0 \\ 0 & \lambda_2 & 0 \\ 0 & 0 & \lambda_3 \end{bmatrix} * [\nu_1, \nu_2, \nu_3]^{-1}. \tag{3.29}$$

We can now define the diagonalized CLVD and DC components of the deviatoric moment tensor:

$$\mathbf{M}_{diag}^{CLVD} = |\epsilon|\lambda_{|max|}\begin{bmatrix}-1 & 0 & 0\\ 0 & -1 & 0\\ 0 & 0 & 2\end{bmatrix} \tag{3.30}$$

$$\mathbf{M}_{diag}^{DC} = (1-2|\epsilon|)\lambda_{|max|}\begin{bmatrix}-1 & 0 & 0\\ 0 & 0 & 0\\ 0 & 0 & 1\end{bmatrix}, \tag{3.31}$$

where $\lambda_{|max|}$ and $\lambda_{|min|}$ denote the eigenvalues with the largest and respectively the smallest absolute value and ϵ is defined as

$$\epsilon = -\frac{\lambda_{|min|}}{|\lambda_{|max|}|}. \tag{3.32}$$

The non-diagonalized parts of the tensor are then given by

$$\mathbf{M}^{CLVD} = [\boldsymbol{\nu}_1, \boldsymbol{\nu}_2, \boldsymbol{\nu}_3] * \mathbf{M}_{diag}^{CLVD} * [\boldsymbol{\nu}_1, \boldsymbol{\nu}_2, \boldsymbol{\nu}_3]^{-1} \tag{3.33}$$

$$\mathbf{M}^{DC} = [\boldsymbol{\nu}_1, \boldsymbol{\nu}_2, \boldsymbol{\nu}_3] * \mathbf{M}_{diag}^{DC} * [\boldsymbol{\nu}_1, \boldsymbol{\nu}_2, \boldsymbol{\nu}_3]^{-1}. \tag{3.34}$$

Using this decomposition of an arbitrary tensor one can delimit the DC components from the CLVD and ISO components and decompose only the DC components into their half-moon, normal/thrust and strike-slip faulting components.

3.5.2 A2 - Determination of Strike, Dip and Rake of a DC Moment Tensor

Here, I briefly review how to obtain the strike, dip and rake angles from a DC moment tensor. As the result of a moment tensor inversion, we typically obtain a full moment tensor, however, for the approach described in this chapter, we need the strike, dip and rake angles of this moment tensor. If the moment tensor is not DC, it can be decomposed into its CLVD, ISO and DC part as shown in Appendix A1. The derivation shown here mainly follows the work of Jost & Herrmann [1989].
A normalized double-couple moment tensor $\mathbf{M}$ can be decomposed into its eigenvectors ν_i and eigenvalues λ_i. In the case of a normalized DC source, the eigenvalues are the following:

$$\lambda_1 = 1 \qquad \lambda_2 = -1 \qquad \lambda_3 = 0. \tag{3.35}$$

The corresponding eigenvectors $\boldsymbol{\nu}_1$, $\boldsymbol{\nu}_2$ and $\boldsymbol{\nu}_3$ then denote the pressure, tension, and null axis of the moment tensor. Using the pressure and tension axes, we can obtain the

normal of the fault plane **n** and the normalized slip direction $\bar{\mathbf{s}}$ on this fault plane:

$$\mathbf{n} = \frac{1}{\sqrt{2}}(\boldsymbol{\nu}_2 - \boldsymbol{\nu}_1) \tag{3.36}$$

$$\mathbf{s} = \frac{1}{\sqrt{2}}(\boldsymbol{\nu}_2 + \boldsymbol{\nu}_1)\,. \tag{3.37}$$

The other nodal plane is then defined by:

$$\mathbf{n} = \frac{1}{\sqrt{2}}(\boldsymbol{\nu}_2 + \boldsymbol{\nu}_1) \tag{3.38}$$

$$\mathbf{s} = \frac{1}{\sqrt{2}}(\boldsymbol{\nu}_2 - \boldsymbol{\nu}_1)\,. \tag{3.39}$$

The normal and slip vectors are defined as [Aki & Richards, 2002]:

$$\mathbf{n} = \begin{pmatrix} -sin(\delta)sin(\phi_s) \\ sin(\delta)cos(\phi_s) \\ -cos(\delta) \end{pmatrix} \tag{3.40}$$

$$\mathbf{s} = \begin{pmatrix} cos(\lambda)cos(\phi_s) + cos(\delta)sin(\lambda)sin(\phi_s) \\ cos(\lambda)sin(\phi_s) - cos(\delta)sin(\lambda)cos(\phi_s) \\ -sin(\lambda)sin(\delta) \end{pmatrix}. \tag{3.41}$$

Using the six equations (3.40) and (3.41) one can obtain strike ϕ_s, dip δ and rake λ.

3.5.3 A3 - Why not Just a Dip vs Rake Plot ?

At first sight, the moment tensor decomposition presented in this chapter seems to be unnecessary and cumbersome. The strike of the fault plane does not play any role if we want to distinguish different faulting geometries, as it only describes a horizontal rotation. Therefore it should be possible to plot the dip of an earthquake as a function of the rake (Figure 3.6).
In such a plot, normal and thrust faulting mechanisms are explicitly defined, see the blue and red diamonds in Figure 3.6.
A pure strike-slip faulting appears three times in this plot. For λ equal to zero it describes a right lateral, for λ equal to $-\pi$ or π a left lateral strike-slip faulting (blue squares in Figure 3.6).
Half-moon mechanisms are either defined by vertical fault planes ($\delta = \pi/2$) and a rake of $-\pi/2$ or $\pi/2$, respectively, or by a horizontal fault plane ($\delta = 0$) and an arbitrary rake $\lambda = [-\pi, \pi]$.

This shows that in such type of plot no distinct classification to one of the end-members (normal, thrust, strike-slip and half-moon faulting) is possible. This explains the necessity of the decomposition shown in this chapter.

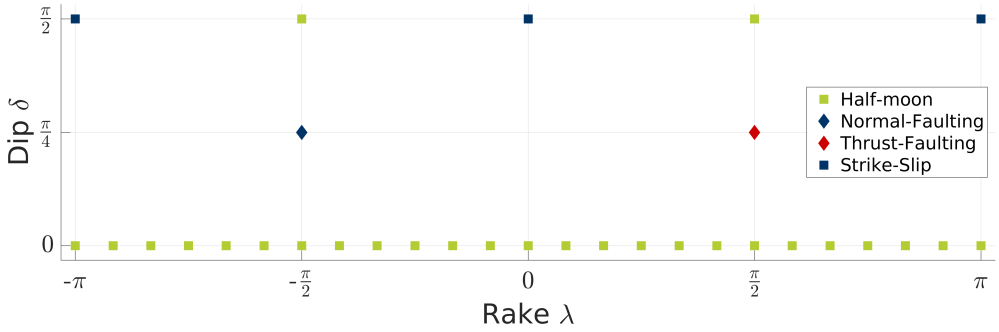

Figure 3.6: Dip as a function of rake for selected types of faulting. Blue and red diamonds denote normal or respectively thrust faulting, blue squares strike-slip and green squares half-moon faulting.

CHAPTER 4

ANISOTROPIC MOMENT TENSOR INVERSION OF HYDRAULIC FRACTURING-INDUCED SEISMICITY

In the following, I use the two theoretical concepts developed in Chapters 2 and 3 to invert and analyze source mechanisms of microseismic events induced by hydraulic fracturing. For this, I present a workflow that can be used to invert for pure-slip potency tensors and non-DC moment tensors and that takes source and propagation anisotropy into account. Using this approach, I invert mechanisms for 132 events and analyze (1) the spatial distribution, (2) the non-DC components created by anisotropy and (3) diversity of mechanisms. Additionally, I discuss the question if the incorporation of anisotropy provides better MTI results than a pure isotropic inversion. To analyze the event distribution and propagation of the hydraulic fracture, I moreover introduce the principle of spatio-temporal gyration and apply this concept to the data. In the final part of this chapter, I summarize the main observations of this case study that I then try to explain and reproduce with numerical modeling in Chapters 5 and 6.

4.1 Introduction to the Data Set

The data set consists of three stages of hydraulic fracturing recorded in August 2010 by two down-hole 3-component (3C) receiver arrays. The data were provided by a sponsor of the *PHASE* research consortium.
In a previous work, Reshetnikov & Shapiro [2015] inverted travel times of three perforation shots to obtain an anisotropic (VTI) velocity model. The depth distributions of vertical P and S-wave velocities are shown in Figure 4.1. Especially in the upper part, the velocity model exhibits high degrees of anisotropy, whereas the anisotropy in

the source depth (between 1750 m and 1820 m) is rather small. Additionally, Reshetnikov & Shapiro [2015] hand-picked arrival times of P and S-wave arrivals and inverted for earthquake hypocenters for all three stages using travel times and polarizations of P-waves. To compute travel times and raypaths, raytracing described in Reshetnikov [2014] was used. Hypocenter locations for the complete third stage are shown in Figure 4.2. The hypocenters form a thin strip that is oriented approximately south-west to north-east that coincides with the orientation of the maximal principal stress (σ_H) [Heidbach *et al.*, 2016]. The depth distribution (Figures 4.2b and 4.2c) shows that events are not homogeneously distributed, but occur in narrow depth bands, especially those that are close to the injection point (red circle in Figure 4.2).
For the following moment tensor inversion, I use all information (arrival time picks, velocity model and locations) from Reshetnikov & Shapiro [2015] and determine source mechanisms for a subset of events[1].

4.2 Moment Tensor Inversion (MTI) in Anisotropic Media

4.2.1 General Assumptions for the Inversion

Full or Constraint MTI ?
The moment tensor **M** generally consists of six independent components. Using inverse theory, it is possible to rewrite Equation 2.24 to

$$\mathbf{M} = (\mathbf{G}^T\mathbf{G})^{-1}\mathbf{G}\mathbf{u} \tag{4.1}$$

and invert the full moment tensor using 3C displacement **u** and the known Green's tensor **G**.
Nolen-Hoeksema & Ruff [2001] show that if raypaths and the corresponding slowness vectors are limited to a single plane, an unambiguous determination of all six components of the moment tensor is impossible. On the other hand, Grechka [2014] shows that is theoretically possible to invert the full moment tensor in anisotropic media using a single straight borehole. The sensitivity of each independent component of **M** is controlled by the source-receiver geometry and thereby a function of the Green's tensor **G**. Although, an inversion of the full moment tensor is theoretically possible for the given source-receiver geometry, a sensitivity analysis showed that the geometry is rather insensitive to ISO and CLVD-components. This means that small errors in **G**, as well as noise in data **u**, might propagate into **M** [Grechka, 2020b] and can create unrealistically high ISO and CLVD-components.

[1] I use events that occur early during the treatment and have a sufficient signal-to-noise ratio.

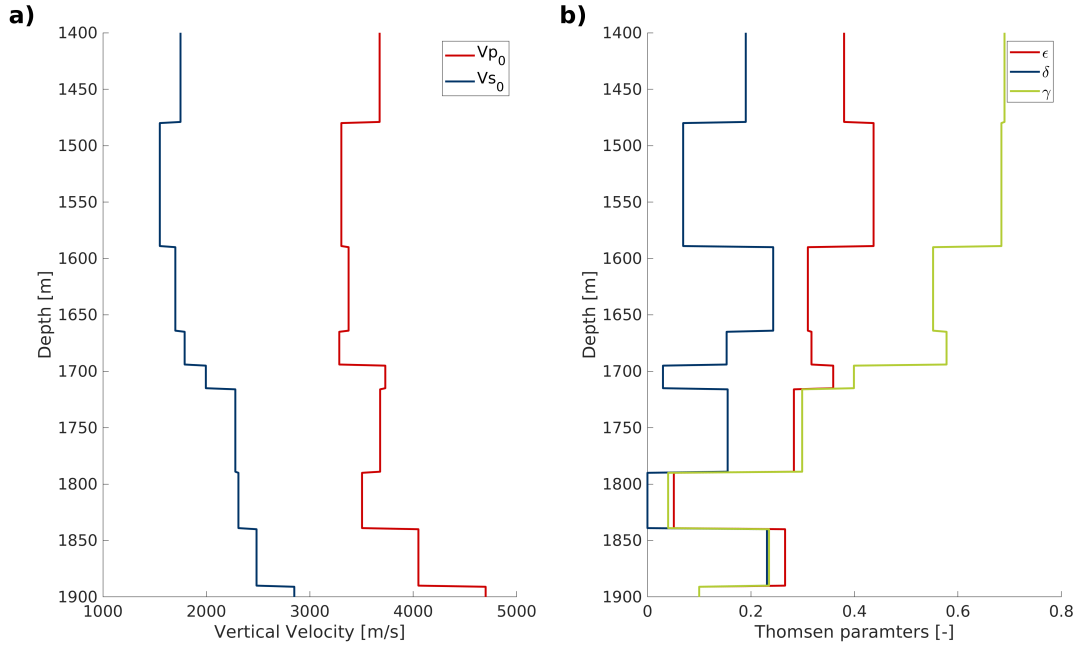

Figure 4.1: Velocity model from Reshetnikov & Shapiro [2015]. **a)** Depth distribution of vertical P and S-wave velocities, **b)** Thomsen paramters of the VTI-medium.

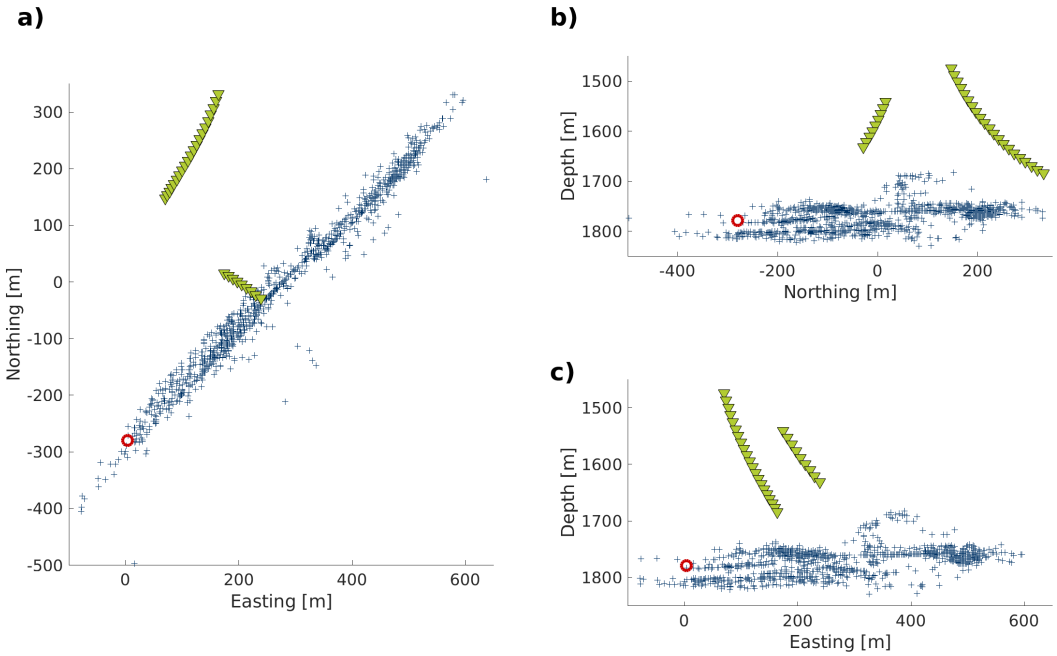

Figure 4.2: Hypocenter locations of the third fracturing stage from Reshetnikov & Shapiro [2015], **a)** map view, **b)** & **c)** side view. The red circle marks the location of the injection point, the green triangles the positions of the downhole geophones.

Thus, I decided to use a moment tensor inversion constrained to less than six unknowns. Typical constrained MTI's either assume a tensile source that is fully described by five independent parameters or a double-couple MT that consists of four independent components (seismic moment M_0, strike Φ_S, dip θ and rake λ) [Grechka, 2020b]. Although the creation and propagation of the hydraulic fracture itself are best described by tensile opening, I assume that the microseismic events that I consider in the following occur behind the wall of the hydraulic fracture and do not show significant tensile opening. Additionally, I scale the observed displacement to get rid of the scalar seismic moment as an additional inversion parameter. Thus, I use a constrained inversion scheme that only determines three unknowns (strike, dip and rake).

DC Potency Tensor - non-DC Moment Tensor

As discussed above, I constrain the inversion to pure slip faulting (which would correspond to DC faulting in isotropic media). Because the pure shear faulting occurs in anisotropic rock layers, the corresponding moment tensors are generally not purely double-couple (see theoretical considerations in Chapter 2). More precisely, the inversion scheme I present in the following determines pure slip potency tensors, i.e. I rather perform a constrained potency tensor inversion than a MTI. Although the resulting moment tensors are non-DC, the degree of freedom I invert for is still three (Φ_S, θ and λ).

4.2.2 Data Pre-Processing

Receiver Rotation

The monitoring system contains 30 3-component seismometers that are deployed in two inclined boreholes. The orientation of the three components of each seismometer is unknown and differs from receiver to receiver. Because the polarity of P-wave is needed for the moment tensor inversion, I firstly rotate the waveforms to an east-north-vertical (x,y,z) coordinate system. An explanation of this procedure can be for instance found in Grechka [2020a]. Here, I compute raypaths and theoretical polarizations at each receiver for one of the perforation shots. For this, a two-point raytracing algorithm described in Röser *et al.* [2018] and Röser & Shapiro [2019] is used.
Subsequently, I rotate the recorded waveforms of this perforation shot such that they best fit the expected polarizations from raytracing. This is exemplarily shown in Figure 4.3. After rotation, neighboring traces have a significantly higher waveform similarity. Since a perforation shot can be considered as an explosion, all P-wave first motions are consistently positive.

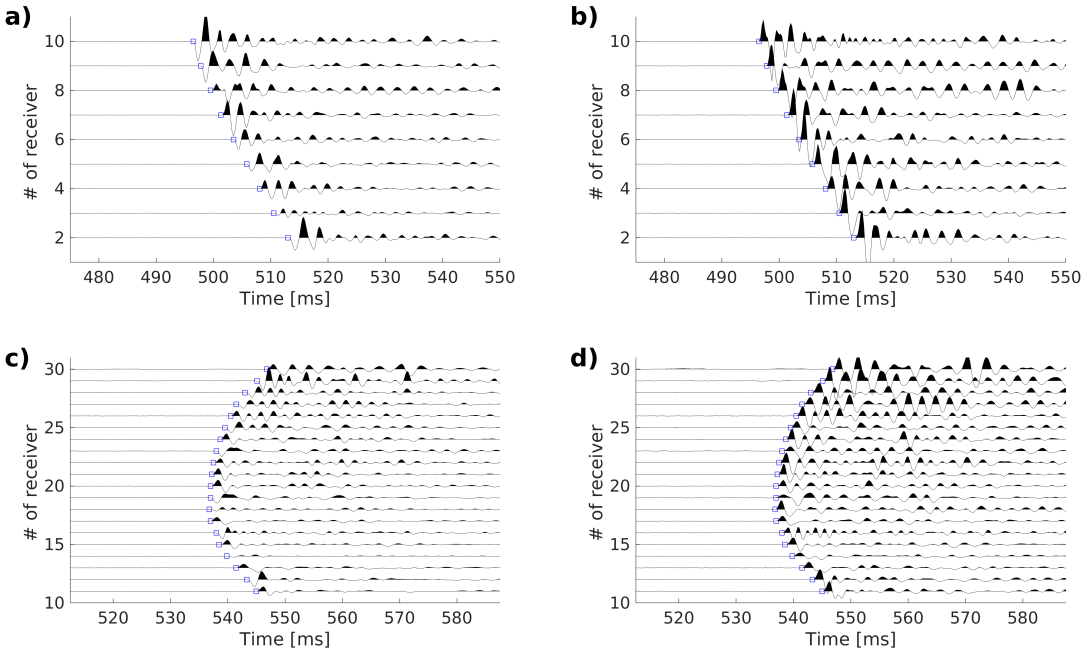

Figure 4.3: Seismograms of a perforation shot recorded at the two receiver arrays (upper and lower part of the Figure) and corresponding P-onset time picks. Figures **a)** and **c)** show the seismograms of the 3rd component, **b)** and **d)** the vertical (z-) component after the rotation. After the rotation, neighbored geophones have a significant higher waveform similarity.

Determination of Amplitude

To determine microseismic source mechanisms the P-wave polarity and amplitudes of P- and S-wave displacement are needed. The used downhole geophones record the ground velocity, and waveforms are therefore integrated to obtain displacement seismograms. I then use the handpicks to automatically determine the first-motion polarity of P-wave arrivals and a scalar displacement for both, P and S-wave, arrivals:

$$u^{Pmeas} = \frac{u(t_{pw})_z}{|u(t_{pw})_z|} max\left(\sqrt{u(t_{pw})_x^2 + u(t_{pw})_y^2 + u(t_{pw})_z^2}\right) \tag{4.2}$$

$$u^{Smeas} = max\left(\sqrt{u(t_{sw})_x^2 + u(t_{sw})_y^2 + u(t_{swq})_z^2}\right), \tag{4.3}$$

where t_{pw} and t_{sw} denote time windows of a length of half of the wavelength of P- and S-waves after the hand picked arrival time of the respective wavetypes [1]. In this notation,

[1]The considered microseismic events have quite simple waveforms and exhibit typically only a single peak for both, P and S-waves. Thus it is sufficient to use the short time windows t_{pw} and t_{sw}

u^{Smeas} is strictly positive, u^{Pmeas} can be both, positive and negative. For reasons of quality control, I also compute a S-P displacement ratio:

$$u^{s/p_{meas}} = log10\left(\frac{u^{Smeas}}{|u^{Pmeas}|}\right). \tag{4.4}$$

4.2.3 Inversion Procedure

An overview of the processing procedure is schematically shown in Figure 4.4 and explained in detail below.
For each event, I use the source depth determined by Reshetnikov & Shapiro [2015] and the corresponding elastic parameters of the source layer to compute the stiffness tensor **C** for the source depth (Equations 2.10 - 2.15).
Subsequently, I use a two-point raytracing algorithm of Röser *et al.* [2018] to compute raypaths from the source to each of the 30 receivers. From raytracing, I obtain polarizations, slowness and length of the raypath to compute the Green's tensor **G** (see Equation 2.24). The Green's tensor expressed in contracted notation consists of (Nx3,6) elements for each wavetype, where N denotes the number of receivers. Both stiffness of the source region and raypaths are independent of the type of faulting and have to be computed only once for each event.
Next, I run a grid search over all possible strike, dip and rake values. For all possible combinations of strike, dip and rake, I compute the corresponding potency tensor (see corresponding Equations 3.2 - 3.7 in Chapter 3). Then, I compute a normalized moment tensor (see Equation 2.20) using the source stiffness (see above), the potency tensor and a fixed rupture area A. Finally, I compute a synthetic 3C displacement:

$$u_I^{syn} = G_{IJ}M_J. \tag{4.5}$$

The synthetic 3C displacement is then converted into a scalar displacement (compare also Equations 4.2 - 4.4):

$$u^{P_{syn}} = \frac{u_z^{P_{syn}}}{\left|u_z^{P_{syn}}\right|}\sqrt{\left(u_x^{P_{syn}}\right)^2 + \left(u_y^{P_{syn}}\right)^2 + \left(u_z^{P_{syn}}\right)^2} \tag{4.6}$$

$$u^{S_{syn}} = \sqrt{\left(u_x^{S_{syn}}\right)^2 + \left(u_y^{S_{syn}}\right)^2 + \left(u_z^{S_{syn}}\right)^2} \tag{4.7}$$

for each receiver. Because I do not want to invert for the scalar seismic moment, I rescale both synthetic and measured amplitudes by dividing them by the mean of the corresponding P and S-wave amplitudes:

$$\bar{u}^{P_{syn}} = \frac{u^{P_{syn}}}{mean(u^{P_{syn}}, u^{S_{syn}})} \qquad \bar{u}^{S_{syn}} = \frac{u^{S_{syn}}}{mean(u^{P_{syn}}, u^{S_{syn}})} \tag{4.8}$$

$$\bar{u}^{P_{meas}} = \frac{u^{P_{meas}}}{mean(u^{P_{meas}}, u^{S_{meas}})} \qquad \bar{u}^{S_{meas}} = \frac{u^{S_{meas}}}{mean(u^{P_{meas}}, u^{S_{meas}})}. \tag{4.9}$$

Finally, I compute a misfit between the modeled (synthetic) scalar $\bar{u}^{syn}$ and the measured $\bar{u}^{meas}$ displacement:

$$\Delta u = \sum_{rec=1}^{N_{rec}} \left|\left|\bar{u}_{rec}^{P_{syn}}\right| - \left|\bar{u}_{rec}^{P_{meas}}\right|\right| * w_{rec}^{P} + \left|\bar{u}_{rec}^{S_{syn}} - \bar{u}_{rec}^{S_{meas}}\right| * w_{rec}^{S} + p_{rec}^{pol} * w_{rec}^{pol}, \tag{4.10}$$

where w_{rec} are weighting factors for each receiver and p_{pol} a factor that accounts for the correctness of P-wave polarity

$$p^{pol} = \frac{1}{2}\left|\frac{\bar{u}^{p_{syn}}}{|\bar{u}^{p_{syn}}|} - \frac{\bar{u}^{p_{meas}}}{|\bar{u}^{p_{meas}}|}\right|, \tag{4.11}$$

that is either zero, if synthetic and measured P-wave polarity coincide or otherwise one.

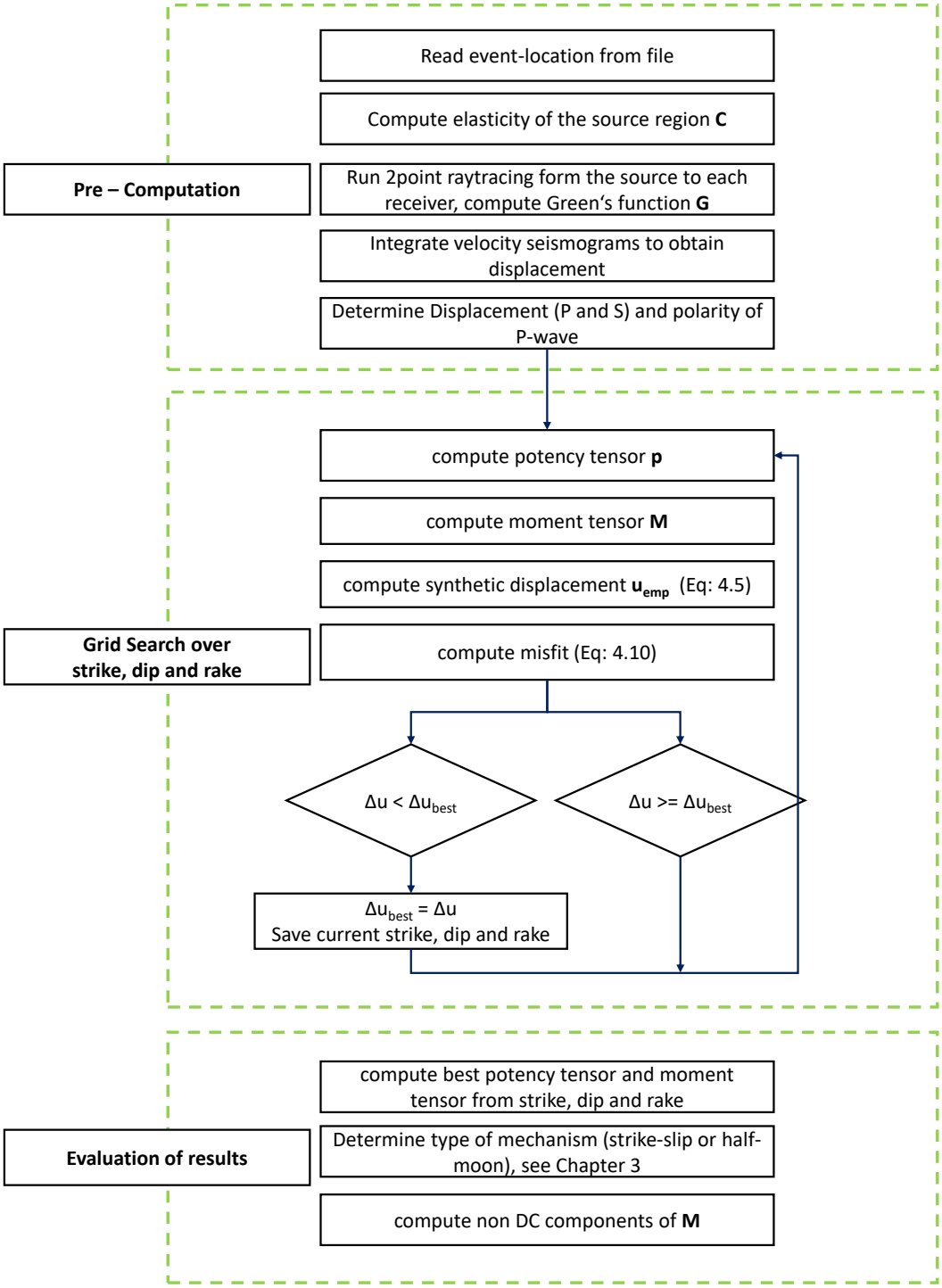

Figure 4.4: Used inversion scheme to determine moment tensors in anisotropic media.

4.3 Results of the Moment Tensor Inversion

4.3.1 Results for a Single Example Event

Figure 4.5 shows seismograms (vertical component) for the two monitoring arrays and the inverted mechanism of a single event that shows typical characteristics for this dataset. Figure 4.6 shows the measured and best fit amplitudes for all 30 receivers. For this particular event, we observe a change in P-wave polarity (from negative to positive polarity) between receivers seven and nine (Figure 4.5a). The P-wave amplitude at receiver 8 is small, the polarity ambiguous. Thus this receiver is expected to observe a point of the focal sphere that is close to one of the nodal planes. The inverted mechanism (Figure 4.5c) shows exactly this pattern. Note that in contrast to the typical lower hemisphere plot of the beachball, I here plot the upper hemisphere to better compare the radiation pattern with the recorded seismograms. In this example, the source-receiver geometry is (by chance) extremely useful, since the orientation of the nodal plane can be reconstructed with high accuracy. The second receiver array observes only points on the side of the radiation pattern that exhibits negative polarity (Figure 4.5b and 4.5c). Figure 4.6 shows that the measured amplitudes can be accurately fitted for both P and S-wave amplitudes. Solely, receivers 7 and 10-13 exhibit higher S-Wave amplitudes than expected. Figure 4.6c shows the logarithm of the S/P amplitude ratio as quality control. The fit is close to the data for most receivers and only differs significantly for receivers seven and eight. As discussed above, these receivers observe a point on the focal sphere that is close to the nodal plane, where P-wave amplitudes are extremely small. For these receivers and this particular event the signal-to-noise ratio for P-waves is extremely small and the measured amplitude is significantly contaminated by the noise. This leads to higher P-wave amplitudes and a smaller S/P ratio than theoretically expected. Figure 4.7 shows for comparison the radiation patterns of the moment tensor and of the PTI (see definition in Chapter 2). The moment tensor shows non-DC components (observable especially close to the nodal points) that are created by the anisotropy of the source layer, whereas the PTI is pure DC, which is a constraint of the inversion procedure. The mechanism shows mostly half-moon faulting.

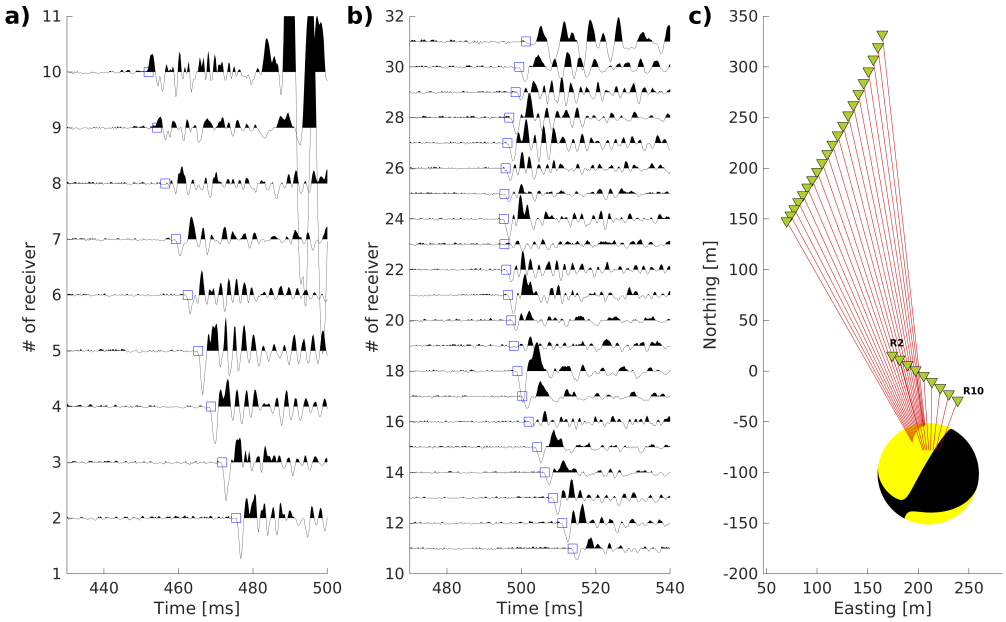

Figure 4.5: Seismograms of the z-component for **a)** the first array, and **b)** for the second array for an example event. **c)** shows the corresponding inverted mechanism and raypaths to all receivers. Note the polarity flip of P-wave between receivers seven and nine in **a** and the corresponding nodal plane in **c**.

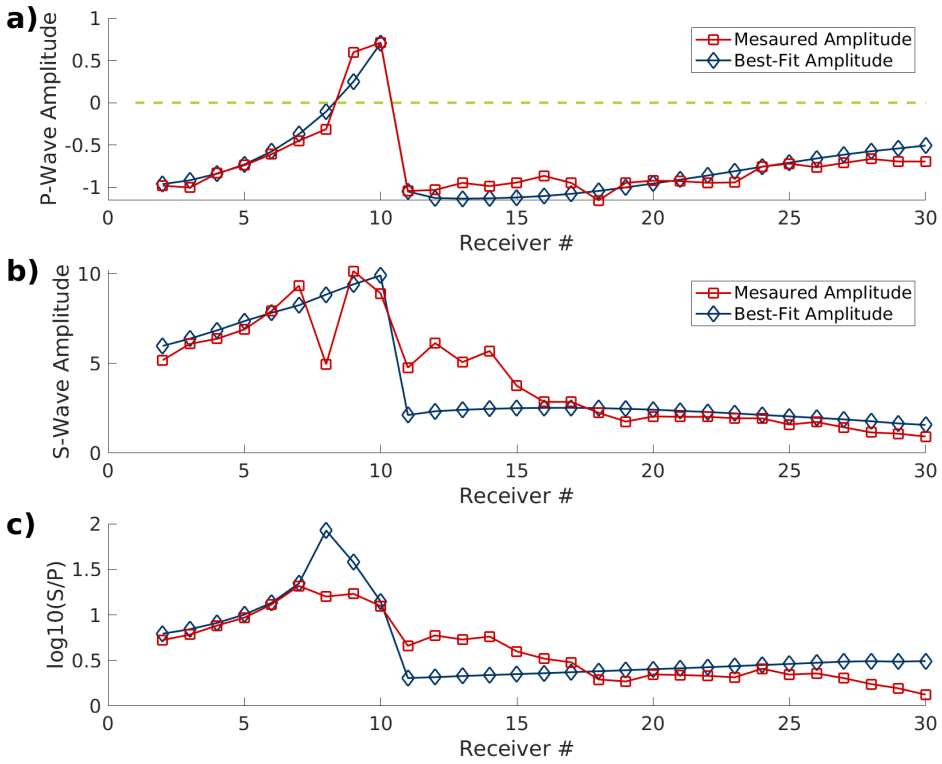

Figure 4.6: Measured and best fit amplitudes of **a)** P-wave, **b)** S-wave and **c)** S/P ratio for the example event shown in Figure 4.5.

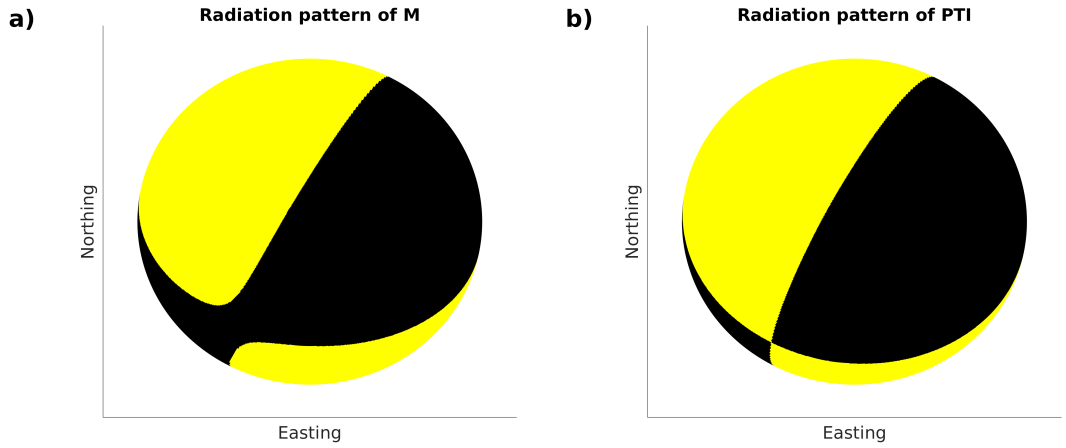

Figure 4.7: Radiation pattern of **a)** the moment tensor and **b)** of the PTI (see definition in Chapter 2). The moment tensor shows small non-DC components, whereas the PTI is pure double-couple (nodal planes intersect in a single line).

4.3.2 Results for all Events

Distribution of Mechanisms

Using the described algorithm, I inverted moment tensors for 132 events. The mechanisms and their spatial distribution are shown in Figure 4.8. The events occur in a thin strip oriented approximately south-west to north-east. This is in good agreement with the orientation of the maximum horizontal stress that has a similar orientation [Heidbach *et al.*, 2016]. The natural faulting regime in the area is strike-slip. The figure shows a majority of 106 half-moon events[1] (color-coded in yellow-black), a special type of dip-slip mechanism that is either characterized by horizontal slip on a horizontal fault plane or by upward or downward slip on a vertical fault plane. Beside these events, I inverted 26 strike-slip events (color-coded in blue-red) that are, as discussed above, typical for the natural seismicity in the region. Half-moon events that occur close to the injection point (red circle in Figure 4.8) show vertical fault (or auxiliary) planes that are parallel to the hydraulic fracture (i.e. oriented south-west to north-east). Half-moon events that occur at greater distances to the injection point exhibit fault planes that are rather oriented north to south.

Figure 4.9 shows the depth distribution of the inverted mechanisms. Because altogether only 26 strike-slip events were observed, the statistics are too poor to analyze, but events seem to be rather homogeneously distributed in depth. In contrast, half-moon events show a clear distribution with depth. The majority of events occur in depths between 1790-1800 m which is close to a layer interface (see velocity model in Figure 4.1). Another peak in the depth distribution is at 1760-1770 m. Between these

[1] I discuss the term half-moon event in detail in Chapter 5.

depths hardly any half-moon events are observed.
The depths distribution shows that events are limited to two rock layers that exhibit moderate anisotropy (layer between 1710-1790 m) and nearly no anisotropy (layer between 1790-1840 m), see Figure 4.1. In the following, I will analyze the non-DC components of the moment tensors created by this source anisotropy.

Analysis of Non-DC Components

Figure 4.10 shows the moment tensor decomposition of the inverted mechanisms for the shallow layer, Figure 4.11 the mechanisms for the deeper layer.
The events in the upper layer exhibit moderate non-DC components (CLVD components between -25 and 20% and volumetric components between -10 and 10%), events in the deeper layer non-DC components close to zero. Strike-slip events exhibit smaller non-DC components than half-moon events.
If we compare these results to the theoretical modeling from Chapter 2 (see Figure 2.9), we observe approximately what was theoretically expected: the non-DC components in the deeper layer are small for both half-moon and strike-slip because anisotropy in this source layer is nearly zero and the fault planes are close to vertical. The observed non-DC components for events in the upper layer are comparable to the ones of the theoretical modeling. The observed non-DC components are slightly higher than theoretically expected, which can be explained by a greater variability in the mechanism distribution. As expected from the theoretical modeling, non-DC components of half-moon events are larger than the strike-slip ones. Both theoretical modeling and data example show that the CLVD-components are approximately twice as high as the ISO-components, which is a characteristic of this particular anisotropic medium.

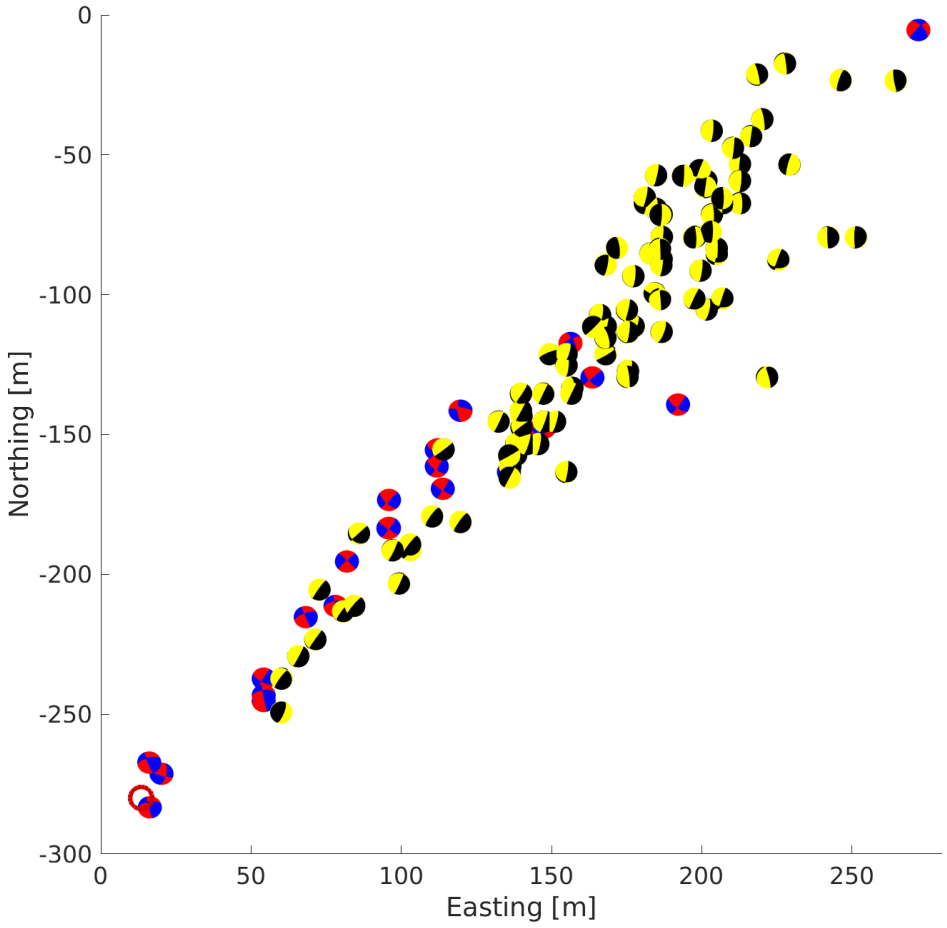

Figure 4.8: Radiation patterns of the inverted moment tensors, red/blue events show strike-slip faulting, yellow/black half-moon events.

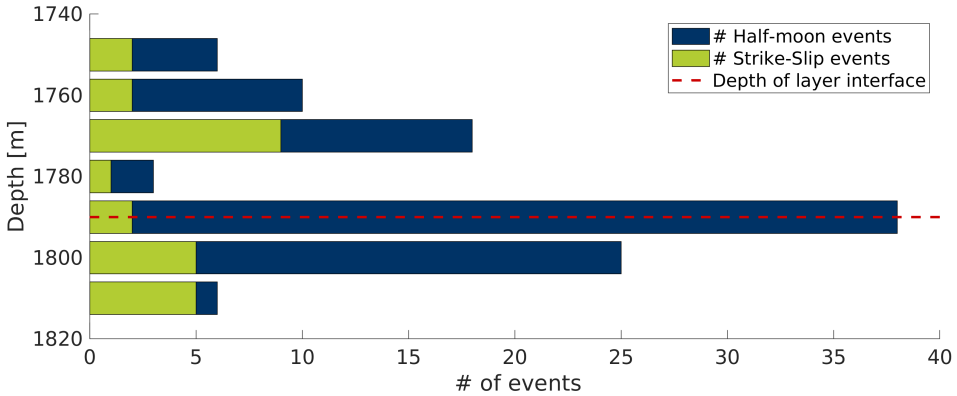

Figure 4.9: Depth distribution of the inverted mechanisms, the red line marks the interface between two layers, see Figure 4.1. The majority of events occurs close to the layer interface at 1790 m and at in depths of ≈ 1770 m.

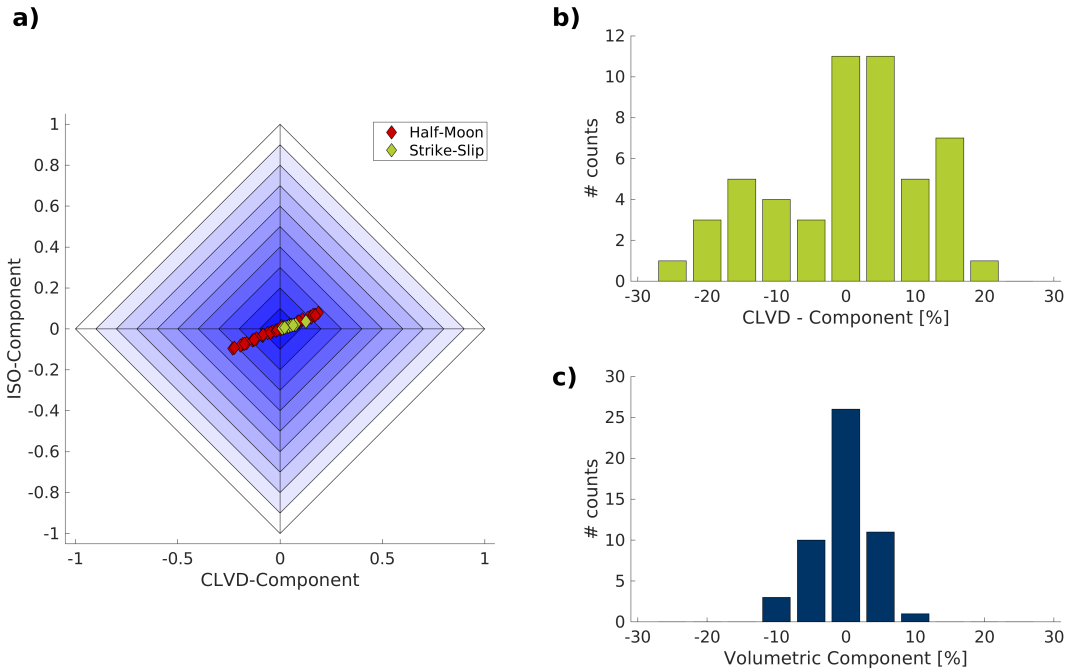

Figure 4.10: **a)** Vavrychuk diamond plot for the inverted mechanisms shown in Figure 4.8 that occur above the layer interface at 1790 m (see Figure 4.9), **b)** histogram of the CLVD-components, **c)** histogram of the ISO-components.

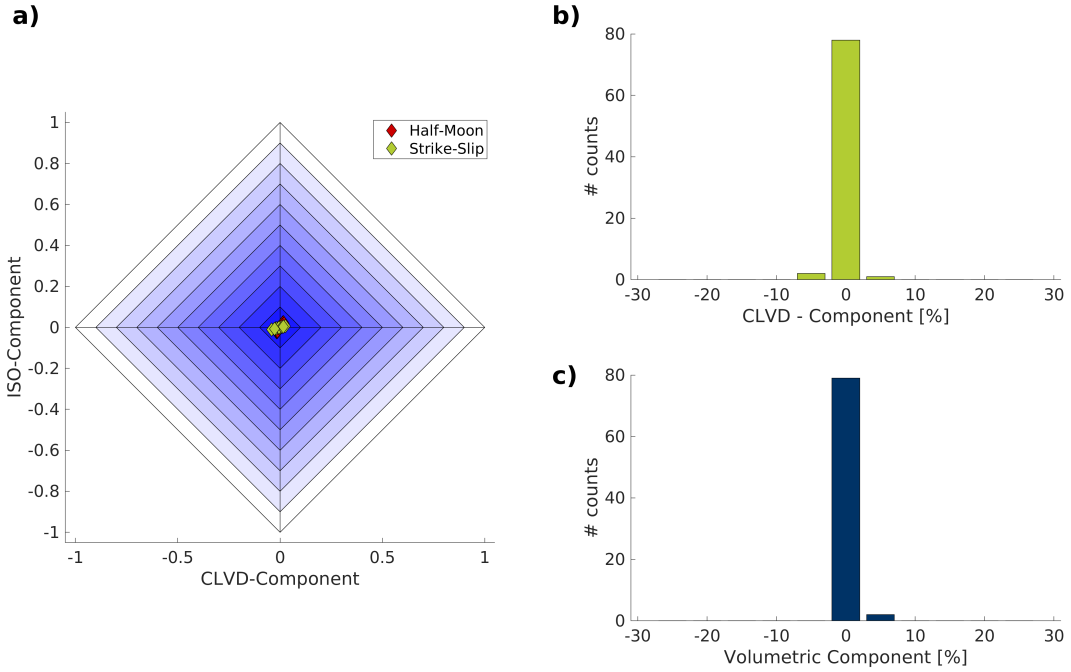

Figure 4.11: **a)** Vavrychuk diamond plot for the inverted mechanisms shown in Figure 4.8 that occur below the layer interface at 1790 m (see Figure 4.9), **b)** histogram of the CLVD-components, **c)** histogram of the ISO-components.

Does the Incorporation of Anisotropy into the Inversion Provides More Accurate Results?

For several case studies (see e.g. Baig & Urbancic [2010] and Staněk & Eisner [2017]), the authors inverted full moment tensors of microseismic events induced by hydraulic fracturing. These events often exhibit non-DC components that I assume to be at least partly caused by seismic anisotropy in the source. Here, I account for the effect of anisotropy by considering its influence on double-couple faulting in the moment tensor. In the following, I discuss the question if this procedure provides a better fit to the data than the search for a double-couple moment tensor. For this, I run an additional grid search assuming double-couple moment tensors.

An obvious approach to answer this question could be a comparison of the values of the misfit function (Equation 4.10) for the presented inversion scheme and double-couple moment tensors. A comparison of both misfits is shown in Figure 4.12. The fit for both inversions is almost equal, i.e. the incorporation of anisotropy only improves the fit insignificantly.

An alternative way to approach this question is to compare the similarity of mechanisms. Here, I assume that under a uniform stress field similar mechanisms are induced and a higher uniformity of mechanisms better represents the nature of induced events. For this comparison, I use the moment tensor decomposition tool I developed in Chapter 3. The results for both inversions are shown in Figure 4.13. First, I separate half-moon and strike-slip events and then compare the inversion results for the proposed anisotropic inversion (blue and green crosses) and for the pure isotropic inversion (yellow and red circles). The error ellipses show the co-variance (2σ) of the data that contain 95% of the data points, if the data is normally distributed. Figure 4.13 shows that the anisotropic inversion provides a more uniform distribution of mechanisms (i.e. smaller area of the error ellipse) than the isotropic inversion. This difference is especially noticeable for the strike-slip events.

Both, the misfit value and the comparison of mechanism similarity shows a slightly, but not significant, better fit for the anisotropic inversion. As discussed above, the level of anisotropy and the orientation of mechanisms only cause small differences between both inversions, a concluding answer on the posed question is impossible using this dataset. This needs to be further tested on datasets with a higher degree of anisotropy and mechanisms that are stronger influenced by anisotropy (for instance normal faulting earthquakes).

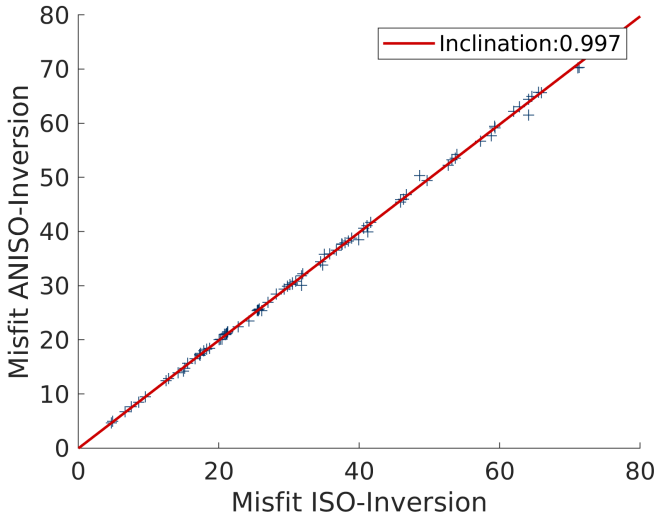

Figure 4.12: Comparison of the value of Δu for the different inversions (isotropic and anisotropic). Misfit values for both inversions are almost equal, the linear fit shows an inclination of 0.997, i.e. the misfit of the ANISO inversion is minimal smaller.

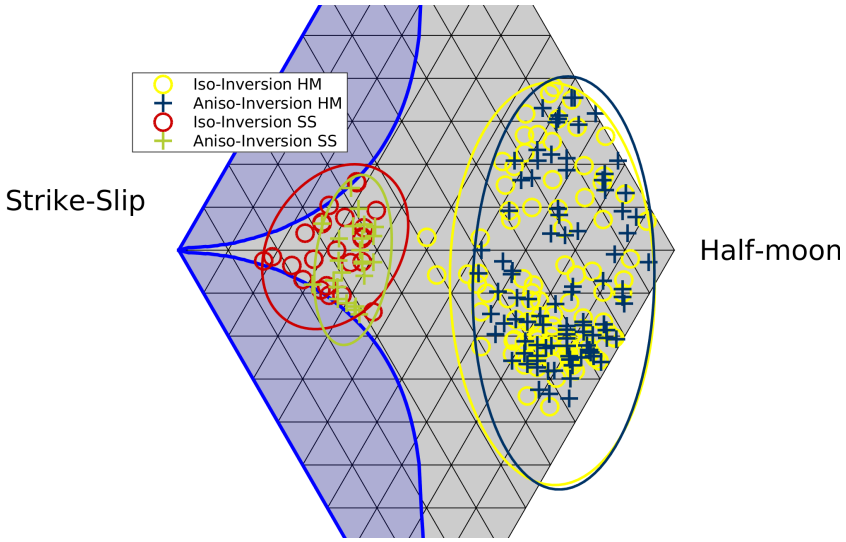

Figure 4.13: Source type plot of the inverted mechanisms for isotropic and anisotropic inversion. Mechanisms obtained using the anisotropic inversion show a higher similarity (smaller error ellipses).

4.4 The Gyration Ellipsoid

In Chapters 5 and 6, I use numerical finite element modeling to investigate the stress field created by an ellipsoidal hydraulic fracture in order to find an explanation for the occurrence of half-moon events. Beside microseismic source mechanisms, the spatial-temporal distribution of events is important to interpret the propagation of the hydraulic fracture and the geomechanical conditions in its vicinity. To compare the modeling results to the field observations in this chapter, I consider in the following additionally the spatial-temporal distribution of the inverted mechanisms. A mathematical tool to analyze this spatial-temporal distribution is the gyration ellipsoid.
The spatial gyration ellipsoid as a sphere that includes a number of given points was firstly introduced by Šolc [1971] and Šolc & Stockmayer [1971] in the field of chemical physics. Shapiro *et al.* [1997, 1999b] introduced the gyration tensor in geophysics using the concept to estimate the permeability of a stimulated rock volume using the spatial distribution of microseismic events. Recently, Tuttle *et al.* [2020] introduced the spatial-temporal gyration that added the temporal dimension to the gyration ellipsoid that allows to investigate the growth of hydraulic fractures with time and a direct comparison with injection pressures and rates. Here, I apply the idea of the spatial-temporal gyration to the Horn-River Basin dataset.
The following derivations and notations follow Grechka [2020a]. The hypocenters of N earthquakes can be considered as a collection of points $\boldsymbol{\xi}_{[N]}$ that coordinates are arranged in a N x 3 matrix. The mass center $\boldsymbol{\xi}_N^{CM}$ of this point collection is given by

$$\boldsymbol{\xi}_N^{CM} = \frac{1}{N}\sum_{n=1}^{N}\boldsymbol{\xi}_{[N]}. \tag{4.12}$$

The gyration tensor $\mathfrak{G}$ is then defined as:

$$\mathfrak{G} = \frac{1}{N}\left(\boldsymbol{\xi}_{[N]} - \boldsymbol{\xi}_N^{CM}\right)^T\left(\boldsymbol{\xi}_{[N]} - \boldsymbol{\xi}_N^{CM}\right). \tag{4.13}$$

$\mathfrak{G}$ is a 3 x 3 symmetric, non-negative definite tensor which can be thus decomposed into its eigenvalues and eigenvectors. The eigenvectors correspond to the orientation of the principal axes of the gyration ellipsoid, the eigenvalues to the corresponding length of the axes. For the following analysis, I only consider the size of the gyration ellipsoid (i.e. its eigenvalues). To study the temporal evolution of the gyration ellipsoid, I consider only the events that occurred before a given time.
Figure 4.14b shows the length of the principal axes of the gyration ellipsoid as a function of time for the data from Horn-River-Basin considering only half-moon events. To

compute the gyration ellipsoid, at least three points (i.e. three half-moon events) are necessary, which is the case at approximately 18 minutes after the start of the treatment. From 18 to approximately 35 minutes, the growth of the largest axis is almost linear (blue dashed line in Figure 4.14b). This linear trend offers the opportunity to estimate the growth rate of the fracture that is given by its inclination that is approximately 4 m/min for this case. This almost linear growth of the fracture is also visible in the RT-plot [Shapiro *et al.*, 1999a] (Figure 4.14a) that shows the distance between an event and the injection point as a function of the occurrence time of the event. This part of the fracture growth is usually referred to as "volume-controlled growth" (see e.g. Shapiro [2015]). The length of the intermediate axis of the gyration describes the height of the stimulated volume that is 30 m at 35min which is in good agreement with the distribution of events in Figure 4.9.
After 35 minutes of stimulation, the growth rate of the stimulated volume is significantly smaller (≈ 0.5m/min). Moreover, events occur closer to the injection point (Figure 4.14a). This trend can either be explained by the development of a more complex fracture network or loss of fracturing fluid due to the increased fracture surface.

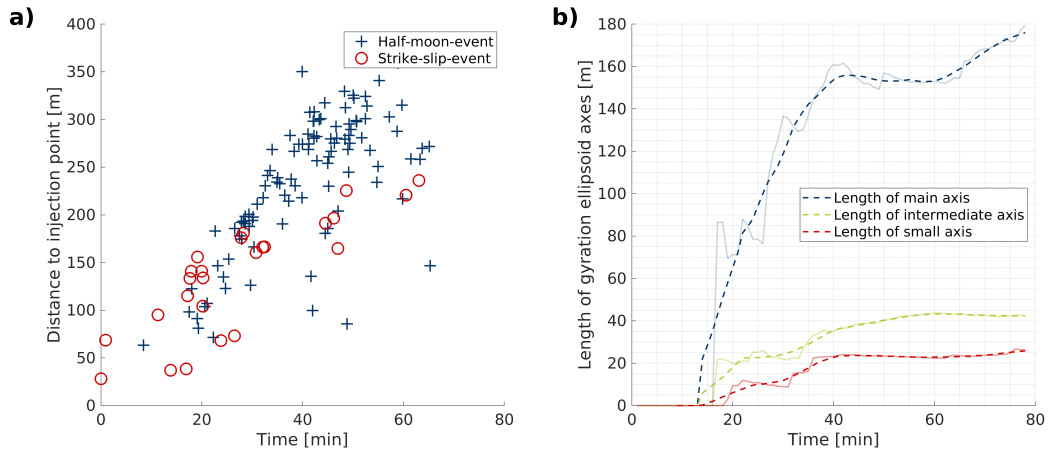

Figure 4.14: **a)** R-T-plot of the analyzed events, red circles mark strike-slip events, blue crosses half-moon events. **b)** Solid lines show the length of the principal axes of the gyration ellipsoid as a function of time, dashed lines are smoothed over a time interval of 10 min.

4.5 Summary of Results and Motivation for Chapters 5 and 6

Using the presented inversion scheme above, I determined moment tensors for 132 events. The source mechanisms show two main types of faulting. A majority of events are half-moon events that can be either characterized by vertical slip on vertical fault planes or horizontal slip on horizontal fault planes. A minority of events ($\approx$ 20%) shows strike-slip faulting.

Half-moon events, in particular these close to the injection point, have vertical fault (or auxiliary) planes that are parallel to the hydraulic fracture. Events occur in narrow depth bands. The lower limit of events coincides with a layer interface. The upper limit is within a layer[1]. The mechanisms exhibit moderate degrees of non-DC components. Half-moon events are not only the dominant mechanism type for this dataset, but similar observations are made by several authors (see discussion in Chapter 5.1.3) at other hydraulic fracturing sites, i.e. half-moon events seem to be the dominant mechanism type for hydraulic fracturing. However, these events have (under typical tectonic stress conditions) a low probability to occur (see discussion in Chapter 5). Their occurrence requires that the stress field in the vicinity of the fracture changes locally, creating optimal conditions for half-moon events. This process and the reasons for this change are up to now still not well understood.

In the following two chapters, I use numerical finite element modeling to investigate in more detail the geomechanical conditions for half-moon events and show how the elastic stresses in the vicinity of a hydraulic fracture are changed, to trigger these type of events.

[1] I show in Chapter 5 that this is most probable close to the vertical upper limit of the hydraulic fracture itself.

CHAPTER 5

A 2D GEOMECHANICAL MODEL FOR HYDRAULIC FRACTURING

In the previous chapter, I inverted for source mechanisms of events induced by hydraulic fracturing. Accounting for the influence of anisotropy on the radiation pattern leads to a more consistent distribution of mechanisms. A majority of mechanisms show half-moon faulting that is typical for HF, but unusual for tectonic seismicity. Thus, these events seem to be directly fracturing-related. In this chapter, I elaborate on the stress conditions that are needed to create half-moon events and show with a numerical 2D finite element modeling, how and where these conditions are created during hydraulic fracturing. The chapter is in wording and with regards to content mainly equal to our work published in Boitz & Shapiro [2021]. Figures 5.1, 5.2 and 5.4-5.11 are equal to the ones presented in the paper, Figure 5.3 was not included in the original version of the paper. I acknowledge the contribution of my co-author, Prof. Serge Shapiro who initially suggested to study shear stresses and the resulting stress rotations at layer interfaces and who contributed to improve the initial and revised manuscript.

5.1 Introduction to Geomechanical Modeling

5.1.1 Discussion of the Term "Half-Moon Event"

I have already used the term "half-moon event" for a special type of microseismic source mechanism that either exhibits horizontal slip on horizontal fault planes or upward or downward slip on a vertical fault plane. These events are denoted half-moon events because of the characteristic shape of their radiation pattern. The usage of this term is controversial and considered by several authors as slang. Among others, Staněk & Eisner [2017] used the term "dip-slip" to describe these events. However, in global seis-

mology, the term ”dip-slip” describes upward or downward faulting (a rake of ±90°) on an arbitrary inclined fault plane (including also normal and thrust faulting). In this sense, half-moon events are only a subgroup of dip-slip events that have strictly vertical or horizontal fault planes. In order to not always make this constraint for the term dip-slip, I maintain to use the term half-moon in this thesis.

5.1.2 Geomechanics of Hydraulic Fracturing

During hydraulic fracturing (HF) stimulations fluids are injected under high pressure in sedimentary layers. If the injection pressure exceeds approximately the minimum principal stress plus the formation tensile strength [Hubbert & Willis, 1957; Jaeger *et al.*, 2007] a hydraulic fracture is created. This fracture ideally opens in the direction of the minimum principal stress and propagates in the plane normal to the minimum principal stress. Additional to the stress distribution, the propagation depends on local changes in lithology, layer thickness, among others.
The fracture opening is frequently accompanied by microseismic events, which are triggered along preexisting natural fractures or weakness surfaces in the rocks surrounding the fracture [Maxwell, 2014], mainly due to changes in pore pressure and local stress, caused by the injection and propagation of the hydraulic fracture. The locations of microseismic events and their mechanisms can be used to evaluate the success of the hydraulic fracturing treatment. As hydraulic fracturing is usually performed in layered shales, a highly accurate anisotropic velocity model is essential since anisotropy, as discussed in Chapter 2, has a significant impact on both locations and source mechanisms of microseismic events [Boitz *et al.*, 2018].
Multiple studies [Staněk & Eisner, 2013, 2017; Rutledge *et al.*, 2015, 2016; Grechka & Heigl, 2017; Boitz & Shapiro, 2018] that I review in more detail in section 5.1.3, consistently observed half-moon events. However, the geomechanical conditions for half-moon events are still not fully understood. Among others, it is still debated, if the slip occurs on the vertical or the horizontal plane. Rutledge *et al.* [2016] and Staněk & Eisner [2017] discussed the conditions for these event type and propose models which explain half-moon events by slip along weak bedding planes. Previously, Chuprakov & Prioul [2015] develop a model later used by Weng *et al.* [2018] which also explains half-moon events by slip along bedding planes. Recently, Rutledge [2019] revisited the topic and concluded that bedding plane slip is rather improbable.
Zoback & Snee [2018] show that both, slip on the horizontal and on the vertical plane, can explain half-moon events depending on the natural stress regime. In thrust faulting regimes, the slip is expected to occur on the horizontal plane, in normal faulting

regimes along the vertical plane. My study and the following explanation in section 5.2.2 show that under typical tectonic conditions half-moon events are unlikely to occur. Simultaneously, one should expect to observe earthquakes with a variety of mechanisms types, before half-moon events are induced. However, this expectation contradicts observations found in the studies discussed in section 5.1.3.
In this chapter, I aim to find an explanation to overcome this discrepancy. For this, I propose a simple numerical 2D finite-element model that provides a principle explanation for most of the observations from the case studies. I review the basics of geomechanics (see e.g. [Zoback, 2007]) and elaborate on the conditions needed to create local stress field rotations. I show that under specific stress conditions (which are frequently created during hydraulic fracturing) predominantly half-moon events with different shearing sense at different distinct depths and on opposite fracture sides are induced. These stress conditions are either created at layer interfaces, where the elastic properties of rocks vary or at the tips of hydraulic fractures. For the case of layering, I additionally apply two sets of boundary conditions and show that half-moon events can be induced independently of the natural faulting regime in both normal faulting and strike-slip environments. The two models generate local stress field rotations resulting in different shearing senses of half-moon events, which are consistent with Zoback & Snee [2018].

5.1.3 Case Study Review

Beside the case study presented in Chapter 4 (later referred to as 'Horn-River study'), half-moon events are found at several hydraulic fracturing sites. Here, I give an overview of three additional publications to elaborate on typical characteristics of half-moon events that I try to reproduce with the numerical modeling in this chapter.
Staněk & Eisner [2013, 2017] analyze seismicity induced by hydraulic fracturing in Arkoma Basin and recorded by a surface star-like array. They observed half-moon events whose vertical planes are parallel to the hydraulic fractures. Two groups of half-moon events can be identified that show opposed shear senses. Beside half-moon events, several strike-slip events at the edges of the seismic cloud are observed, which are typical for the natural seismicity in the region. Staněk & Eisner [2017] additionally proposed a model to explain their observations. In their interpretation, the aseismic tensile opening of the hydraulic fracture perturbs the stress field in its vicinity and creates bedding plane slip normal to the hydraulic fracture in the direction of σ_{min}.
Rutledge *et al.* [2015, 2016] interpret microseismic events from hydraulic fracturing in Barnett shale monitored by a vertical downhole receiver array. They observe events occurring at narrow depth bands that also show opposed shear senses. As in the previous

example, the vertical plane is aligned with the hydraulic fracture. The observations are also interpreted to be related to bedding plane slip.
Grechka & Heigl [2017] analyze potency and moment tensors of microseismicity created by hydraulic fracturing in the Bakken field. The events are registered and located by several vertical downhole receiver arrays. The case study shows again half-moon events, whose vertical planes have the typical alignment with the hydraulic fracture. Events located at greater distances to the fracture exhibit a horizontal rotation of this vertical plane, i.e. the vertical plane is rather normal to the hydraulic fracture than parallel. Both potency and moment tensors are predominately double-couple. Moment tensors show slightly higher ISO-components which might be explained by the impact of source anisotropy (see discussion in Chapter 2).
Summarized, the following common characteristics of half-moon events can be identified:

1. Half-moon events are consistently found in all four studies and are the predominant event type.

2. Half-moon events are sometimes accompanied by a minority of events typical for natural faulting in the specific region (Staněk & Eisner [2017] and Horn-River study).

3. Microseismic events are located in narrow depth bands, i.e. they occur at distinct depth ([Rutledge *et al.*, 2015, 2016] and Horn-River study).

4. The vertical plane of half-moon events is mostly aligned with the hydraulic fracture (all 4 case studies) and tends to rotate horizontally at greater distances to the injection point (Grechka *et al.* [2017] and Horn-River study).

5. Half-moon events show opposed slip orientations (all 4 studies) that occur at different depths (Rutledge *et al.* [2016]).

5.2 Theory of Geomechanics

5.2.1 Mohr-Coulomb Failure Criterion

The subsurface contains natural preexisting fractures that are already critically stressed. Here, I assume that faulting is possible along arbitrary directions if the Mohr-Coulomb conditions are satisfied. Already small changes in stress or pore pressure can cause these fractures to fail. A classical model to explain this failure is the Mohr-Coulomb

failure criterion (shown in Figure 5.1) that I explain in the following. The derivations mainly follow Shapiro [2015]. To analyze the stability of natural cracks so-called Mohr-Coulomb circles are used. A Mohr-Coulomb circle is defined by its center σ_m and its radius R:

$$\sigma_m = |\sigma_i + \sigma_j|/2 \tag{5.1}$$

$$R = |\sigma_i - \sigma_j|/2. \tag{5.2}$$

Usually, this circle is rather plotted in the domain of two effective normal stresses than in the domain of normal stresses. The effective stress is the absolute value of the normal stress minus the pore pressure,

$$|\sigma_n'| = |\sigma_n| - P_p. \tag{5.3}$$

Basically, this shifts the whole circle parallel to the x-axis toward the origin. Since I consider in the following a purely elastic medium, the pore pressure is neglected and I plot Mohr-Coulomb circles in the domain of normal stresses.
The principal stresses create shear stresses τ on preexisting cracks that only depend on the angle between the maximum principal stress and the orientation of the respective crack plane θ,

$$|\tau(\theta)| = \sin(2\theta)\, R. \tag{5.4}$$

If τ is smaller than τ_{crit} a natural fracture is considered to be stable. τ_{crit} is usually defined by a linear relationship

$$|\tau_{crit}| = C_0 + \mu_f |\sigma_n|, \tag{5.5}$$

where C_0 is the cohesion. The right hand side describes the friction force per a unit surface of the fault. The slope of this failure line only depends on the static friction coefficient μ_f. This coefficient specifies the point, where the Mohr-Coulomb circle first touches the failure line. Additionally, it defines the optimal orientation angle

$$\theta_{opt} = \frac{1}{2}\arctan\left(\frac{1}{\mu_f}\right) \tag{5.6}$$

between a fault and the maximum principal stress, i.e. the angle of the fault that is exposed to the most critical shear stresses (in the sense that τ_{crit} - τ becomes negative). Typically, μ_f is in the range of 0.6 to 1 leading to θ_{opt} in the range of approximately 30° to 22.5°.
The fault plane shown in Figure 5.1 is optimally oriented with respect to the maximum principal stress (i.e. the vertical stress). In other words, this is the first event type

we would observe during an increase in pore pressure, if preexisting fractures with all orientations exist. In typical tectonic settings, where one of the principal stresses is vertical, extremely high pore pressures are needed to cause half-moon events as shown in Figure 5.2. Additionally, we should observe significantly more earthquakes on a variety of different fault plane orientations and not exclusively half-moon events [Zoback & Snee, 2018]. To create predominately these events, the maximum principal stress needs to deviate by approximately θ_{opt} from the vertical or the horizontal direction. Then, horizontal or vertical fault planes become optimal (close to the green star event in Figure 5.1). For this, a significant local rotation of the stress field is required. The optimal orientation of the principal stresses for half-moon events is also shown in Figure 5.3.

5.2.2 Why do we Hardly see Half-Moon Events in Nature ?

As stated in the introduction, half-moon events are the typical source mechanism for hydraulic fracturing. However, if we analyze tectonic seismicity, we hardly observe this event type anywhere in nature. This can be explained by the specific stress conditions that are needed for half-moon events and that I discussed above.
In typical tectonic settings one of the three principal stresses is oriented vertically. The vertical stress in the subsurface is basically defined by the density of the overburden rock mass ρ, the constant of gravitation g and the depth z:

$$\sigma_v = g \int_0^z \rho(z) dz. \tag{5.7}$$

Without significant lateral variations in density or topography, the vertical stress is laterally constant and can be considered as a principal stress. This is especially the case for sedimentary basins that often exhibit uniform layering and are usually of interest for hydraulic fracturing.
If one principal stress is vertical, the other two are horizontal. For half-moon events this means that the angle between the maximum principal stress and the fault plane is for all considered stress regimes either 0 or 90 degrees. This is far from the optimal angle of $\theta_{opt} \approx 30°$ (see explanation in section 5.2.1). Thus, local rotations of the stress field are needed to explain solely half-moon events. In the following, I discuss the conditions needed for such a rotation and how these conditions can be created during hydraulic fracture stimulation.

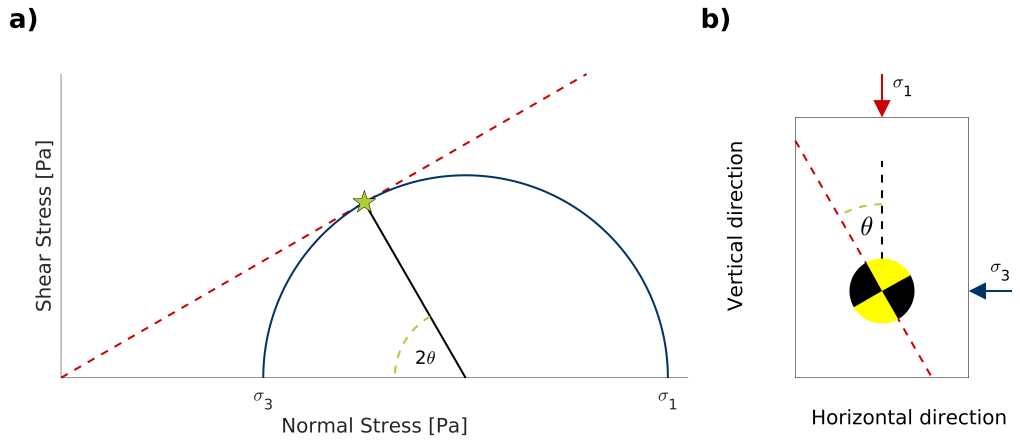

Figure 5.1: **a)** Sketch of a Mohr-Coulomb circle. The size of the circle is defined by the differential stress σ_1 - σ_3, respectively. The red dashed line indicates the failure line. Where the circle touches the failure line (red star), a fault plane with an inclination of θ with respect to the maximum principal stress (i.e. vertical direction) fails. This results in a normal faulting earthquake (side view of beach ball in **b)**) under conditions, where σ_1 is the vertical and σ_3 the horizontal principal stress.

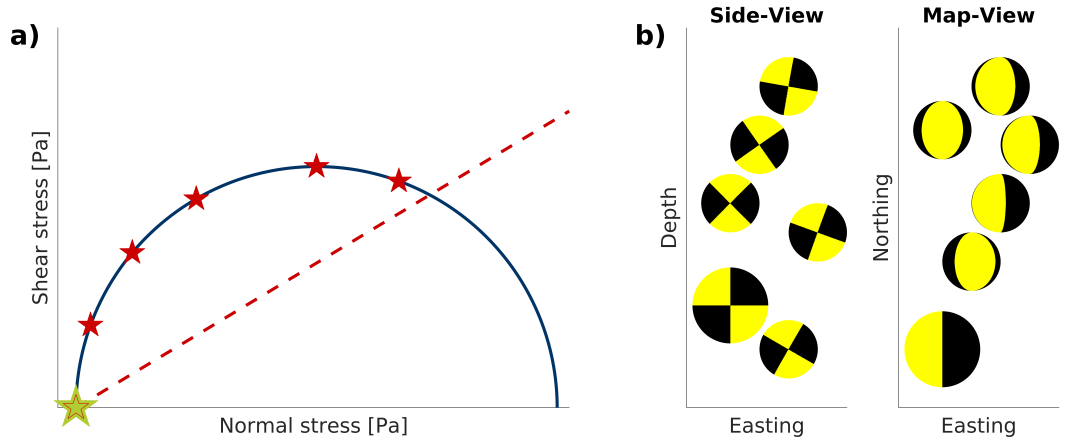

Figure 5.2: **a)** Mohr-Coulomb circle with several fault orientations that failed (red stars) and their corresponding radiation patterns in **b)**. To induce a half-moon event (green star) the pore pressure needs to be as high as the minimum principal stress. In such a situation half-moon events may occur. However, other fault orientations (red stars) are more likely and will fail earlier by the application of a gradually increasing fracturing pressure.

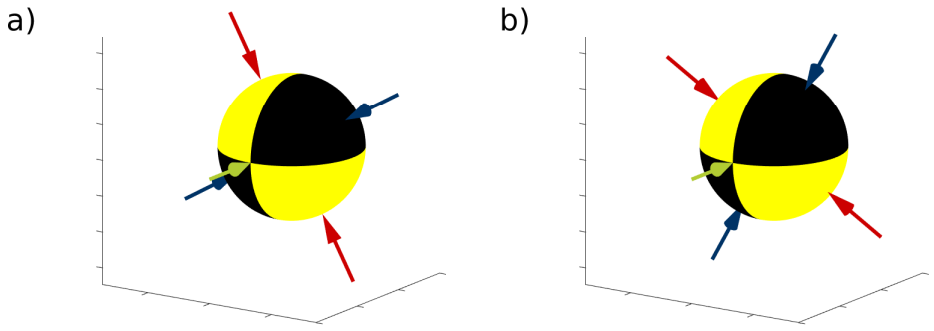

Figure 5.3: Optimal orientation of the principal stresses (σ_1 in red, σ_2 in green and σ_3 in blue) to create half-moon events. In **a)** the slip occurs on the vertical fault plane, in **b)** on the horizontal fault plane.

5.2.3 The 2D Stress Tensor

To approach this question, I model the effect of the pressure of a hydraulic fracture in various tectonic settings. In this work, I do not consider the creation and propagation of the tensile hydraulic fracture itself, which is in detail described in Detournay [2016] and Lecampion *et al.* [2018]. I focus on the elastic medium behind the wall of the hydraulic fracture that is exposed to a modified compressional stress acting normally to the fracture wall. This stress modification is caused by the fluid pressure in the body of the fracture. Since the hydraulic stimulation is usually performed in shales with very low permeabilities and the fracturing operations usually occur in the order of hours, I neglect all dynamic poroelastic effects in the rocks surrounding the fracture and consider these rocks as elastic ones with corresponding parameters of a poroelastic undrained medium.

I investigate in detail the stresses created by hydraulic fracturing in normal and strike-slip faulting regimes. For simplicity, I assume a vertical hydraulic fracture in a horizontally layered medium. In thrust regimes, a hydraulic fracture does not introduce stress rotations in horizontally layered media (see below). Only rotations at the tips may occur (see section 5.4.7). In this chapter, I consider the stress distribution in the plane normal to the longest axis of the hydraulic fracture. Moreover, I assume that the HF is infinitely long and consider its vertical cross-sections. Since all cross-sections are identical, any stress rotation will occur in a vertical plane with respect to the y-axis, and we can reduce our consideration to a 2D model. I denote the horizontal axis by x and the vertical axis by z. Therefore, I can consider a 2D sub-matrix of the stress tensor:

$$\sigma_{ij} = \begin{pmatrix} \sigma_{xx} & \sigma_{xz} \\ \sigma_{zx} & \sigma_{zz} \end{pmatrix}. \tag{5.8}$$

Exactly this sub-matrix will be modified, which causes a stress rotation. The principal stresses are then given by the two eigenvalues $\sigma_{1/2}$ and their directions by the eigenvectors $\bar{p}_{1/2}$ of σ_{ij}.
For further analysis they are expressed here explicitly:

$$\sigma_{1/2} = \frac{1}{2}\left[\sigma_{xx} + \sigma_{zz} \pm \xi\right], \tag{5.9}$$

where ξ is defined as

$$\xi = \sqrt{(\sigma_{xx} - \sigma_{zz})^2 + 4\sigma_{xz}^2}. \tag{5.10}$$

The two eigenvectors follow as

$$\bar{p}_1 = \begin{pmatrix} 2\sigma_{xz} \\ \sigma_{zz} - \sigma_{xx} + \xi \end{pmatrix}; \qquad \bar{p}_2 = \begin{pmatrix} 2\sigma_{xz} \\ \sigma_{zz} - \sigma_{xx} - \xi \end{pmatrix}. \tag{5.11}$$

Note that these eigenvectors are only valid in the case of non-zero shear stresses (in the case of zero shear stresses, they must be considered in the limit $\sigma_{xz} \to 0$). In this particular case, the principal stress directions coincide with the x- and z-directions, i.e. they are oriented vertically and horizontally, respectively. The orientation of the principal stresses can be also expressed by the angle θ_R that describes the angle to rotate the principal stresses into the xz-coordinate system:

$$\tan(2\theta_R) = \frac{2\sigma_{xz}}{\sigma_{xx} - \sigma_{zz}}. \tag{5.12}$$

Let us investigate equations 5.11 and 5.12 in more detail: if σ_{xx} and σ_{zz} are significantly different from each other and shear stresses are small, the principal directions of the stresses are close to vertical and horizontal. Accordingly, the rotation θ_R tends to zero.
However, if σ_{xx} and σ_{zz} are nearly equal, the shear stresses in Equation 5.11 can become dominant. In the extreme situation of $\sigma_{xx} = \sigma_{zz}$ we will observe principal stresses with an angle of 45° with respect to the coordinate axes. We obtain the same result using equation 5.12: if σ_{xx} and σ_{zz} are nearly equal, the denominator goes to zero and we obtain a rotation angle of 45°.
In summary, half-moon events can be observed predominately under the following conditions: If the stress field is appropriately oriented, natural horizontal or vertical planes of weakness become nearly critical. Such stress fields require a significant local stress rotation. A rotation of the stress field is promoted in domains, where the magnitude of vertical and horizontal stresses are close and/or shear stresses are high.

5.3 2D Geomechanical Modeling

After having derived the specific stress conditions to create half-moon events, I investigate in the following how and where these conditions are created by a hydraulic fracture. In particular, I address the question, how hydraulic fractures change the stress field in the vicinity of the fracture itself. For this, I consider three different scenarios, the one that shows the effect of an infinitely high fracture on a layered rock mass (model I, see Figure 5.4), the one that takes into account the finiteness of the fracture in a homogeneous medium (model II, see Figure 5.5) and the one that combines both effects (model III). Model I is embedded in the two different sets of boundary conditions to model hydraulic fracturing under normal faulting conditions and to model a special case of hydraulic fracturing in strike-slip domains. For the second and third model, the problem for a strike-slip regime cannot be simplified to two dimensions, since the stress rotation is more complex and requires a 3D model (see discussion in section 5.4.6). Hydraulic fracturing under general strike-slip conditions is considered in Chapter 6. Thus, models II and III are only analyzed for normal faulting conditions. Because hydraulic fracturing in thrust faulting domains is rare, I do not consider it here.

5.3.1 Model I

Depending on the model, different initial principal stress distributions exist. These tectonic conditions are locally replaced by introducing a vertical hydraulic fracture. In other words, introducing a hydraulic fracture modifies the boundary conditions for the applied elastic stresses. Correspondingly, I perform a 2D elastic finite-element modeling (FEM) using the Comsol Multiphysics® software [COMSOL-Multiphysics®, V 5.4].
Here, I consider two specific situations:

- Model I - Normal Faulting: The tectonic regime is a normal faulting (NF) environment, so the maximum principal tectonic stress is vertical, the minimum principal stress coincides with the direction of fracture opening. As discussed before, the injection pressure needs to be higher than σ_3 to open a fracture, so in the vicinity of the fracture, the minimum principal stress is replaced by the bottom hole injection pressure (i.e. fracturing pressure p_{frac}).
- Model I - Strike-Slip: The tectonic regime is initially a strike-slip (SS) environment, so the maximum principal tectonic stress is horizontal, the minimum principal stress is also horizontal. Under this condition, a 2D model that has one vertical axis does not lie with the σ_1-σ_3-plane. Therefore, I apply a high injection

pressure (greater than tectonic σ_1) inside our fracture. Thus, the minimum principal stress in the vicinity of the fracture becomes vertical, the maximum principal stress is horizontal, locally the stress field is close to a thrust environment (see Table 5.1).

For both 2D models, I consider a slice of a 3D geometry (i.e. effectively assuming an infinitely long HF in the y-direction) in the σ_1-σ_3 plane applying the following boundary conditions. From the left side, I apply a fracturing pressure p_{frac} which is given by the fluid pressure in the body of the hydraulic fracture (42.5 MPa for NF and 50 MPa for SS). At the right model boundary, the horizontal strain ϵ_{xx} is set to zero. From the top, a lithostatic pressure (50 MPa for NF and 40 MPa for SS) is applied. The lower boundary is modeled as a fixed boundary (Figure 5.4). The model itself consists of five rock layers with different thicknesses and elastic properties given in Table 5.2.
Based on these conditions, I perform numerical computations and obtain the full 2D stress tensor for each point within the model. From this, I compute the minimum and maximum principal stresses and their directions as described earlier. Additionally, I estimate the angle θ_R between the maximum principal stress and horizontal or vertical direction that needs a distinct deviation from these directions to create half-moon events. Having both, principal stresses and their orientations in respect to vertical and horizontal fractures, I use Mohr-Coulomb circles to analyze the stability of these preexisting fractures.

		σ_1	σ_2	σ_3
Normal-Faulting	tectonic conditions	$\sigma_1 = \sigma_v$	$\sigma_2 = \sigma_H$	$\sigma_3 = \sigma_h$
	fracture vicinity	$\sigma_1 = \sigma_v$	$\sigma_2 = \sigma_H$	$\sigma_3 = p_{frac} > \sigma_h$
Strike-Slip	tectonic conditions	$\sigma_1 = \sigma_H$	$\sigma_2 = \sigma_v$	$\sigma_3 = \sigma_h$
	fracture vicinity	$\sigma_1 = p_{frac} > \sigma_H$	$\sigma_2 = \sigma_H$	$\sigma_3 = \sigma_v$

Table 5.1: Tectonic stress conditions and stress conditions in the vicinity of the hydraulic fracture for the two sets of boundary conditions for model I.

	vp [m/s]	vs [m/s]	ρ [kg/m^3]	E [GPa]	ν [-]	h [m]	ToL [m]
L 1	3500	2021	2700	27.6	0.25	40	1700
L 2	3300	1905	2700	24.5	0.25	30	1740
L 3	3600	2079	2700	29.2	0.25	10	1770
L 4	3100	1938	2500	22.1	0.18	40	1780
L 5	3500	2021	2700	27.6	0.25	100	1820

Table 5.2: Elastic parameters of the five layers (P and S-wave velocities (vp and vs), density ρ and corresponding Young's moduli E and Poisson's ratios ν), the layer thickness (h) and the top of each layer (ToL) for model I.

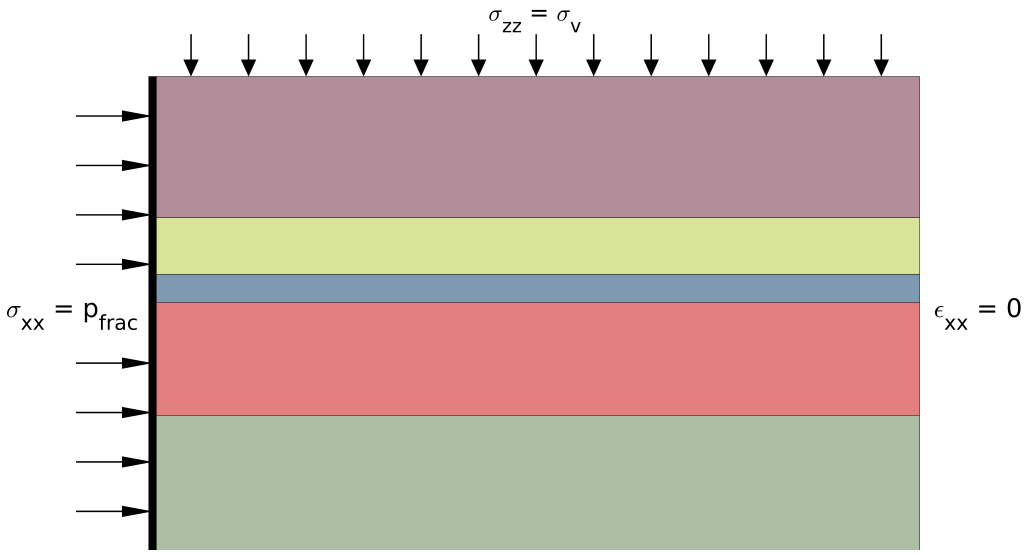

Figure 5.4: Model configuration for model I with the hydraulic fracture on the left side. From the left model boundary a horizontal stress is applied that is equal to the fluid pressure in the body of the hydraulic fracture, from top a vertical stress is applied, the strain at the right model boundary is set to zero. The horizontal extent of the model is 100 m. The colors indicate layers with different elastic properties, see Table 5.2.

5.3.2 Model II

In the previous model, the complex stress perturbations close to the upper and lower vertical limits (fracture tips) are intentionally neglected to investigate only the effect of layering on the stress field. In this model (model II) I consider stress field rotations at these tips, caused by the elliptical shape of the fracture. The model setup is shown in Figure 5.5. From the top of the model again a vertical stress equal to the lithostatic pressure is applied (σ_v=50MPa). From both horizontal sides of the model, I apply a horizontal stress equal to the minimum horizontal stress, σ_h=40MPa (which is approximately equivalent to the boundary condition $\epsilon_{xx} = 0$ at model I). The lower boundary is again modeled as a fixed surface. In this second model, the hydraulic fracture has a finite extent with an elliptical shape with a height of 80 m and a fracture width of 0.01 m. Normal to the elliptical surface a pressure equal to the fluid pressure inside the hydraulic fracture is applied (p_{frac} = 45MPa). Because the fracture is very thin, the fluid pressure acts in most parts of the model almost in a purely horizontal direction, only close to the fracture tips the stress normal to the fracture surface locally rotates and has significant vertical components (see red arrows in Figure 5.5). The hydraulic fracture is embedded into a homogeneous isotropic medium (V_p = 3500m/s, V_s = 2021m/s, ρ = 2500kg/m^3). Due to the elliptical shape of the fracture, a characteristic

stress distribution at the tips can be observed that has been also shown by Warpinski *et al.* [2004] in their analytic solution of a similar problem.

5.3.3 Model III

In the third model, I analyze the influences of both effects (layering and tip effects) simultaneously. For this I apply the same boundary conditions as for model II, the only difference is a thin central layer that has a higher stiffness (Table 5.3).

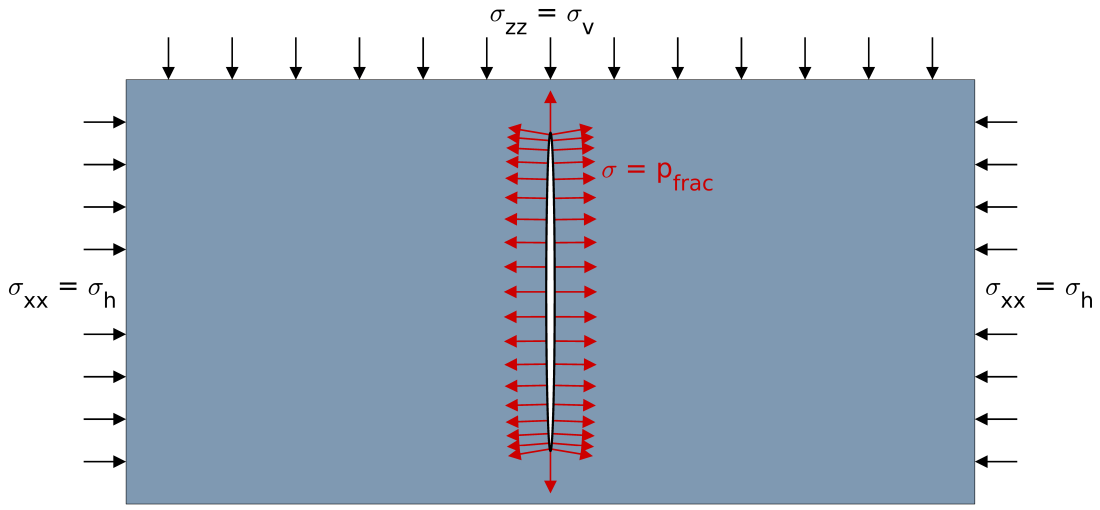

Figure 5.5: Configuration of model II. From the top a vertical stress equal to the vertical tectonic stress (σ_v), from the left and right a horizontal stress equal to (σ_h) is applied. The hydraulic fracture is assumed to be elliptic. Normal to the fracture wall (red arrows) a stress equal to the fluid pressure (p_{frac}) is applied.

	vp [m/s]	vs [m/s]	ρ [kg/m^3]	E [GPa]	ν [-]	h [m]	ToL [m]
L 1	3500	2021	2500	25.5	0.25	240	0
L 2	3900	2252	2500	31.7	0.25	20	240
L 3	3500	2021	2500	25.5	0.25	240	260

Table 5.3: Elastic parameters of the three layers (P- and S-wave velocities (vp and vs), density ρ and corresponding Young's moduli E and Poisson's ratios ν), the layer thickness (h) and the top of each layer (ToL) for model III.

5.3.4 Validity of Model Assumptions

The presented models have two limitations that I shortly address here. The first model assumes an infinitely high fracture with a fluid pressure that is uniformly distributed within the fracture. In this model, I neglect in particular the shape of the fracture itself that is influenced by the rock properties. In stiffer layers the fracture is expected to be thinner than in weaker layers, creating locally a curved fracture surface. This might create shear stresses additional to the shear created by layering. The effect of shear stresses created by the shape of the fracture is addressed in models II and III. The second assumption is that the fluid pressure inside the fracture is uniformly distributed. In reality, the pressure along the fracture height decreases. Especially in the case of our models II and III where the fracture has a finite extent, I assume that the height of the fracture is small enough to neglect this effect.

5.4 Results of 2D Modeling

5.4.1 Model I

As the result of the FEM, I obtain a distribution of all components of the considered 2D sub-matrix of the stress tensor within the model (Figure 5.6). At the left model boundary, the horizontal stress is equal to the applied boundary pressure in the body of the hydraulic fracture (gravity-related effects are neglected here). Due to the variation of elastic rock properties, we observe significant and very sharp variations of the horizontal stress. Especially close to layer interfaces, the stresses change rapidly, clearly indicating the layering. Generally, we observe smaller stresses in weaker rocks. The vertical stress is in most parts of the model nearly homogeneously distributed. Significant variations are only observed near the injection boundary. Rock properties that change with depths additionally generate shear stresses close to layer interfaces. These shear stresses are highest close to the surface of the hydraulic fracture and vanish to the right-hand side of the model. Their magnitude is mainly governed by the elastic contrast between corresponding layers. The spatial extent of the surface patches with significant shear stresses is controlled by the layer thickness. The principal stress directions can be obtained from this stress distribution (Equation 5.11) for each point in the medium. The deviation of the maximum principal stress from vertical direction for NF tectonics and from horizontal direction for SS tectonics is given by the rotation angle θ_R in Equation 5.12. The rotation angle for both models will be presented in the next sections for every location inside the model.

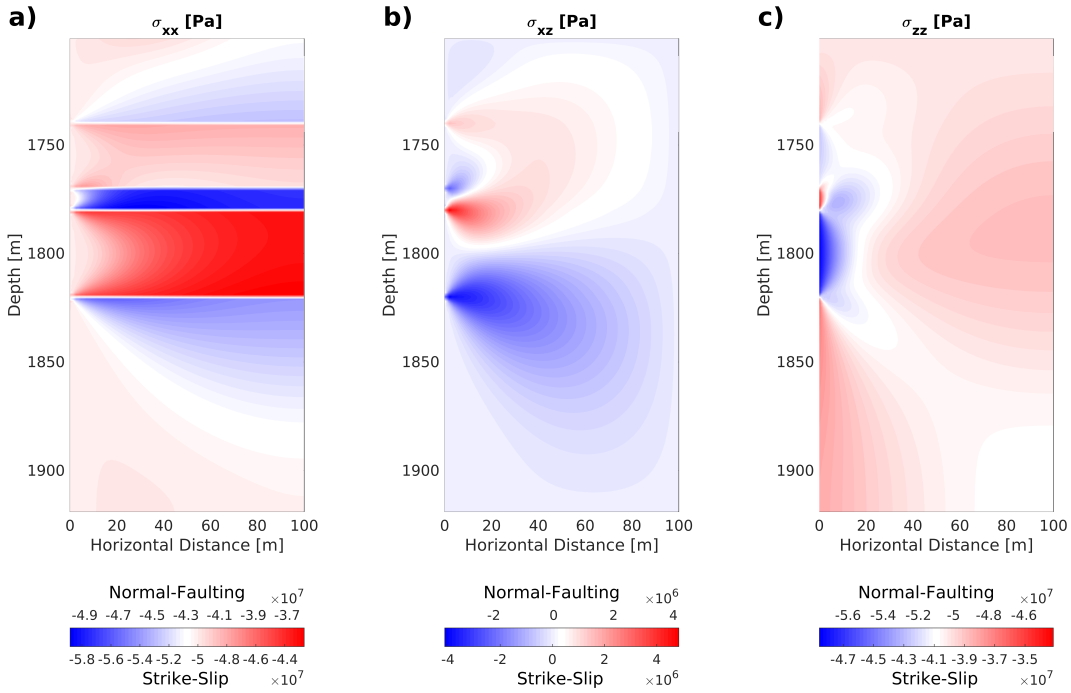

Figure 5.6: Stress distribution for model I, **a)** horizontal compressional stresses, **b)** shear stresses and **c)** vertical compressional stresses. The values above each colorbar corresponds to the normal faulting model, the values below to the strike-slip model. The stress distribution is equivalent for both models, only absolute values differ.

5.4.2 Model I - Normal Faulting

In the NF model, we observe significant stress field rotations of up to 30° within the third and at the top of the fifth layer (Figure 5.7a). Here, σ_1 deviates from the initial vertical orientation. In Figure 5.7c, I present Mohr-Coulomb circle plots for a horizontal profile at a depth of 1823 m (close to the layer interface) to investigate the stability of preexisting vertical cracks. Green stars at each circle show the pairs of coordinates (normal stress, shear stress) for a vertical faulting plane (criticality of vertical cracks). If the pore pressure is increased during the hydraulic treatment (i.e. going from green to red failure line in Figure 5.7c), vertical fractures are then preferably oriented in respect to the stress field, in other words, half-moon events are the most probable mechanism type. Due to the different sign of the shear stress (see also Figure 5.6b), opposed slip directions at different depths are observed. Possible locations and slip directions of half-moon events are schematically shown in the sketch in Figure 5.7b.

In contradiction to previous publications (for instance [Staněk & Eisner, 2017]), I show that the slip of half-moon events occurs most likely on vertical fault planes in normal faulting domains. Failure on horizontal fault planes in normal faulting regimes is very improbable.

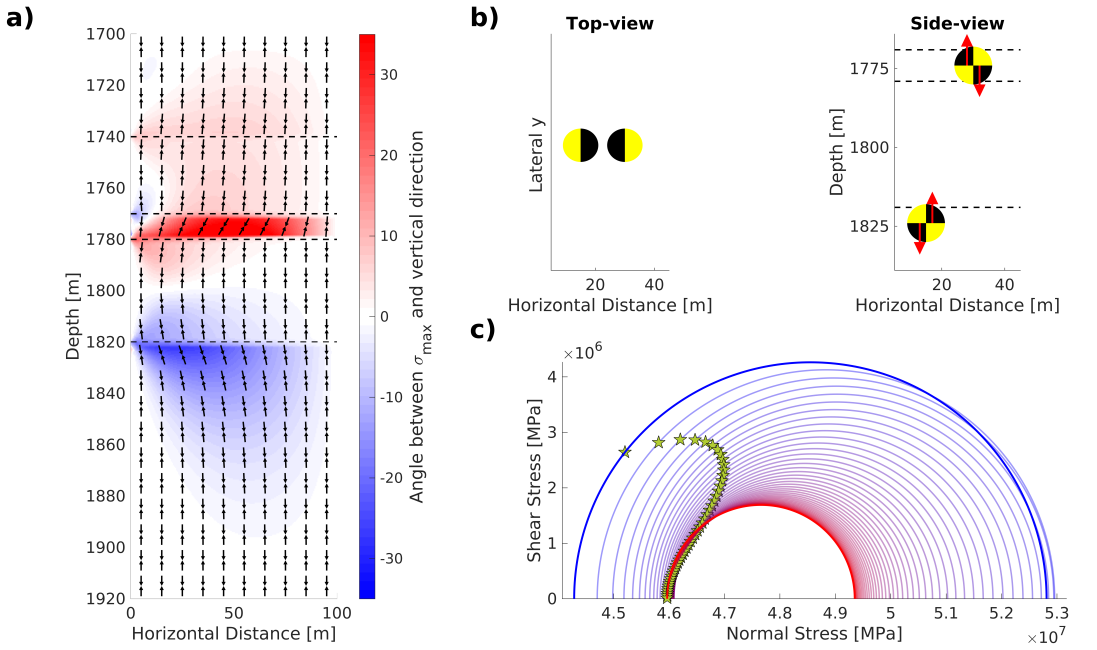

Figure 5.7: **a)** Angle between σ_1 and the vertical direction for the NF model. Black arrows show the orientation of σ_{max} for each location inside the model. **b)** Sketch showing that parts of the model where half-moon mechanisms are probable, red arrows indicate slip orientation. **c)** Mohr-Coulomb circles for a horizontal profile at a depth of 1823 m, close to a layer interface in an area of rotated stress. Green stars at each Mohr-Coulomb circle show the pairs of coordinates (normal stress, shear stress) for a vertical faulting plane (criticality of vertical cracks). In the vicinity of the fracture, these are closest to the failure line, i.e. vertical cracks are most critical. The blue circle corresponds to a location close to the fracture, the red circle to a location at the right model boundary.

5.4.3 Model I - Strike-Slip

In the strike-slip case, significant rotations of the stress field up to 30° are observed at the top and bottom of the fourth layer (Figure 5.8a). Analogously to the normal faulting case, Mohr-Coulomb circles for a horizontal profile through the medium at a depth of 1818 m (close to the layer interface) are plotted in Figure 5.8c. Here each green star at the Mohr-Coulomb circle show the pairs of coordinates (normal stress, shear stress) for a horizontal faulting plane (criticality of horizontal cracks). In this case, horizon-

tally oriented cracks are then optimally oriented and are most likely to fail as dip-slip events. Again, we observe rotation angles of approximately -30° at the upper and 30° at the lower interface, which indicate opposed slip directions. Most probable source locations and slip directions for half-moon events for this model are schematically shown in Figure 5.8b.

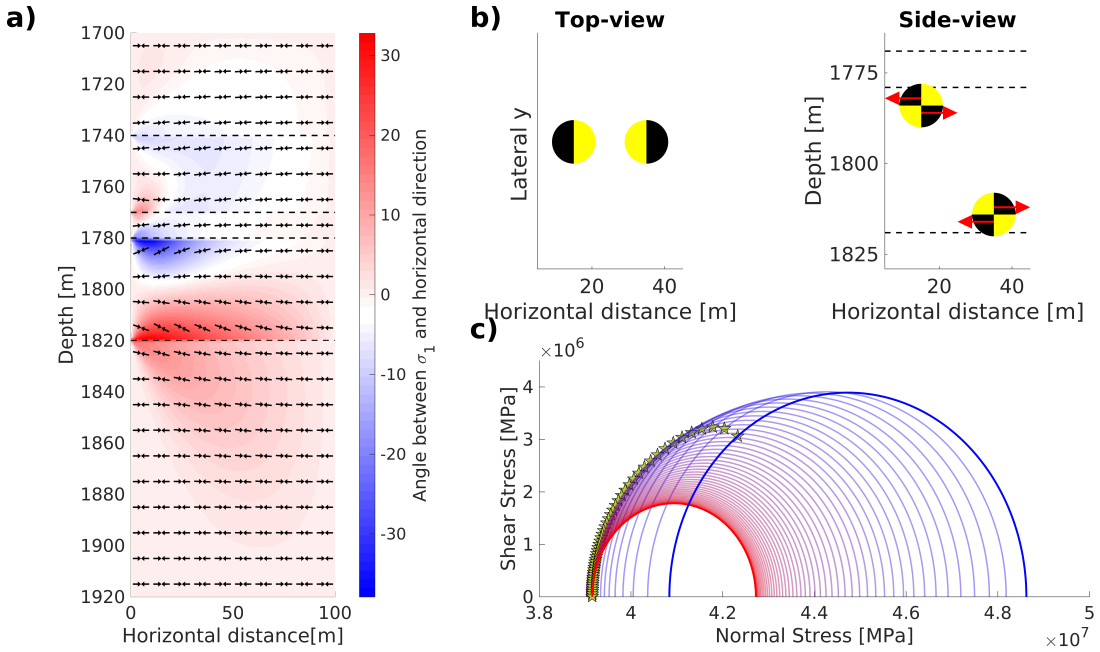

Figure 5.8: **a)** Angle between σ_1 and the horizontal direction for the SS model. Black arrows show the orientation of σ_{max} for each location inside the model. **b)** Sketch showing that parts of the model where half-moon mechanisms are probable and red arrows indicate slip orientation. **c)** Mohr-Coulomb circles for a horizontal profile at a depth of 1818 m, close to the layer interface in the area of rotated stress. Green stars at each Mohr-Coulomb circle show the pairs of coordinates (normal stress, shear stress) for a horizontal faulting plane (criticality of horizontal cracks). In the vicinity of the fracture, these are closest to the failure line, i.e. horizontal cracks are most critical. The blue circle corresponds to a location close to the fracture, the red circle to a location at the right model boundary.

5.4.4 Model II

Figure 5.9 shows the stress distribution for the second model. In the vicinity of the fracture, the horizontal compressional stresses (σ_{xx}) are equal to the injection pressure (45 MPa). At a greater distance to the fracture, they are equal to the minimum horizontal stress σ_h. At the vertical limits of the fracture significantly smaller horizontal stresses are observed. The vertical compressional stress (σ_{zz}) is in most parts of the model equal to the tectonic stress σ_v= 50MPa. Only in the vicinity of the fracture variations are observed. The most interesting observation is the distribution of shear stresses. At the fracture tips, significant shear stresses (several MPa) are created. These shear stresses have opposed signs/directions on both sides of the fracture and at the top and bottom of the fracture. A similar shear stress distribution at the tips of hydraulic fractures has been found by Warpinski *et al.* [2004] using an analytic solution of a similar problem. Similarly to the analysis of model I, I plot the local stress distribution and orientation of the maximum principal stress. In order to directly compare the results for models II and III, I present the angle between the maximum principal stress and vertical direction for both models together (Figure 5.11) after showing the stress distribution for model III. At the fracture tips, the maximum principal stress deviates significantly from the initially vertical orientation. As the shear stresses have opposed orientations on both sides of the fracture, also the maximum principal stress shows opposed tilts from vertical orientation. Similarly to model I (Figures 5.7 and 5.8), I plot Mohr-Coulomb circles for the vicinity of the fracture tip to analyze the stability of vertical cracks (Figure 5.12). In the far-field of the fracture, the directions of tectonic stresses (σ_v,σ_h) are dominant (blue circle).

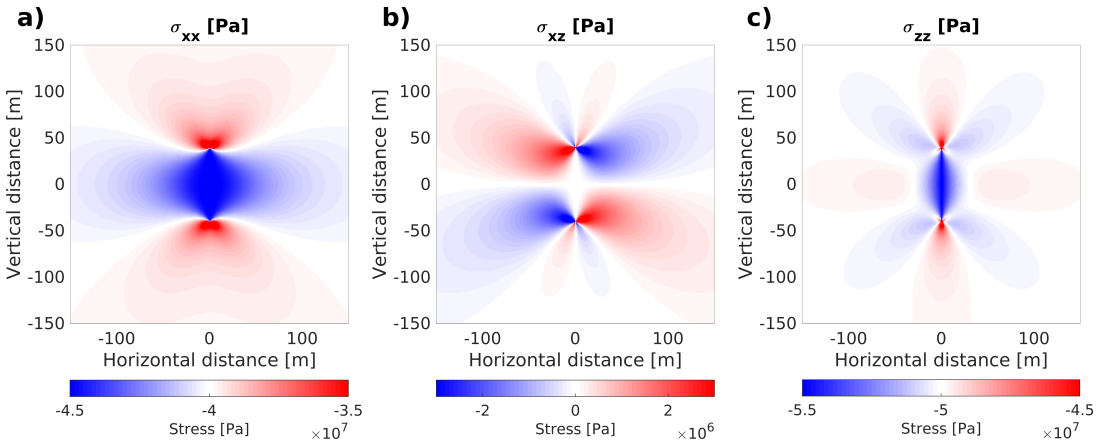

Figure 5.9: Stress distribution for model II, **a)** horizontal compressional stresses, **b)** shear stresses and **c)** vertical compressional stresses. Horizontal and vertical distances are measured from the center of the fracture.

The maximum and minimum principal stresses coincide with the vertical and minimum horizontal stress. The angle between a vertical crack and the maximum principal stress (indicated by the green star) is zero. In the vicinity of the fracture, the radii of the Mohr-Coulomb circles are larger and circles are slightly shifted toward the origin, i.e. areas close to the fracture tip are more critical (see red circle). Due to the local stress field rotation, the angle between σ_1 and vertical direction increases and vertical cracks have an increased criticality and are almost ideally oriented to fail first. Here, half-moon events are highly probable.

5.4.5 Results - Model III

In the final model (model III), both effects that create shear stresses in the fracture vicinity are observable (Figure 5.10). As expected from model I, we observe shear stresses at layer interfaces. Since the central layer is relatively thin (20 m), the spatial extent of the domain with non-vanishing shear stresses inside the model is small. As expected from model II, we additionally observe shear stresses at the fracture tips. Their spatial extent, especially in vertical direction is smaller compared to model II, since both effects superimpose each other. Both effects create local stress field rotations (Figure 5.11b). Although the impact of layering is smaller, both effects are significant and can explain the occurrence of half-moon events.

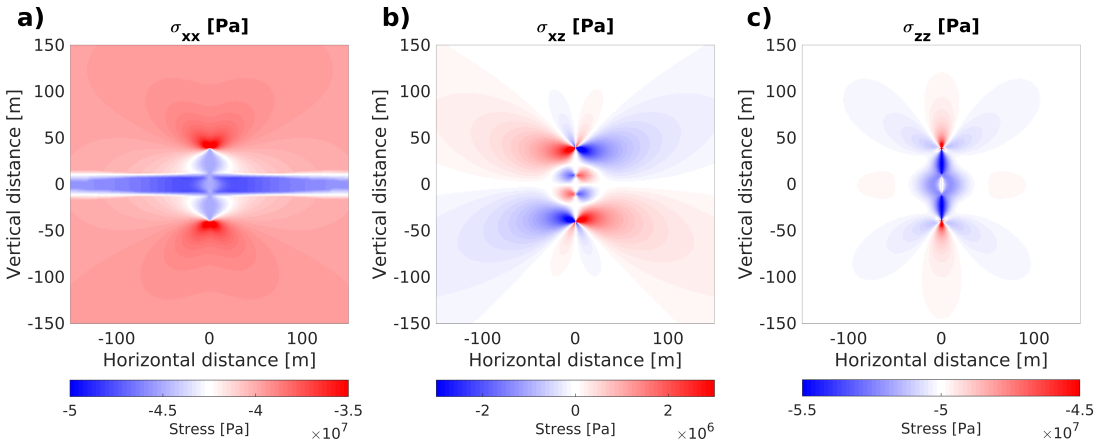

Figure 5.10: Stress distribution for model III, **a)** Horizontal compressional stresses, **b)** Shear stresses and **c)** vertical compressional stresses. Horizontal and vertical distances are measured from the center of the fracture.

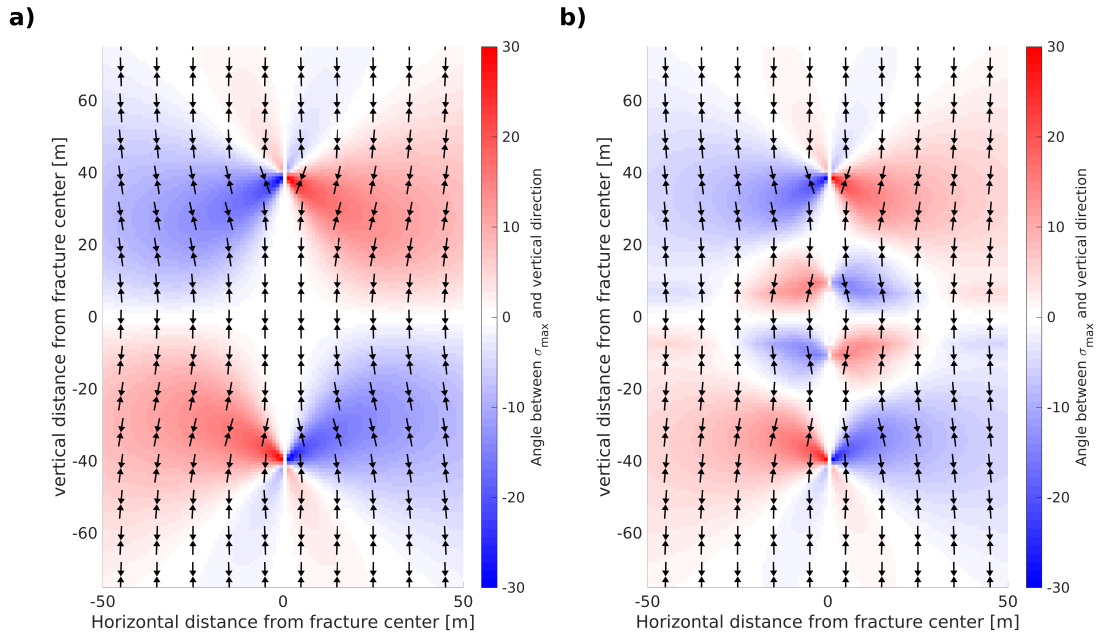

Figure 5.11: Local orientation of the maximum principal stress for **a)** model II and **b)** model III. Both models show a significant rotation of the maximum principal stress close to the fracture tips. Model III additionally shows stress field rotations at layer interfaces.

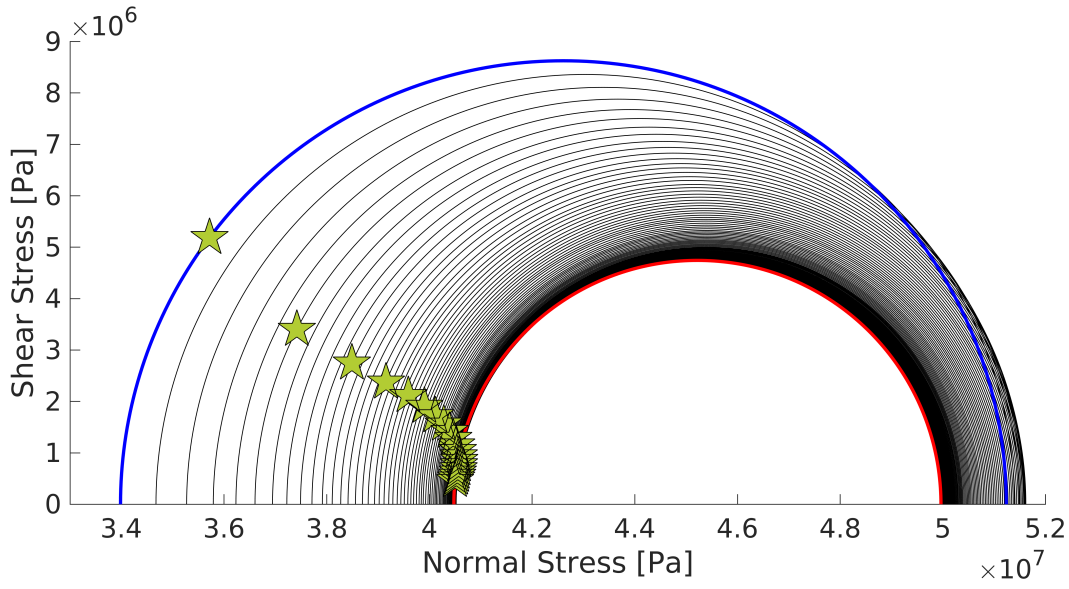

Figure 5.12: Mohr-Coulomb circles for a horizontal profile close to the fracture tip (model II). The blue circle corresponds to a location close to the fracture, the red circle is in the far field of the fracture.

5.4.6 Tip Effects Under Strike-Slip Conditions

The second and third model can not be adapted for the strike-slip case. The vertical plane that we consider in Figure 5.4, is in the strike-slip case the σ_2-σ_3-plane. Thus, this plane cannot be used to investigate rotations of the maximum principal stress. The σ_1-σ_3-plane for the SS-case is horizontal. If we considered this plane, we might observe horizontal rotations of the maximum principal stress around the fracture, however, this cannot cause half-moon events. As discussed before, the maximum principal stress needs a certain deviation from the horizontal direction to create half-moon events. Thus, a simplification of the strike-slip case for models II and III does not contribute to clarify tip-domain conditions for half-moon events. This requires more detailed modeling in 3D, which I present in Chapter 6.

5.4.7 Hydraulic Fracturing in Thrust Faulting Environments

As shown above, one possible source of local stress field rotations are rapidly changing elastic parameters between layers of varying lithology. In the case of an ambient thrust faulting environment, the hydraulic fracture would ideally propagate in the horizontal plane. When assuming a horizontal sedimentary layering, the fracture would not cross any layer interfaces and hence not create any stress field rotation. Thus, half-moon events cannot be caused by layering under these conditions. Stress field rotations at the tips of a horizontal fracture, however, might occur. Because hydraulic fracturing in thrust conditions and the observation of horizontal fractures is very seldom, I do not consider this case here.

5.5 Summary of 2D Geomechanical Modeling

Due to hydraulic stimulation, stress conditions in the vicinity of a hydraulic fracture are significantly changed. Next to the body of the hydraulic fracture, the horizontal stress which initially varies from layer to layer is changed to the fluid pressure inside the hydraulic fracture. This stress change can cause local rotations of the principal stresses close to the hydraulic fracture. To observe such a rotation, close values of horizontal and vertical stresses and significant shear stresses are required. In such stress regimes, half-moon events are highly probable. The first domains where these conditions are commonly created are close to interfaces between different sedimentary rock layers with different lithologies and elastic parameters. The spatial extent of regions of rotated stress orientation is controlled by the layer thickness and the variations of the elastic parameters between layers. Hydraulic fracturing under normal faulting tectonics can create half-moon events with slip on a vertical fault plane. If hydraulic fracturing is performed under strike-slip conditions with high injection pressures, this can lead to half-moon faulting along the horizontal plane.
The second region, where stress field rotations occur, is located at the fracture tips. Here, shear stresses are created by the finite body and surface of the hydraulic fracture itself. The presented models can explain several features that are observed in the field, see section 5.1.3. Half-moon events are located in certain depths (i.e. near layer interfaces (model I) or at the fracture tips (model II)) and show opposed shear senses in different depths and on opposite sides of the fracture. Although the simple 2D models can explain most of the field observations, several key aspects cannot be captured by the 2D model, for instance, hydraulic fracturing under strike-slip conditions, where the injection pressure is smaller than σ_1. For this, a 3D modeling approach is required that I consider in the following chapter.

CHAPTER 6

A 3D GEOMECHANICAL MODEL FOR HYDRAULIC FRACTURING

The numerical modeling in the previous chapter offered insights into what conditions are needed for half-moon events and how these are created during the hydraulic stimulation. Although I used 2D cross-sections as a simplification, several observations from the field (see section 5.1.3) can be explained by the numerical model. This includes (1) a general explanation for the occurrence of half-moon events, (2) their location at narrow depth intervals and (3) opposed slip orientations on opposed sides and at the upper and lower limit of the hydraulic fracture. Thus, the 2D model is a justifiable approach to model hydraulic fracturing in normal faulting tectonics. However, it can be applied to strike-slip tectonics only for the very special (and rather unusual) case, where the injection pressure p_{inj} is higher than σ_1. Additionally, the observation of the horizontal rotation of the vertical plane (see point 4 in section 5.1.3) is still insufficiently answered.

Here, I extend the numerical modeling to the full 3D space. Thereby, I can model hydraulic fracturing in strike-slip domains for arbitrary stress distributions and can additionally account for effects that occur at the horizontal tips of the fracture. The 3D model can be also used to check if the assumption of 2D cross-sections in the previous chapter was justified by analyzing slices through the 3D medium that are equivalent to the modeling plane in the previous chapter. Previously, I showed that half-moon events are likely to occur at interfaces between layers of different stiffnesses that are crossed by the fracture or at the complex stress field at the tip of the hydraulic fracture. Although both effects are significant, my models show that tip effects seem to be more important. Thus, I consider in this chapter only stress field rotations at the tips of a hydraulic fracture, caused by its ellipsoidal shape. Finally, I compare the modeling results to the case study from Horn-River-Basin (Chapter 4).

6.1 3D Geomechanical Theory

6.1.1 3D Stress Tensor

In the previous chapter, I used a submatrix of the full 3D stress tensor to analyze stress rotations in 2D. Here, I introduce the full 3D stress tensor and show how to obtain the orientation and magnitude of the principal stresses. Besides, I extend the concept of Mohr-Coulomb diagrams to 3D media.
The three-dimensional stress tensor is a symmetric tensor that can be written as (see e.g. Shapiro [2015]):

$$\sigma_{ij} = \begin{pmatrix} \sigma_{xx} & \sigma_{xy} & \sigma_{xz} \\ \sigma_{yx} & \sigma_{yy} & \sigma_{yz} \\ \sigma_{zx} & \sigma_{zy} & \sigma_{zz} \end{pmatrix}, \tag{6.1}$$

where the diagonal elements are the compressional stresses and the non-diagonal elements are the shear stresses.
This tensor can be decomposed into its eigenvalues and eigenvectors that correspond to the size and direction of the principal stresses, respectively. Correspondingly to the notation in Chapter 5, I denote here the magnitudes of the principal stresses by σ_1, σ_2 and σ_3 and their directions by $\bar{p}_1$, $\bar{p}_2$ and $\bar{p}_3$. The principal stresses are perpendicular to each other. As shown in Chapter 5, half-moon events require local rotations of the stress field, i.e. a deviation of the maximum principal stress from horizontal/vertical direction. For the 2D case, it is possible to compute the orientation of the principal stresses and their magnitude analytically (Chapter 5). For an arbitrary 3D stress tensor this analytical computation is not possible and the orientation and magnitude of the principal stresses are calculated numerically.

6.1.2 Orientation of the Maximum Principal Stress

As explained above, each principal stress can be expressed by its magnitude σ_i which is equal to the corresponding eigenvalue of the stress tensor and by its orientation which is equal to the corresponding eigenvector, $\bar{p}_i$, of the stress tensor.
In contrast to the previous chapter, I do not only consider the angle between the corresponding stress and vertical direction but additionally its horizontal orientation. Thus, I express the direction of each principal stress in terms of two angles, ξ and φ. ξ_i describes the deviation of $\bar{p}_i$ from vertical direction and φ_i its horizontal orientation where an angle of zero means an orientation in the y-direction.

Both angles can be computed as follows:

$$\xi_i = arctan\left(\frac{p_{iz}}{\sqrt{p_{ix}^2 + p_{iy}^2}}\right) \tag{6.2}$$

$$\varphi_i = arctan\left(\frac{p_{ix}}{p_{iy}}\right), \tag{6.3}$$

where p_{ix}, p_{iy} and p_{iz} denote the x- ,y- and z-component of the direction of the i-th principal stress.
In principle, one can compute the orientation of any of the three principal stresses, however, for stability analysis of natural faults using the Mohr-Coulomb failure criterion, only the orientation of the maximum principal stress is necessary. Thus, I neglect the index i in the following and ξ and φ denote the respective angles for the maximum principal stress.
If the size and the orientation of the maximum principal stress are known, we can analyze the stability of preexisting natural cracks. This analysis is typically done using the Mohr-Coulomb failure criterion. In contrast to Chapter 5, where I described the stress state only by a single Mohr-Circle (defined by σ_1 and σ_2), the stress in the medium is here described by three Mohr-Circles (σ_1-σ_2,σ_1-σ_3, and σ_2-σ_3).
The Mohr-circle with the largest radius (defined by σ_1,σ_3) and the angle ξ are then used for stability analysis. For completeness, I plot all three circles in sections 6.3.1 and 6.3.2.

6.2 3D Geomechanical Modeling

I perform the numerical modeling in 3D using an ellipsoidal hydraulic fracture in a homogeneous isotropic medium (Figure 6.1). Additionally, I apply the boundary conditions in Table 6.1 to solve for the full stress tensor for each location inside the medium. Normal to the surface of the ellipsoidal fracture, I apply a pressure that is equal to the fluid pressure inside the hydraulic fracture (p_{frac}). The conditions at the outer model limits are chosen according to the tectonic setting (Table 6.1). The tectonic stresses are chosen such that the maximum and intermediate principal stress are quite close and significantly larger than the minimum principal stress (Table 6.1). This characteristic was also found by Zoback & Snee [2018] and [Kuang *et al.*, 2017] in field observations. The chosen injection pressure is relatively high (higher than σ_2) which is consistent with the field data example from Horn-River-Basin in Chapter 4 [Hummel & Shapiro, 2013].

For the modeling, the same assumptions as in Chapter 5 on the shape of the fracture and the pressure distribution are made. This includes a perfect ellipsoidal shape of the fracture and a uniform pressure distribution within the fracture. I justify these assumptions with the same arguments as in section 5.3.4.

	$\sigma_{xx} = \sigma_H$	$\sigma_{yy} = \sigma_h$	$\sigma_{zz} = \sigma_V$	p_{inj}
Normal-Faulting	45 MPa	30 MPa	50 MPa	47.5 MPa
Strike-Slip	50 MPa	30 MPa	45 MPa	47.5 MPa

Table 6.1: Boundary conditions for the two models.

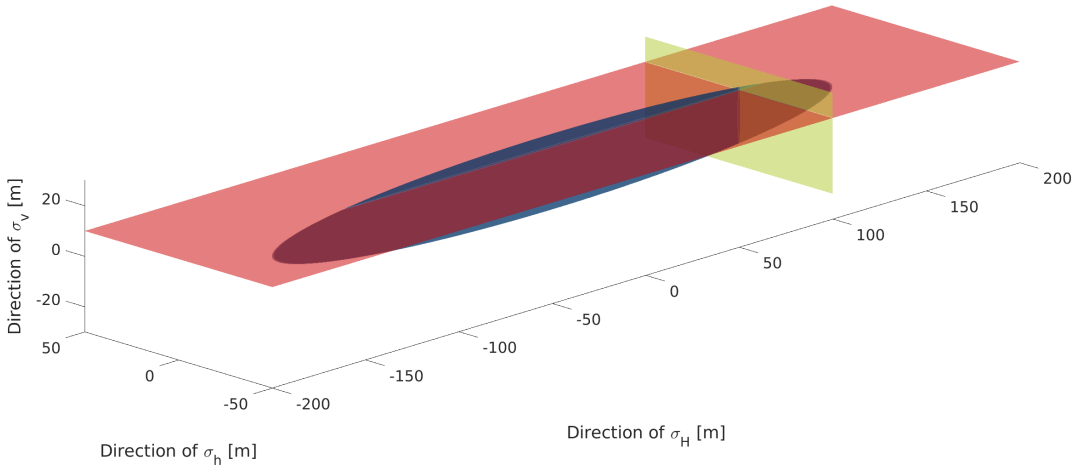

Figure 6.1: Geometry of the numerical model. The hydraulic fracture is modeled as an ellipsoid (blue) with a height of 30 m, a length of 300 m and a thickness of 0.01 m in σ_h direction. The surrounding rock mass is modeled as a homogeneous isotropic medium ($V_p = 3500 \frac{m}{s}$, $V_s = 2021 \frac{m}{s}$ $\rho = 2500 \frac{kg}{m^3}$). The 3D stress distribution is analyzed in two perpendicular planes (red and green) that are parallel to the coordinate axes.

6.3 Results of 3D Modeling

The numerical modeling is again performed with the COMSOL-Multiphysics software [COMSOL-Multiphysics®, V 5.4]. As a result of the computation, I obtain the full 3D stress tensor for every location inside the model. For simplification, I evaluate the stress distribution in two planes close to the fracture tips that are perpendicular to the coordinate axes, shown in Figure 6.1.

Figures 6.2 and 6.3 show the spatial distribution of all six components of the stress tensor inside the model. The compressional stresses are shown in Figures a, c and e, the shear stresses in Figures b, d and f. In most parts of the model, the compressional stresses are equal to the tectonic stress conditions (indicated by greenish color, see also Table 6.1). Only close to the fracture wall, all three components show significantly higher stresses. Normal to the horizontal tips of the fracture very thin volumes are created, where the compressional stresses are significantly reduced. Close to the hydraulic fracture also significant shear stresses are created. Here, σ_{yz} exhibits values of several MPa along the whole fracture wall, whereas σ_{xy} and σ_{xz} are smaller (less than 1MPa). The vertical cross-section (Figure 6.3) equals the 2D plane that I considered in Chapter 5 and exhibits a very similar stress distribution as the 2D model.

In the following, I analyze the results for the normal-faulting and the strike-slip model independently. For this, I compute the orientation of the maximum principal stress and the corresponding orientation angle ξ and φ.

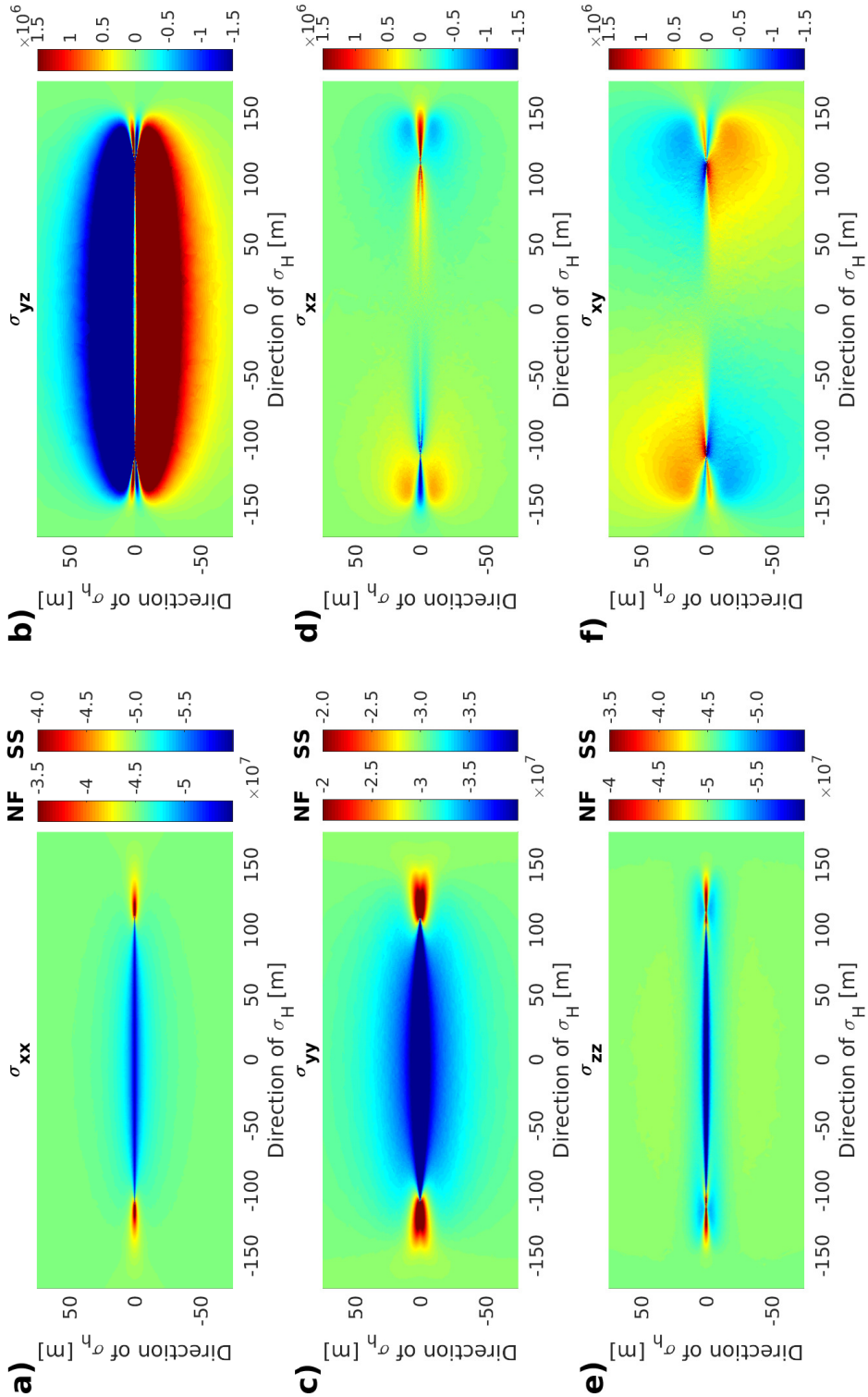

Figure 6.2: Spatial distribution of the six components of the stress tensor for a horizontal slice through the model (red plane in Figure 6.1). The left colorbar next to each subplot corresponds to the stresses for the normal faulting model boundary conditions, the right colorbar to the strike-slip conditions. The shear stress distribution is identical for both models.

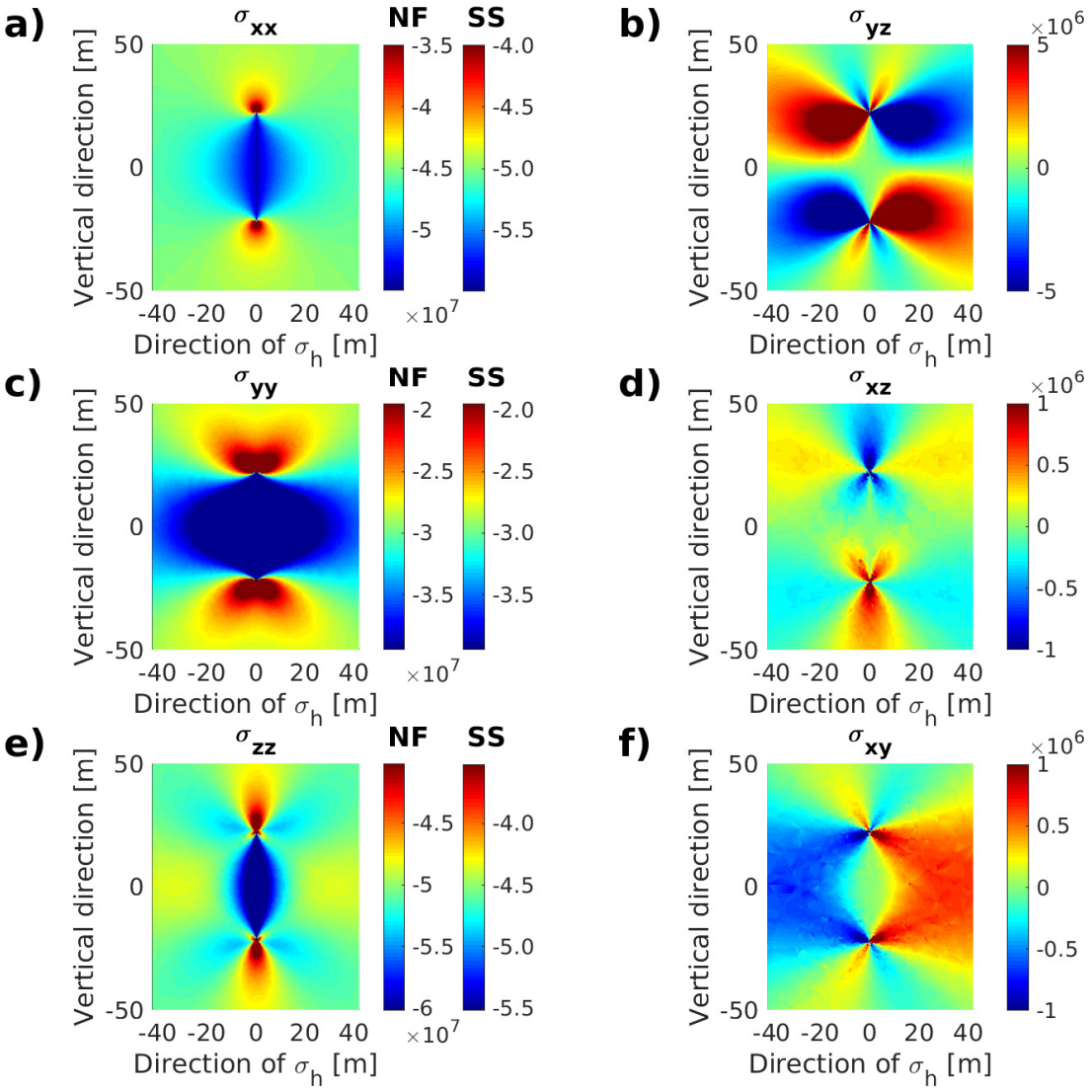

Figure 6.3: Spatial distribution of the six components of the stress tensor for a vertical slice through the model (green plane in Figure 6.1). The left colorbar next to each subplot corresponds to the stresses for the normal faulting model boundary conditions, the right colorbar to the strike-slip conditions. The shear stress distribution is identical for both models.

6.3.1 Modeling Results - Normal Faulting Model

Figure 6.4 shows the local orientation of the maximum principal stress for the two planes. Figures 6.4a and 6.4b show the spatial distribution of the angle ξ inside the model, Figures 6.4c and 6.4d the distribution of φ.
Since the maximum tectonic stress is vertical, the angle ξ is close to 90° in most parts of the model. Only close to the fracture itself, the maximum principal stress is significantly tilted and perpendicular to the fracture surface. Two domains of rotated stress can be observed. The first domain ranges over the whole surface next to the wall of the hydraulic fracture. Here we observe angles ξ of approximately 60°. The second area of tilted stress is located close to the fracture tips. Here we observe a very thin area of rotated stress that is aligned with the orientation of the fracture itself. Correspondingly, the angle φ exhibits values of 180° (positive σ_h direction) and 0° (negative σ_h direction) next to the fracture wall. Close to the fracture tip, the angle φ changes very locally to an angle of 0° or 180°, respectively, which corresponds to an orientation that is aligned with the hydraulic fracture or σ_H-direction. Under this condition, we expect half-moon events with slip on the vertical fault plane next to the entire hydraulic fracture (later called location I). As indicated by Figure 6.4c we observe opposed slip orientations on both sides of the fracture which is also schematically shown in Figure 6.8.

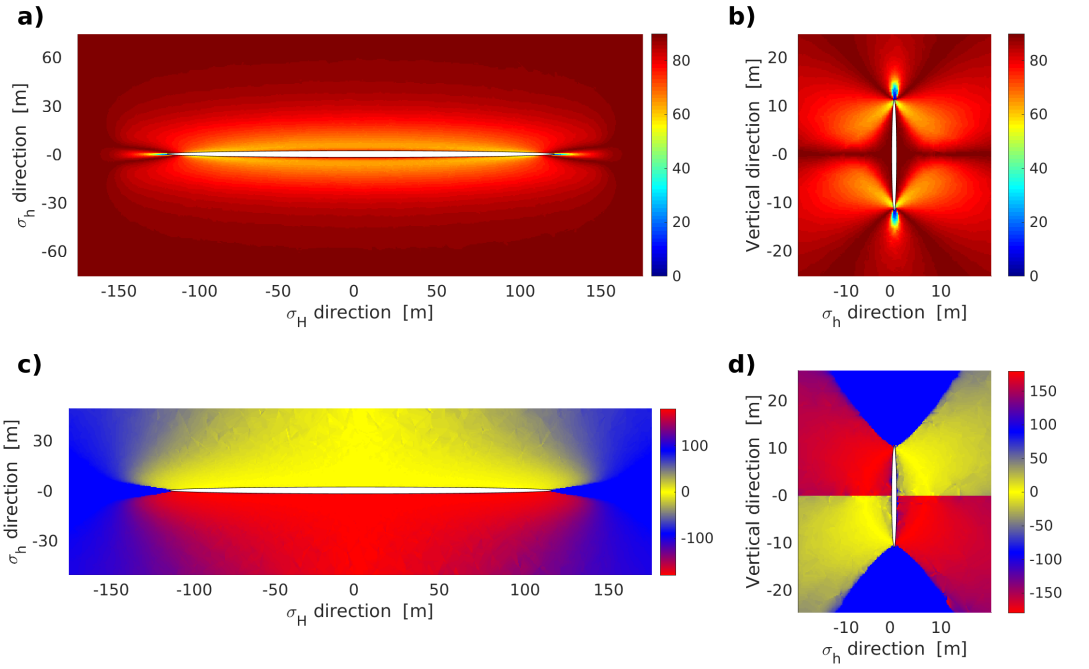

Figure 6.4: Orientation of the maximum principal stress for the NF model for the two observation planes (see Figure 6.1). **a)** and **b)** show the spatial distribution of angles ξ and **c)** and **d)** the distribution of φ.

Additionally, we might observe half-moon events at the fracture tip with vertical slip and a fault orientation normal to the hydraulic fracture (location II). As the area of rotated stress is extremely thin, it is questionable if such events are triggered in reality or if this is just a characteristic of the numerical model, see also discussion the section on model assumptions.
In addition to the local stress orientation, the magnitude of the principal stresses can be used to evaluate the local stability of preexisting cracks. For this, I use the Mohr-circle representation. Figure 6.5a shows Mohr circles for location I and 6.5b for location II. The red star in each plot shows the criticality of vertical cracks. The dashed lines in both plots correspond to the tectonic stress regime and can be considered as the (stable) natural stress state before the hydraulic fracture was created (see also values in Table 6.1). For this tectonic situation, the angle between a vertical crack and σ_1 is zero, since σ_1 is vertical and thus vertical cracks have a low criticality. The non-dashed lines correspond to the stress state for locations I and II. At location I, σ_1 is significantly increased, σ_3 decreased and σ_2 in approximately the same range as previously. This leads to larger radii of the Mohr-Coulomb circles, i.e. an increased criticality. The red star again marks the angle between the maximum principal stress and a vertical crack. At this location, a vertical crack is almost ideally oriented. Both, the increase of the radii (i.e. increased instability) and the orientation of the stress field can explain half-moon events at this location. At location II (Figure 6.5b), the relative difference between the principal stresses is comparable to the tectonic case, but all exhibit significant smaller absolute values. Also at this location, ideal conditions (magnitude and orientation of σ_1) for half-moon events on a vertical fault plane are created.

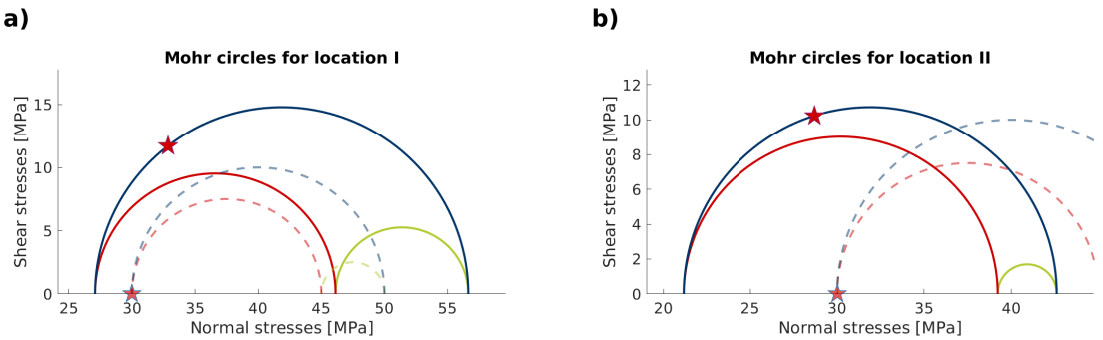

Figure 6.5: Mohr circles for **a)** a location next to the fracture wall and **b)** close to the fracture tip. The red star shows the criticality of a vertical fault plane. At both locations vertical fault planes are oriented almost ideally to fail as half-moon events. Furthermore, both locations are significantly more stressed than under tectonic conditions, see dashed lines.

6.3.2 Modeling Results - Strike-Slip Model

Similarly to the normal faulting model, I plot the orientation of the maximum principal stress for the two observation planes for the strike-slip boundary conditions in Figure 6.6.

Here, the maximum tectonic stress is horizontal (in both figures parallel to the x-axis) and thus the maximum principal stress is in most parts identical and parallel to it, as shown by dark blueish colors that correspond to an angle close to 0° in Figure 6.6a and 6.6b and bluish colors that correspond to angles close to ± 90° in Figure 6.6c and 6.6d. Only close to the tip of the hydraulic fracture we observe significant local rotations of the maximum principal stress. At the tips, the maximum principal stress rotates within a small area and shows significant vertical components up to an orientation close to vertical, i.e. ξ close to 90°. Additionally, the maximum principal stress also rotates in horizontal direction and is perpendicular to the fracture in the vicinity of the fracture tip (Figures 6.6c and 6.6d). Here, φ is either close to zero or 180° which can explain opposed slip directions on different sides of the fracture. We additionally observe opposed stress rotations at the top and bottom of the fracture.

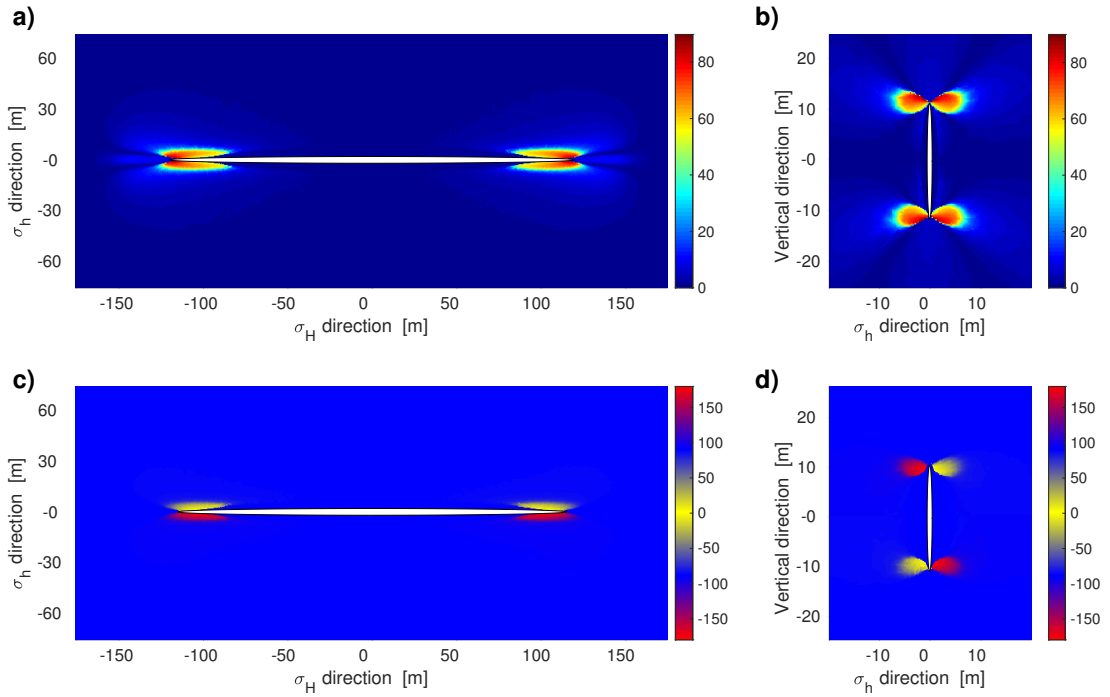

Figure 6.6: Orientation of the maximum principal stress for the strike-slip model for the two observation planes (see Figure 6.1). **a)** and **b)** show the spatial distribution of angles ξ and **c)** and **d)** the distribution of φ.

As previously done for the normal faulting model, I evaluate the local stress state using Mohr-Coulomb circles. Again, the local stress field is significantly more critical (greater radii of the Mohr-circles and smaller normal stresses) than the tectonic situation. The red star shows the criticality of a vertical fracture. Due to the stress rotation, vertical fractures are locally optimally oriented to the local stress field, i.e. most critical, creating ideal conditions for half-moon events. In contrast to normal faulting, the volume of rotated stress is much smaller and restricted to the tips, and half-moon events are not expected to happen along the whole fracture wall in this case. Possible locations and slip orientations for half-moon events are again shown schematically in Figure 6.8.

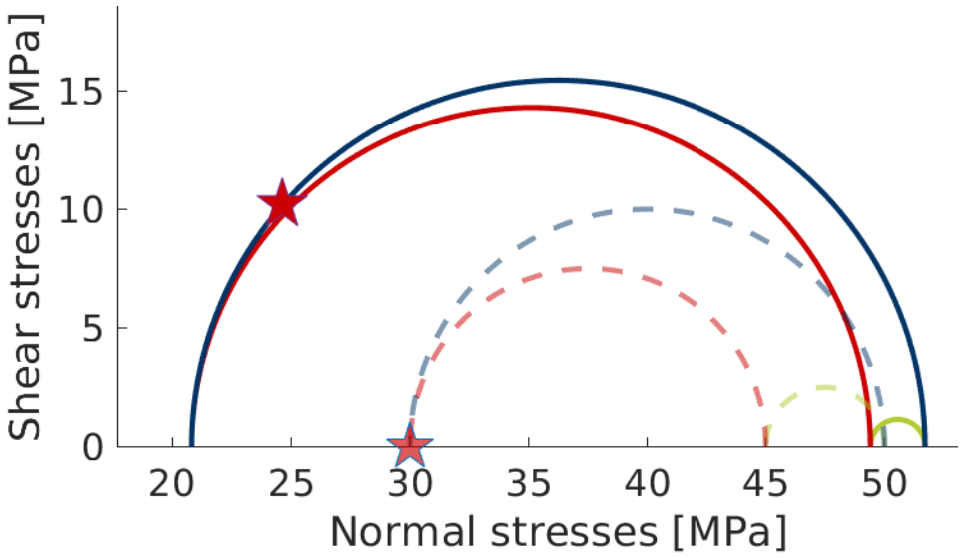

Figure 6.7: Mohr circles for the location of rotated stress close to the fracture tip (Figure 6.6). At this location the stress state is more critical than the tectonic (natural) stress state (dashed lines). The red star marks the criticality of a vertical natural fracture. The local stress field is almost ideally oriented to trigger a half-moon event at such a vertical fault plane.

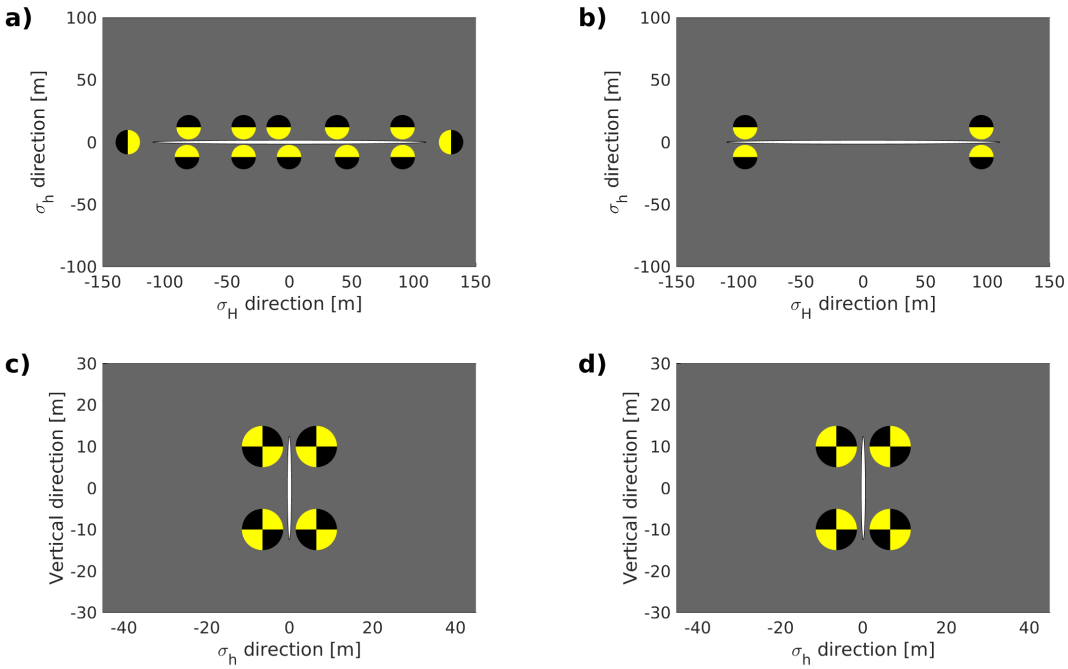

Figure 6.8: **a)** and **c)** Locations, where half-moon events are probable for the NF model (see also Figure 6.4), **b)** and **d)** same plot for the strike-slip model (see Figure 6.6). In NF, half-moon events are expected to occur horizontally along the complete fracture wall with fault planes parallel to the fracture itself and in a very thin domain at the fracture tips with fault planes normal to the fracture. In depth, event locations are restricted to the area around the vertical edges of the fracture. In strike-slip domains, half-moon events are only expected close to the fracture tip with fault planes parallel to the fracture. Similarly to NF, events should occur at narrow depth bands.

6.3.3 Comparison with Field Observations

I have shown that under both normal and strike-slip, conditions preferable conditions for half-moon events can be created. Having introduced the field data example in Chapter 4, I compare these results to the numerical model. As natural seismicity in Horn-River Basin mainly shows strike-slip faulting, I compare the results to the corresponding modeling results.

For early events, we observe the typical pattern of events with parallel fault planes to the fracture itself (see Figure 4.8). Events are located very close to the fracture. We hardly see opposed slip directions on opposite sides of the fracture (as expected from our model), almost all beachballs show compression in south-east direction. A possible explanation might be that this area has been weakened before (by previous fracturing stages) and thus this region is more critical and closer to failure.

Events at a greater distance to the injection point (around x=200m and y=-75m) do

not show the perfect parallelism of fracture and fault plane as expected, but fault plane orientations rotate from the initial orientation to almost north-south direction. Furthermore, events do not form a thin strip but occur in a wider range. This might be an indication for the evolution of a more complex fracture network that consists not only of a single fracture. In this case, the model assumption of a single planar fracture is no longer valid and I, therefore, concentrate in the following analysis on the early events. From the modeling, we expect half-moon events only at the tips of the hydraulic fracture. This means that with the increasing length of the fracture, half-moon events are not expected to occur close to the injection point. To check if this characteristic can be seen in the microseismic data, we consider the R-T-analysis [Shapiro *et al.*, 1999a] for our source in Figure 4.14a, where the distance from the injection point for each event is plotted as a function of time since the start of injection. Especially in the first 40 minutes we observe half-moon events that occur at increasing distances from the injection point with time. For each time, half-moon events occur only in a certain distance range, for instance for t=30 minutes events occur in the range of 150m to 200m, but not close to the injection point itself. This coincides quite well with the results from the numerical modeling in Figure 6.6, where half-moon events are only probable at the tip of the hydraulic fracture. After approximately 40 minutes of injection, we still observe the general trend of a propagating fracture with events at greater distances to the injection point. Additionally, we observe events at smaller distances from the injection point. This trend is also visible in the size of the gyration ellipsoid in Figure 4.14b. From this time on, we also observe a rotation of the vertical plane of the half-moon events. These two observations might be an indication of the development of a more complex fracture network. This might also explain why we observe events at smaller distances from the injection point.

Figure 4.14a also shows that the ratio between strike-slip events and half-moon events is high at the start of injection and decreases during the stimulation. A possible interpretation is that strike-slip events only require small perturbations in pore-pressure that build up quickly, whereas half-moon events require the opening and propagation of a hydraulic fracture of a certain length which takes several minutes.

In contrast to the half-moon events, strike-slip events exhibit a larger variability in the distance from the injection point, since they do not require the specific stress field that is only created at the fracture tips. They occur on faults that are naturally already close to critical failure and have been additionally weakened by the increased pore pressure due to the fracturing.

6.4 Summary and Outlook of 3D Geomechanical Modeling

As an addition to the geomechanical analysis in Chapter 5, I used a 3D numerical model, to analyze the geomechanical stress conditions that are necessary to create half-moon events and compared these results to field observations from Horn-River Basin.
As shown before, half-moon events require a significant deviation of the maximum principal stress from horizontal or vertical orientation. Locally close horizontal and vertical stress and significant shear stresses are needed. These conditions are fulfilled close to the tips of hydraulic fractures, where significant shear stresses are created due to the ellipsoidal surface of the fracture.
Half-moon events are probable in both normal-faulting and strike-slip regimes. In normal-faulting regimes, half-moon events can occur along the entire fracture wall on vertical fault planes that are parallel to the hydraulic fracture itself. Furthermore, they might occur in a very thin area beyond the tips of the fracture with fault planes oriented perpendicular to the fracture. Both regions exhibit principal stresses that are optimally oriented in respect to vertical cracks. The criticality of these cracks is increased, compared to the tectonic stress conditions. In strike-slip domains, half-moon events are only probable close to the tips of the hydraulic fracture. Comparably to normal faulting, half-moon events occur on vertical fault planes that are parallel to the hydraulic fracture. This is in contradiction to the results from Chapter 5, where the model showed a slip on the horizontal plane, however, this result was only valid for an injection pressure higher than σ_1. If I had used the assumption here, I would get a similar result.
Finally, I compared the modeling results to the field data from Horn-River-Basin and found several common characteristics. At the start of the treatment, mainly half-moon events which vertical fault planes that are aligned with the fracture wall are observed. The first 40 minutes of injection are well approximated by the numerical model. With the propagation of the fracture, events also show greater distance to the injection point which coincides with my model that only explains half-moon events around the fracture tips. For times beyond 40 minutes, the fracture network seems to become more complex and cannot be explained by the simple model with a single fracture. The interpretation of the more complex fracture network is supported by (1) the change in fault plane orientation of half-moon events, (2) the size of the gyration ellipsoid and (3) RT-analysis in Figure 4.14.
Although main field observations are explained by the model, some questions are still unanswered and object of further research. This includes (1) the comparison of the numerical model to NF case studies, (2) the influence of anisotropy on the stress distribution and (3) the influence of the interaction of multiple hydraulic fractures on the stress field.

CHAPTER 7

CONCLUSIONS AND OUTLOOK

The injection of fluids into the subsurface perturbs the initial stress state and has the potential to trigger earthquakes. These earthquakes occur on preexisting, already critically stressed, natural faults that fail due to changes in stress and/or pore pressure caused by the operations. The observation and analysis of these earthquakes over the past decades have broadened the knowledge of the triggering mechanisms and initiated ways to mitigate the seismogenic risk. This thesis aims to contribute to the understanding of fluid-induced seismicity by providing advanced techniques to model earthquake mechanisms. In particular, I address the effect of anisotropy on the radiation patterns of earthquakes (Chapter 2). I provide a new tool to analyze the faulting orientations of double-couple earthquakes (Chapter 3) and explain with a geomechanical modeling (Chapters 5 and 6) the occurrence of half-moon events, a seismic source mechanism typical for hydraulic fracturing. The technical tools are applied to a microseismic dataset (Chapter 4). The joint analysis of microseismic data and geomechanical modeling leads to a better understanding of the physics of the mechanisms that trigger microseismicity induced by hydraulic fracturing.

Following the introduction (Chapter 1), I illustrate in Chapter 2 the frequently overlooked difference between potency and moment tensors using synthetic examples. The potency tensor, a quantity proportional to the strain in the source, is a purely geometrical description of the orientation of earthquake faulting. The moment tensor, proportional to the stresses created by such an earthquake is, in the case of double-couple faulting in isotropic media, a re-scaled version of the potency tensor, but can be significantly influenced by the properties of the faulting medium if the medium is anisotropic or the faulting not purely double-couple. I illustrate this effect by analyzing radiation patterns and their non-DC components of double-couple faulting in several anisotropic media. In particular, I analyze the influence of the degree of anisotropy and the orientation of the fault plane with respect to the symmetry axis. Furthermore, my findings suggest to analyze potency tensors of microseismic events rather than moment

tensors. For this, I introduce a graphical visualization of this potency tensor by using the potency tensor isotropic (PTI) equivalent.
Because most sources are predominately double-couple, a further decomposition and visualization addressing the source geometry of double-couple sources can be a useful tool to analyze multiple source mechanisms at once. Such decompositions already exist using projections of different angles of the principal components of the moment tensor into ternary diagrams. Due to the different projections, source mechanisms are not uniformly distributed in the ternary diagrams, but they exhibit distortion. Thus, I propose a new decomposition that divides an arbitrary double-couple tensor into fractions of strike-slip, normal, thrust and half-moon faulting. With this decomposition, each DC tensor can be described by just two independent parameters and the visualization with a diamond plot shows no distortion, and source mechanisms are uniformly distributed in the diamond. The decomposition can be used for any type of seismicity but is especially useful to analyze events induced by hydraulic fracturing, as it comprises half-moon faulting, which is a typical source mechanism for HF.

The theoretical tools from the first two chapters are used in the third chapter to invert and analyze source mechanisms of microseismic events induced by hydraulic fracturing in Horn-River Basin, Canada. I present a general inversion scheme, using the theoretical knowledge from Chapter 2 that can be used for source inversion in anisotropic media and invert for source mechanisms (potency and moment tensors) of more than 100 microseismic events. To analyze the main types of faulting, I apply the decomposition from Chapter 3 and find that a majority of events indicate half-moon faulting accompanied by several strike-slip events. Additionally, I analyze the non-DC components induced by the anisotropy and highlight that the general influence is small because the degree of anisotropy of the source layers is small and fault planes are close to parallel to the symmetry axis of the medium. Therefore, the subsequent discussion cannot answer the question conclusively whether a source inversion incorporating the effect of anisotropy provides better results than an isotropic inversion.

Half-moon events, as the typical mechanism for hydraulic fracturing, are not only found in the presented study but are frequently discussed in the literature. Half-moon events are rarely observed in natural seismicity, because they require special stress conditions, for example, tilted principal stresses. As they are recurrently observed at multiple HF sites, they seem to be directly fracturing-related, although the physics of these events has up to now not been well understood and the available models cannot account for all observations from the field. I present a 2D numerical finite element model that explains local rotations of the stress field, needed for half-moon events, at layer interfaces and close to the tips of the hydraulic fracture. This model, although it is quite simple,

can explain most observations from the field, including the occurrence of half-moon events at distinct depth and opposed slip orientations on different sites of the fracture as well as in depth.

Modeling hydraulic fracturing under general strike-slip conditions is not feasible using a 2D model. To compare the numerical modeling to the Horn-River case study, I thus further investigate the stresses created by an ellipsoidal fracture using a 3D approach. For simplicity, I limit the modeling to a homogeneous isotropic medium to only analyze stress rotations at the fracture tips. For hydraulic fracturing under normal faulting tectonics, the 3D model reproduces accurately the results from the 2D model and additionally indicates a possible occurrence of half-moon events at the horizontal tips of the hydraulic fracture with a vertical fault plane oriented normal to the HF. The model results for strike-slip tectonics show that half-moon events are only probable at the fracture tip, with vertical fault planes oriented parallel to the HF. This model can explain accurately the observations from the Horn-River data example for the early phase of stimulation. With the propagation of the hydraulic fracture, half-moon events also propagate away from the injection point. After 40 minutes of stimulation, the distribution of event locations and mechanisms shows a larger variety, which I interpret as the development of a more complex fracture network, which cannot be captured by the numerical model.

In summary, the presented thesis provides two new tools for the advanced processing of microseismic data that can be applied to any microseismic dataset. The presented case study confirms the frequent observation of half-moon events induced by hydraulic fracturing and the subsequent numerical modeling provides the first principle explanation that can explain the field observations. Therewith, it provides a significant contribution to the understanding of the physics of hydraulic rock stimulation.

Outlook

The numerical modeling in the final chapters of this thesis showed different characteristics of half-moon events under normal faulting and strike-slip conditions, although half-moon events are possible in both tectonic regimes. The characteristics for strike-slip conditions were validated by the field data example from Horn-River Basin. If I would have a hydraulic fracturing dataset from a region with normal faulting tectonics, it would be interesting to see if the distinctive features of the numerical modeling can be observed also in such data. For instance, it could be verified, if events with fault planes normal to the hydraulic fracture at the horizontal tips of the fracture really exist or if these are just a feature of the numerical model.

The representation of the rock for the numerical model in Chapter 6 was chosen to be the most simple, a homogeneous isotropic medium. As discussed before, hydraulic fracturing is typically performed in shales that are characterized by a significant degree of anisotropy. This anisotropy can have an additional impact on the stress distribution and therewith on local stress field rotations. Future numerical modeling would specifically account for this effect. Another simplification was the usage of a single ellipsoidal hydraulic fracture. Nowadays, hydraulic fracturing is commonly performed using a procedure called zipper-frac, where multiple hydraulic fractures are created subsequently or even simultaneously in neighbored boreholes. The interactions of these fractures and their influence on the stresses in the rock will be a question of future research.

In the past years, the traditional downhole microseismic monitoring with 3C geophones has been expanded by the application of distributed acoustic sensing (DAS) using fiber optic cables. These fiber optic cables are installed in boreholes close to the operations and measure the strain in the surrounding rock. Thereby, they can be used likewise as geophones to detect microseismic events (using the high-frequency emission of the deformation) and additionally to monitor the slow strain, i.e. the part of rock deformation that is related to the opening and propagation of the hydraulic fracture. Such data would provide a unique opportunity to compare the growth of hydraulic fractures in nature to the numerical modeling, to calibrate numerical models and to further understand the influence of rock properties, pumping pressure, pumping volumes, etc. on the fracture growth. In contrast to downhole geophones that can be considered as several 'point measurements' in a borehole, DAS cables are typically installed in the horizontal and vertical part of a borehole and thereby monitor a larger part of the focal sphere of an earthquake. Such data can be potentially used to invert for full moment tensors to further investigate the influence of anisotropy on the radiation pattern.

BIBLIOGRAPHY

AKI, K. & RICHARDS, P.G. (2002). *Quantitative Seismology*. University Science Books.

BAIG, A. & URBANCIC, T. (2010). Microseismic moment tensors: A path to understanding frac growth. *The Leading Edge*, 320–324.

BOITZ, N. (2016). *Seismic source mechanisms in anisotropic media - construction and inversion*. Msc. thesis, Freie Universität Berlin.

BOITZ, N. & SHAPIRO, S. (2018). Non double-couple components of seismic moments caused by seismic anisotropy. In *80th EAGE Conference and Exhibition*.

BOITZ, N. & SHAPIRO, S. (2021). Geomechanical stress conditions to induce half-moon events during hydraulic fracturing. *Geophysics*, **Accepted**.

BOITZ, N., RESHETNIKOV, A. & SHAPIRO, S. (2018). Visualizing effects of anisotropy on seismic moments and their potency-tensor isotropic equivalent. *Geophysics*, **83**, C85–97.

ČERVENÝ, V. (2001). *Seismic Ray Theory*. Cambridge University Press.

CHAPMAN, C. (2004). *Fundamentals of Seismic Wave Propagation*. Cambridge University Press.

CHAPMAN, C. (2019). Yet another moment-tensor parameterization. *Geophysical Prospecting*, **67**, 485–495.

CHAPMAN, C.H. & LEANEY, W.S. (2012). A new moment-tensor decomposition for seismic events in anisotropic media. *Geophysical Journal International*, **88**, 343–370.

CHENG, X., TANG, J., ZDRAVEVA, O., YARMAN, C. & HOBRO, J. (2012). Ray-based prestack depth migration for orthorhombic media. *SEG Technical Program Expanded Abstracts*, 4609.

CHUPRAKOV, D. & PRIOUL, R. (2015). Hydraulic fracture height containment by weak horizontal interfaces. *SPE Hydraulic Fracturing Tecnology Conference*.

COMSOL-MULTIPHYSICS® (V 5.4). www.comsol.com comsol ab, stockholm, sweden.

DETOURNAY, E. (2016). Mechanics of hydraulic fractures. *Annual Review of Fluid Mechanics*, **48(1)**, 311–339.

FEDOROV, F.I. (1968). *Elastic Waves in Crystals*. Springer Science+Business Media New York.

FROHLICH, C. (1992). Triangle diagrams: ternary graphs to display similarity and diversity of earthquake focal mechanisms. *Physics of the Earth and Planetary Interiors*, **75**, 193–198.

FROHLICH, C. (2001). Display and quantitative assessment of distributions of earthquake focal mechanisms. *Geophysical Journal International*, **144**, 300–308.

GRECHKA, V. (2014). On the feasibility of inversion of single-well microseismic data for full moment tensor. *Geophysics*, **80**, KS41–KS49.

GRECHKA, V. (2020a). *Anisotropy and Microseimics*. Society of Exploration Geophysicists.

GRECHKA, V. (2020b). Moment tensors of double-couple microseismic sources in anisotropic formations. *Geophysics*, **85**, KS1–KS11.

GRECHKA, V. & HEIGL, W.M. (2017). *Microseismic Monitoring*. Society of Exploration Geophysicists.

GRECHKA, V., LI, Z., HOWELL, R. & VAVRYCUK, V. (2017). Single-well moment tensor inversion of tensile microseismic events. *SEG Technical Program Expanded Abstracts 2017*, 2746–2751.

GRIGOLI, F., CESCA, S., RINALDI, A.P., MANCONI, A., LÓPEZ-COMINO, J.A., CLINTON, J.F., WESTAWAY, R., CAUZZI, C., DAHM, T. & WIEMER, S. (2018). The november 2017 mw 5.5 pohang earthquake: A possible case of induced seismicity in south korea. *Science*, **360**, 1003–1006.

HEIDBACH, O., RAJABI, M., REITER, K., ZIEGLER, M. & TEAM, W. (2016). *World Stress Map Database Release 2016*. GFZ Data Services.

HOOKE, R. (1678). *De Potentia Restitutiva, or of Spring Explaining the Power of Springing Bodies*. London.

HUBBERT, M.K. & WILLIS, D. (1957). Mechanics of hydraulic fracturing. *Society of Petroleum Engineers*, 153–163.

HUDSON, J., PEARCE, R. & ROGERS, R. (1989). Source type plot for inversion of the moment tensor. *Journal of Geophysical Research*, **94**, 765–774.

HUMMEL, N. & SHAPIRO, S. (2013). Analysis and interpretation of hydraulic fracturing induced seismicity from the horn river basin. In *9th Annual PHASE report*.

JAEGER, J., COOK, N.G.W. & ZIMMERMANN, R.W. (2007). *Fundamentals of Rock Mechanics*. Blackwell Publishing.

JOST, M.L. & HERRMANN, R.B. (1989). A students's guide to and review of moment tensors. *Seismological Research Letters*, **60, 2**, 37–57.

KAGAN, Y.Y. (2007). Simplified algorithms for calculating double-couple rotation. *Geophysical Journal International*, **171**, 411–418.

KNOPOFF, L. & RANDALL, M. (1970). The compensated linear-vector dipole: A possible mechanism for deep earthquakes. *Journal of Geophysical Research*, **75**, 4957–4963.

KUANG, W., ZOBACK, M. & ZHANG, J. (2017). Estimating geomechanical parameters from microseismic plane focal mechanisms recorded during multistage hydraulic fracturing. *Geophysics*, **82**, KS1–KS11.

LAY, T. & WALLACE, T.C. (1995). *Modern Global Seismology*. Academic Press.

LEANEY, S. & CHAPMAN, C. (2010). Microseismic sources in anisotropic media. In *82nd EAGE Conference and Exhibition*.

LECAMPION, B., BUNGER, A. & ZHANG, X. (2018). Numerical methods for hydraulic fracture propagation: A review of recent trends. *Journal of Natural Gas Science and Engineering*, **49**, 66–83.

MAXWELL, S. (2014). *Microseismic Imaging of Hydraulic Fracturing: Improved Engineering of Unconventional Shale Reservoirs*. Society of Exploration Geophysicists.

NOLEN-HOEKSEMA, R.C. & RUFF, L.J. (2001). Moment tensor inversion of microseisms from the b-sand propped hydrofracture, m-site, colorado. *Tectonophysics*, **336**, 163–181.

RESHETNIKOV, A. (2014). Ray-tracing for microseismic monitoring in strongly anisotropic media. In *9th Annual PHASE report*.

RESHETNIKOV, A. & SHAPIRO, S. (2015). Using multipath shear wave arrivals for velocity model inversion and microseismic location in strongly anisotropic shale. In *10th Annual PHASE report*.

RICE, J.R. (1980). *The Mechanics of Earthquake Rupture*. Elsevier/North Holland, Amsterdam.

RIEDESEL, M. & JORDAN, T. (1989). Display and assessment of seismic moment tensors. *Bulletin of the Seismological Society of America*, **79**, 85–100.

RÖSER, A. & SHAPIRO, S. (2019). Improved efficiency of ray tracing by using adaptive step size control in anisotropic media. In *SEG Technical Program Expanded Abstracts*, 3894–3898.

RÖSER, A., BOITZ, N. & SHAPIRO, S. (2018). Ray tracing with adaptive step size control in inhomogeneous anisotropic media. In *80th EAGE Conference and Exhibition*.

RUTLEDGE, J. (2019). Is bedding-plane slip a common microseismic source during hydraulic fracturing? In *SEG Technical Program Expanded Abstracts*.

RUTLEDGE, J., YU, X. & LEANEY, S. (2015). Microseismic shearing driven by hydraulic-fracture opening: An interpretation of source-mechanism trends. *The Leading Edge*, 926–934.

RUTLEDGE, J., WENG, X., CHAPMAN, C., YU, X. & LEANEY, S. (2016). Bedding-plane slip as a microseismic source during hydraulic fracturing. *SEG International Exposition and 86th Annual Meeting*, 2555–2558.

SEGALL, P. (2010). *Earthquake and Volcano Deformation*. Princeton University Press.

SHAPIRO, S., HUENGES, E. & BORM, G. (1997). Estimating the crust permeability from fluid-injection-induced seismic emission at the ktb site. *Geophysical Journal International*, F15–F18.

SHAPIRO, S., AUDIGANE, P. & ROYER, J.J. (1999a). Large-scale in situ permeability tensor of rocks from induced microseismicity. *Geophysical Journal International*, 207–213.

SHAPIRO, S., AUDIGANE, P., ROYER, J.J. & FEHLER, M. (1999b). An inversion for the permeability tensor by using seismic emission. *SEG Expanded Abstracts*.

SHAPIRO, S.A. (2015). *Fluid-Induced Seismicity*. Cambridge University Press.

SHEARER, P. (2012). *Introduction to Seismology 2nd Edition*. Cambridge University Press.

SHERIFF, R.E. & GELDART, L.P. (1995). *Exploration Seismology*. Cambridge University Press, 2nd edn.

ŠOLC, K. (1971). Shape of a random-flight chain. *The Journal of Chemical Physics*, 335–344.

ŠOLC, K. & STOCKMAYER, W.H. (1971). Shape of a random-flight chain. *The Journal of Chemical Physics*, 2756–2757.

STANĚK, F. & EISNER, L. (2013). New model explaining inverted source mechanisms of microseismic events induced by hydraulic fracturing. *SEG Technical Program Expanded Abstracts*, 2201–2205.

STANĚK, F. & EISNER, L. (2017). Seismicity induced by hydraulic fracturing in shales: A bedding plane slip model. *Journal of Geophysical Research*, 7912–7926.

STEIN, S. & WYSESSION, M. (2013). *An Introduction to Seismology, Earthquakes, and Earth Structure*. Blackwell Publishing.

TAPE, W. & TAPE, C. (2013). The classical model for moment tensors. *Geophysical Journal International*, **195**, 1701–1720.

THOMSEN, L. (1986). Weak elastic anisotropy. *Geophysics*, **51**, 1954–1966.

TSVANKIN, I. (1997). Anisotropic parameters and p-wave velocity for orthorhombic media. *Geophysics*, **62**, 1292–1309.

TUTTLE, S., GRECHKA, V., JAHAN, I. & ZHANG, Z. (2020). Spatiotemporal gyration from microseismicity in the permian basin. *8th Unconventional Resources Technology Conference*.

VAVRYČUK, V. (2005). Focal mechanisms in anisotropic media. *Geophysical Journal International*, **161**, 334–346.

VAVRYČUK, V. (2015). Moment tensor decomposition revisited. *Journal of Seismology*, **19**, 231–252.

WARPINSKI, N., WOLHART, S. & WRIGHT, C. (2004). Analysis and prediction of microseismicity induced by hydraulic fracturing. *SPE Journal*, 24–33.

WENG, X., CHUPRAKOV, D., KRESSE, O., PRIOUL, R. & WANG, H. (2018). Hydraulic fracture-height containment by permeable weak bedding interfaces. *Geophysics*, **83**, 137–152.

YU, X., LEANEY, S., RUTLEDGE, J. & CHAPMAN, C. (2016). Multievent moment-tensor inversion for ill-conditioned geometries. *Geophysics*, **81**, KS11–KS24.

ZHU, L. & BEN-ZION, Y. (2013). Parametrization of general seismic potency and moment tensors for source inversion of seismic waveform data. *Geophysical Journal International*, **194**, 839–843.

ZOBACK, M. & SNEE, J.E.L. (2018). Predicted and observed shear on pre-existing faults during hydraulic fracture stimulation. *SEG Technical Program Expanded Abstracts 2018*, 3588–3592.

ZOBACK, M.D. (2007). *Reservoir Geomechanics*. Cambridge University Press.

Curriculum Vitae

Der Lebenslauf ist in der Online-Version aus Gründen des Datenschutzes nicht enthalten.

Publications

Journal Publications

2021 Boitz, N. & Shapiro, S. (2021). Geomechanical stress conditions to induce half-moon events during hydraulic fracturing. Geophysics. Accepted. doi:10.1190/geo2019-0681.1

2018 Boitz, N., Reshetnikov, A., & Shapiro, S. (2018). Visualizing effects of anisotropy on seismic moments and their potency-tensor isotropic equivalent. Geophysics, 83, C85–97. doi:10.1190/geo2017-0442.1

Conference Proceedings

2020 Boitz, N. & Shapiro, S. (2020). Stress field rotations at the tip of hydraulic fractures: an explanation for half-moon events ? In 82nd EAGE Conference and Exhibition (accepted).

2019 Boitz, N. & Shapiro, S. (2019a). Geomechanical conditions to create half-moon events during hydraulic fracturing. In SEG Technical Program Expanded Abstracts 2019.doi:10.1190/segam2019-3214643.1

Boitz, N. & Shapiro, S. (2019b). Stress conditions for dip-slip events during hydraulic fracturing. In 81st EAGE Conference and Exhibition.

Boitz, N. & Shapiro, S. (2019c). The influence of seismic anisotropy on microseismic moment tensors and their radiation patterns. In Schatzalp-Workshop 2019, Davos

2018 Boitz, N. & Shapiro, S. (2018). Non double-couple components of seismic moments caused by seismic anisotropy. In 80th EAGE Conference and Exhibition

Roeser, A., Boitz, N., & Shapiro, S. (2018). Ray tracing with adaptive step size control in inhomogeneous anisotropic media. In 80th EAGE Conference and Exhibition.

2016 Boitz, N., Reshetnikov, A., & Shapiro, S. (2016). Anisotropic source mechanism construction and waveform modeling. In 78th EAGE Conference and Exhibition.

Danksagungen

Zuallererst gilt mein großer Dank Prof. Serge Shapiro für die Ermöglichung und Betreuung dieser Arbeit. Danke für die vielen fachlichen Diskussionen und kreativen Ideen die maßgeblich zu dieser Arbeit beigetragen haben.

Vielen Dank an Prof. Tilmann für die Übernahme des Zweitgutachtens.

Ich danke Dr. Jörn Kummerow, der mit seiner Lehrveranstaltung "Erdbeben und Struktur der Erde" vor vielen Jahren meine Begeisterung und Interesse für die Seismologie geweckt hat. Danke Jörn, dass Du immer ein offenes Ohr für Probleme und Fragen hast und für die Möglichkeit die Übung zu deiner Lehrveranstaltung betreuen zu dürfen.

Danke Lisa für unsere gemeinsame Zeit in Lankwitz, für die Planung unserer gemeinsamen Kurse, den fachlichen Austausch und für unsere kulinarischen Projekte abseits der Arbeit.

Mein Dank gilt außerdem Aurelian für die Möglichkeit, seine Raytracing Software zu nutzen, ohne die die Momententensorinversion in Kapitel 4 nicht möglich gewesen wäre. Danke für deine Hilfe und für die vielen und langen Diskussionen über die Numerik des Raytracings.

Ich danke meinen Kollegen in Lankwitz, Stine, Jonas, Rens, Ivan und Henri für die gemeinsame Zeit.

Danke Jörg für deine Hilfe in technischen Fragen rund um Linux, COMSOL und Co.

Einen besonderen Dank an meine Familie und Freunde, für eure Motivation und Unterstützung und euer Interesse zu verstehen, was ich eigentlich mache.

Der letzte und größte Dank geht an meine Frau Luise. Danke für deine Unterstützung, Wertschätzung und deine Art, immer die richtigen Worte zu finden. Danke für unsere gemeinsamen letzten Jahre, ich freue mich auf unsere Zukunft.